Production of Energy and Chemicals by Thermochemical Conversion from Recycled and Renewable Biomass

A DISSERTATION
SUBMITTED TO THE FACULTY OF THE
UNIVERSITY OF MINNESOTA
BY

Cheng Zhu

IN PARTIAL FULFILLMENT OF THE REQUIREMENTS
FOR THE DEGREE OF
DOCTOR OF PHILOSOPHY

Adviser: Paul Dauenhauer

August 2016

Acknowledgements

I would, first and foremost, like to express my sincere gratitude to my adviser, Professor Paul Dauenhauer, for accepting me into his research group and providing me the opportunity to further explore the realm of science and engineering. His insightful guidance and continuing support for the last five years have cultivated my critical thinking and made my research efforts fruitful. Professor Dauenhauer has great passion, motivation, and ambition in research, from who I have learnt a lot that I could extend to my future life. I would also like to thank my current and former group members, Dr. Matthew Mettler, Dr. Jin Yang, Dr. Sara Green, Dr. Luke Williams, Dr. Andrew Teixeira, Dr. Sheng Chu, Xiaoduo Qi at University of Massachusetts and Dr. Alex Paulsen, Dr. Dae Sung Park, Dr. Charles Spanjers, Christoph Krumm, Kristeen Joseph, Saurabh Maduskar, Katherine Vinter, Gregory Facas at University of Minnesota for providing frequent conversations about research and their constant support and valuable advices when I faced difficulties. All the joyful and unforgettable moment we spent together have made us far more beyond just group members. I would especially like to thank Dr. Geoff Tompsett for training me in the beginning of my research work and assistance with running experiments. His personal knowledge and wisdom have taught me invaluable lessons. I would like to further extend my appreciation to Accordant Energy collaborators Dr. Dingrong Bai and Paula Calabrese for their useful suggestions on the project. Additionally, I would like to thank Julie Prince for making my transfer smoothly and helping with adapting to the new department. Furthermore, I must acknowledge all my friends outside the department for making my graduate life more balanced and colorful. A great thanks goes to my closest

friends including Jie Zhao, Chenxu Yang, Kristeen Joseph who have always comforted me and by my side in my times of need. Finally, I am very grateful for the love and support from my family who encourage me to pursue my highest goal in graduate school and let me follow my dream in life. I know without my parents, I would not be where I am today.

Abstract

Recovery energy from municipal solid waste and biomass are one of the leading methods to achieve maximum energy efficiency and environmental sustainability. The two major technical approaches are biochemical conversion like fermentation and thermochemical conversion processes include combustion, gasification, and pyrolysis. Since thermochemical conversions have short processing cycle, higher productivity and complete utilization of almost any type of feedstocks as advantages, my research focused on production of energy and chemicals by thermochemical conversion from recyclable and renewable feedstocks, mainly including two projects: novel biomass-supported sorbent for coal combustion emission control and fundamental study of biomass fast pyrolysis in the presence of alkaline earth metals.

The first research project coal combustion emission control was collaborated with Accordant Energy LLC. on the development of ReEngineered Feedstock. A new coal reaction technology called ReEngineered Feedstock^{TM} (ReEF), consisting of sorbent-containing post-recycled paper and plastics, was evaluated for coal combustion emission control when co-firing with pulverized coal in mixtures containing from 26 to 37 wt% ReEF. Experiments were conducted with four types of ReEF in a two-inch diameter laboratory-scale fluidized bed combustor system heated to 1200, 1400 and 1600 °C. Flue gas emission was continuously monitored with an online infrared multi-gas analyzer and mass spectrometer. The results indicate that co-firing ReEF with coal provides SO_2 reduction in flue gas up to 85% and moderate decrease in NO emission, as well as higher carbon conversion than pure coal combustion. ReEF feedstock and slag & ash solids were

analyzed by XRD; identification of sulfates in the product ash conclusively supports the mechanism of in situ sulfur capture.

Sulfation kinetics of ReEF combustion were evaluated in a drop-tube reactor at variable conditions (800 - 1000 °C, 1400 ppm SO_2, 5% - 30% O_2 in nitrogen) with continuous effluent characterization via online infrared spectroscopy. Pelletized ReEF consisted of refuse-derived fuel (RDF, 65 wt% non-recyclable fibers/plastics) and integrated calcium hydroxide sorbent (35 wt%) was taken as an example. Characterization of ReEF with SEM-EDX indicated random distribution of calcium hydroxide sorbents on fiber/plastic particles. Sulfation of calcium hydroxide in ReEF was delayed due to RDF combustion when compared with pure calcium hydroxide sorbent. A low oxygen condition was shown to produce high conversion of calcium hydroxide to calcium sulfate ($X_{Ca(OH)_2} > 0.4$). While, calcination and combustion of ReEF in a high oxygen environment ($O_2 > 20\%$) result in increased sorbent sintering and reduced total sulfur uptake.

The second project investigated the chemical reactivity of cellulose decomposition in the presence of alkaline earth metals. Conversion of lignocellulosic biomass to ‘bio-oils’ via pyrolysis is a promising reactor technology for renewable chemicals and biofuels. While fundamental understanding of the relevant catalysts within reacting biomass particles is only in its infancy, it is known that inorganic materials naturally present within biomass act as catalysts, limiting the yield of bio-oil and altering the product distribution. In this work, the effect of alkaline earth metals on cellulose pyrolysis chemistry was investigated to determine the catalytic effect on primary (transport-free) and secondary (diffusion-limited) reaction pathways. Catalytic materials included homogeneous metal ions (Ca^{2+}, Mg^{2+}) from their inorganic salts, $Ca(NO_3)_2$ and $Mg(NO_3)_2$, and their

corresponding heterogeneous metal oxides (CaO, MgO). While oxides were shown to have limited impact on cellulose pyrolysis chemistry, metal ions were found to significantly alter the secondary reaction pathways of cellulose under diffusion-limited conditions common to lignocellulosic particles within industrial reactors.

The initial breakdown kinetics of cellulose were examined from 385 °C to 505 °C using a millisecond, thin-film reactor called PHASR (Pulse-Heated Analysis of Solid Reactions). Using the cellulose surrogate, α-cyclodextrin, the energetics of each kinetic regime were characterized by measuring the conversion between 20 ms and 2.0 seconds. An interesting finding is that cellulose undergoes two distinct kinetic regimes with a distinct transition at 467 °C, which is interpreted as a reactive melting point. The low temperature kinetic regime exhibited a low activation energy for glycosidic bond cleavage ($E_{a,1} = 23.2 \pm 1.9$ kcal/mol, $k_{0,1} = 2.0 \times 10^{7}$ 1/s) consist a chain-end cleavage mechanism, while the high temperature regime ($E_{a,2} = 53.7 \pm 1.1$ kcal/mol, $k_{0,2} = 2.4 \times 10^{16}$ 1/s) was consistent with intra-chain scission. Further work continues on adding calcium into α-cyclodextrin samples to quantitatively compare the relative change in reaction rates and activation energies of the decomposition reactions. Increasing Ca loading dramatically increased reaction rate with much shorter time to complete the conversion. One important discovery is that the reaction rate exhibits second order dependence on the Ca concentration. The apparent energetics for Ca-catalyzed cyclodextrin decomposition is similar to that of pure cyclodextrin at high temperature, which implies the presence of Ca ions may change cellulose decomposition mechanism from chain-end cleavage to intra-chain scission.

Table of Contents

List of Figures

List of Tables

Chapter 1. Introduction

1.1 Background

Demand for energy and its resources is increasing every day due to the rapid outgrowth of population and urbanization. About 91% of the energy consumed in the United States comes from non-renewable energy sources, which include uranium ore and the fossil fuels—coal, natural gas, and petroleum. While, renewable energy sources including biomass, hydropower, geothermal, wind, and solar provide only 9% of the energy used in the United States. [1] Among them, recovery energy from municipal solid waste and biomass are one of the leading methods to achieve maximum energy efficiency and environmental sustainability. The two major technical approaches include thermochemical conversion involving three options: combustion, gasification, and pyrolysis to produce heat, steam, electricity, and liquid fuels or biochemical conversion using enzymes and bacteria to break down biomass to liquid fuels like fermentation. [2] Thermochemical conversions have short processing cycle, higher productivity and complete utilization of almost any type of feedstocks as advantages, therefore as the main focus of this study.

Biomass is available abundant in nature and is cheap as a renewable source. It can be divided into three categories: wastes, forest products and energy crops. [3] World production of biomass is estimated at 146 billion metric tons a year, mostly wild plant growth. [4] Thus, thermochemical conversion of biomass has a potential to provide a cost effective and sustainable supply of energy. Pretreatment is needed for waste and biomass feedstocks through a series of processes including separation, size reduction, drying and densification to be fit for feeding. [5] Combustion process which burns waste and biomass in the presence of excess air to achieve complete oxidation has been discussed in Chapter 2 and 3, while pyrolysis of biomass in the absence of oxygen to produce a liquid bio-oil is stated in Chapter 4 and 5.

1.2 Motivation

Biomass is receiving significant attention as a renewable energy resource for fuels and chemicals. Utilization of biomass through different thermochemical conversion processes converting into various energy products has been investigated by researchers for decades.

In the first study of coal combustion emission control, the effects of co-feeding sorbent-containing ReEF materials with coal was investigated on the sequestration of pollutants in flue gas, such as SO_2 and NO. ReEF materials are composed of non-recyclable fibers and plastics combined with sorbents including hydrated lime, sodium bicarbonate, and Trona. Integration of waste materials with these sorbents has led to a new clean coal reaction technology called ReEngineered Feedstock^{TM} (ReEF), developed by Accordant Energy, LLC (formerly known as ReCommunity Energy, LLC.). ReEF [6]–[8] is designed to be physically and chemically compatible to coal utilized in a pulverized coal combustor, such that it can be directly co-reacted with existing coal feeding/handling infrastructure in combustion facilities. Utilization of refuse-derived fuel (RDF) can replace up to 30% of coal with post recycled materials, [9] which otherwise would be landfilled. ReEF was characterized to determine the structure of the sorbent-RDF matrix. The study aims to evaluate the effectiveness of ReEF as an innovative and efficient reactant co-feed for coal combustion and emission reduction using a fluidized bed combustor.

Kinetics of sulfur capture and general desulfurization behavior of ReEF particles was evaluated under a series of reaction conditions in a vertical sulfation reactor system. The effects of combustion on sorbent calcination and sulfation were also evaluated in a horizontal calcination furnace, capable of providing short-time exposure to high temperatures and reactant gases. Results reveal that sulfation of sorbent in ReEF is postponed by the combustion of surrounding RDF, thereby providing a tunable reactant particle system for controlling the time and position of desulfurization within pulverized coal combustion reactors. This technology has the dual potential to impact the economics and environmental footprint of both waste management and coal-fired power plants.

The second study of the technology for conversion of biomass to 'bio-oils' via pyrolysis is a promising approach that has reached an intermediate stage of development. The underlying challenges in pyrolysis chemistry are the complex cellular structure of woody biomass and the presence of inorganic species within biomass that act as natural catalysts, significantly affecting the yield of bio-oil as well as its product distribution. This research aims to understand biomass pyrolysis at the molecular level in the presence of alkaline earth metals. Varying concentrations of calcium and magnesium cations have been doped into pure cellulose from their inorganic salts ($Ca(NO_3)_2$ and $Mg(NO_3)_2$) using ion-exchange, while the corresponding oxides (CaO and MgO) are incorporated with cellulose by dry mixing. Additionally, levoglucosan (LGA) is impregnated with calcium nitrate and magnesium nitrate to evaluate secondary melt-phase products. Thin-film pyrolysis was utilized to delineate the catalytic role of calcium and magnesium on primary versus secondary melt-phase reactions of cellulose.

As to the kinetics of pyrolysis reactions, current pyrolysis mechanisms and nature of intermediates are proposed based on initial and final pyrolysis compositions from a variety of experimental reactors and conditions. [10]–[14] Complex reactions and extremely short time scales make existing analytical techniques inadequate to capture kinetic. The Pulsed-Heated Analysis of Solid Reactions (PHASR) technique is utilized to measure the precise kinetics and associated energetics of glycosidic bond cleavage. Initial experiments validate the use of α-cyclodextrin as a kinetic surrogate of cellulose. Quantification of the conversion of α-cyclodextrin with time (20 ms to 2.0 sec) for a range of temperatures (385–505 °C) enables elucidation of reaction rate coefficients and determination of the apparent activation energy and associated pre-exponential factors for cellulose cleavage. Further work of adding calcium into α-cyclodextrin samples enables to quantify the catalytic effect of alkaline earth metals in terms of relative change in reaction rates and activation energies of the decomposition reactions. Determining the role of natural inorganic catalysts in altering pyrolysis chemistry within the intermediated liquid and the nature of primary reactions will allow for optimization of transport-kinetic models used to scale up and optimize pyrolysis reactors and contribute to the development of biofuel production processes. This fundamental catalytic study will be a starting point for the future generation of detailed kinetic schemes which can be directly implemented in reactor-level modeling and optimization software.

Chapter 2. Novel Biomass-Supported Sorbent for Coal Combustion Emission Control

2.1 Introduction

Coal combustion remains and is predicted to be an important process for electricity production in the United States and many countries around the world for the foreseeable future. [15] The United States produces approximately seven quadrillion BTUs of electrical power per year from coal, constituting 42% of all electrical energy being produced in the country in 2011. [16] However, coal power plants produce gases such as SO_x, NO_x and HCl, which can lead to environmental problems including formation of acid rain. Power stations that use coal boilers exhibit typical stack flue gas concentrations before scrubbing of 200-2000 ppm SO_2, 50-100 ppm CO, and 800 ppm NO_x, [17] which are orders of magnitude higher than permitted by regulation. [18], [19] Increasingly protective regulations, such as the Clean Air Act, mandate the reduction of emissions from coal combustion facilities. For instance, to comply with the Acid Rain Program in New England, Merrimack Station has completed its Clean Air Project on Mar. 30, 2012. This plant has reduced its mercury and sulfur dioxide emissions by more than 95% [20] and is currently one of the cleanest coal-fired power plants in the United States.

Significant investment is required downstream of the coal-fired boiler to remove SO_x and NO_x pollutants to regulated levels. While numerous technologies exist for emissions cleaning, such as wet scrubbing of the exhaust gas, augmentation of new chemical processing equipment to existing power plants introduces significant capital costs, and sometimes increases water consumption and decreases energy efficiency. A transformational solution aims to develop an energy-rich coal co-reactant from post-recycled materials which can be utilized within existing coal combustion facilities as both a fuel substitute and a sorbent of harmful process emissions.

2.1.1 Emission Control Technologies

Co-combustion of coal and CO_2-neutral fuel such as refuse-derived fuels (RDF) is one method of reducing CO_2 emissions during energy production while simultaneously decreasing other undesirable emissions such as SO_x and NO_x. RDF is produced from Municipal Solid Waste (MSW) through a process of screening, size reduction, separation and drying. [5] The heating value of RDF is comparable to other biomass such as straw and wood, which allows for the possibility of being injected into a pulverized coal boiler for energy generation. [21] Co-firing of coal with RDF has been investigated previously by others. [9], [22]–[32] In general, undesired emissions such as SO_x are reduced by co-firing RDF due to its relatively low sulfur content compared to coal.

Sorbent addition, blended with coal combustion, is another well-known technique for the reduction of SO_x, NO_x, mercury and other pollutants. [33]–[37] Traditional sorbent materials used for desulfurization are typically alkali compounds, including lime (CaO) or hydrated lime ($Ca(OH)_2$), calcium carbonate ($CaCO_3$), soda ash (Na_2CO_3), caustic soda (NaOH) and others. Lime is the most common sorbent used during combustion forming the stable calcium sulfate ($CaSO_4$) in oxidizing conditions and calcium sulfide (CaS) under reducing (low oxygen) conditions. [34]

$$CaO + SO_2 + \tfrac{1}{2}O_2 \rightarrow CaSO_4 \quad \text{oxidizing conditions} \tag{2.1}$$

$$CaO + H_2S \rightarrow CaS + H_2O \quad \text{reducing conditions} \tag{2.2}$$

Another sorbent, sodium bicarbonate ($NaHCO_3$), has been utilized for flue gas sorption including SO_2, HCl and HF. $NaHCO_3$ decomposes at high temperatures to form Na_2CO_3, which has high specific surface area and reacts with HCl and SO_2 to produce NaCl and Na_2SO_4. [38]–[40] The following reactions take place at high temperatures for the neutralization of SO_2.

$$2NaHCO_3 + \text{heat} \rightarrow Na_2CO_3 + CO_2 + H_2O \quad (2.3)$$

$$Na_2CO_3 + SO_2 + \tfrac{1}{2}O_2 \rightarrow Na_2SO_4 + CO_2 \quad (2.4)$$

It is reported that $NaHCO_3$ sorbent achieves a high degree of desulfurization, but it is not recommended for high temperature applications for sintering. Hydrated lime desulfurization efficiency in dry conditions is in the range of 30–40%. [38]

Although the addition of inorganic sorbents to control the emission of toxic trace elements from coal combustion has previously been reported in laboratory, pilot, or commercial-scale fluidized bed combustors, [41], [35], [36] the effectiveness of these technologies has proven limited. The furnace sorbent injection process is cheap to install but can be expensive to operate, since inefficient utilization of sorbents and high furnace temperatures make the desulfurization product unstable. [34], [36], [37] For instance, the conventional sulfation product $CaSO_4$ thermally decomposed with high flame temperature above 1200 °C, regardless of combustor type (industrial grate furnaces (IGF) or pulverized coal fired boilers (PCFB)). Cheng et al. [41] observed that sorbent absorptive capacity is related to both physical qualities of the absorbents (type, amount and particle size) and the combustion temperature. For example, smaller particles have greater surface area and more internal pores, which can enhance the reaction between trace element-containing vapors and absorbents. Desulfurization efficiency at 1100 °C, measured by Cheng et al., [41] was only 22.1% for CaO of 125-300 μm, while sulfur removal could reach 35.1% for CaO of <75 μm. Despite improved performance for small CaO sorbents, overall sulfur removal was still relatively low.

Few reports exist on the combination of sorbent and RDF or MSW co-firing with coal. Waste materials can be combusted for heat generation, while sorbents react with flue gas and capture SO_2 and HCl, provided they can be combined in a single particle. Daugherty et al. [42] examined over 150 potential binders and binder combinations for the lab tests. Final results showed calcium hydroxide or quicklime to be the best performing binder. Ohlsson [43] carried out co-firing tests using 12 wt% calcium hydroxide binder RDF and 88 wt% coal in a 440 MW cyclone fired combustor for 10 h. The results showed that sulfur (SO_2) was reduced by about 17% and NO_x by 2-3%. Liu et al. [44] reported that HCl could be removed by adding CaO to MSW combustion, producing $CaCl_2$. F. Okasha [45] showed that by impregnating CaO in the combined straw-bitumen pellets instead of feeding sorbent separately, a major portion of sulfur was retained throughout the entire burning period.

2.1.2 ReEngineered Feedstock

Integration of waste materials with additives or sorbents has led to a new clean coal reaction technology called ReEngineered Feedstock^{TM} (ReEF), developed by Accordant Energy, LLC (formerly known as ReCommunity Energy, LLC.). [8] First, recyclable fibers and plastics, metals and inert materials were separated from municipal, institutional and commercial wastes. The remaining non-recyclable fibers and plastics were separated and recombined at a prescribed weight ratio. Sorbents were then mixed with the recombined non-recyclable fibers and plastics and pelletized into ReEF pellets (cylinders, approx. 4-5 mm diameter). Pellets were then pulverized for use in this study. The majority of pulverized ReEF particles ranged from 300 to 1000 μm, while coal was sieved to particle sizes of 50-300 μm. Elemental analyses of coal and four ReEF are listed in Table 2.1. Compared with coal, ReEF has higher volatile matter and less fixed carbon, nitrogen, and sulfur, which leads to lower SO_2 and NO_x emissions; depending on fiber/plastic ratio and sorbent content, ReEF can have energy content over a wide range – lower than, similar to biomass, or comparable with coal. The higher ash content in ReEF is primarily due to the added inorganic sorbent.

Table 2.1. Elemental analysis of coal and ReEF.

Sample	Proximate Analysis (wt%)				Ultimate Analysis (wt%)					Heat of Combustion	
	Moisture	Volatile Matter	Fixed Carbon	Ash	H	C	N	O	S	Btu/lb	Kcal/kg
coal	2	33.13	57.2	7.7	5.4	75.3	1.8	8	1.7	13607	7564.50
ReEF SL[a]	1.24	59.67	5.33	33.76	5.08	33.76	0.06	26.11	0.04	5787	3217.15
ReEF ML[b]	2.39	49.9	15.13	32.58	5.24	28.99	0.05	33.03	0.039	5546	3083.17
ReEF SB[c]	7.79	55	9.51	27.7	4.93	36.46	0.086	30.82	0.041	6018	3345.57
ReEF Trona[d]	9.52	52.32	9.51	33.63	5.04	34.88	0.067	26.33	0.051	5538	3078.73

a. Sorbacal lime—high surface area hydrated lime
b. Mississippi lime—standard hydrate lime
c. Sodium bicarbonate
d. Pre-milled Trona

Pulverized ReEF was combined with pulverized coal in different mass ratios and mixed thoroughly prior to use. The properties of ReEF including weight percent of components in ReEF and weight percent of ReEF combined with pulverized coal are shown in Table 2.2. ReEF content in coal/ReEF mixture are recommended by the Accordant Energy from 26 wt% to 37 wt%. The energy content of coal/ReEF mixture is approximately 30 kJ/g, which is similar to that of the bituminous coal. ReEF is compared with each independent sorbent, including Sorbacal lime, Mississippi lime, sodium bicarbonate, and pre-milled Trona, a naturally occurring mixture of sodium bicarbonate and sodium carbonate. These sorbents were either commercial products or natural materials. Table 2.2 shows the sorbent cation-(Ca, Na)-to-sulfur ratio for mixtures and the weight percent of sorbent in the mixtures of pure sorbent with coal.

Table 2.2. Properties of ReEngineered Feedstock (ReEF) and sorbents.

Sample	ReEF SL	ReEF ML	ReEF SB	ReEF Trona	Coal
Fibers (wt%)	52	52	53.6	49.6	0
Hard plastic (wt%)	13	6.5	6.7	6.2	0
Soft plastic (wt%)	0	6.5	6.7	6.2	0
Sorbent (wt%)	35	35	33	38	0
ReEF proportion[a] (wt%)	26	26	35	37	0
Mixture energy (kJ/g)	30.4	30.4	29.5	29.1	31.6
Sorbent type	Sorbacal lime	Mississippi lime	Sodium bicarbonate	Pre-milled Trona	None
Sorbent formula	$Ca(OH)_2$	$Ca(OH)_2$	$NaHCO_3$	$Na_3(CO_3)(HCO_3)\bullet 2H_2O$	None
Molecular weight (g/mol)	74	74	84	226	0
Cation/S ratio[b]	Ca/S=3.1	Ca/S=3.1	(Na/2)/S=2.0	(Na/2)/S=2.8	0
Sorbent proportion[c] (wt%)	11	11	15	18	0

a. ReEF percentagein coal/ReEF mixture (wt%), recommended by Accordant Energy
b. Sorbent cation (Ca, Na)-to-sulfur molar ratio for coal/ReEF mixture and coal/sorbent mixture
c. Calculated sorbent percentage in coal/sorbent mixture (wt%)

2.2 Experimental Description

ReEngineered Feedstock (ReEF) was evaluated at laboratory scale using a custom-built pulverized coal combustor with online infrared and mass spectrometry gas characterization. Four pulverized ReEF materials were tested.

2.2.1 Experimental Apparatus and Procedure

To demonstrate the effectiveness of ReEF co-feeding with coal, a fluidized bed combustion (FBC) reactor [46]–[48] of the was constructed as shown in the Figure 2.1 schematic of the reactor and analytical system. A 5.0 cm outer-diameter alumina tube (99.8%, CoorsTek Inc.) was the main reactor inside a high temperature furnace, which can withstand temperatures up to 1650 °C. The alumina tube was 100 cm in length with 80 cm placed inside the heated zone during operation. Three thermocouples (type B, Pt/30%Rh-Pt/6%Rh) were placed into the combustor tube from the top to measure the temperatures at each of three thermal zones. A distributor plate (316 stainless steel mesh) was welded to a stainless steel tube, 3.8 cm in diameter and 15 cm in length. The distributor plate/tube assembly was inserted into the bottom of the reactor tube and tightly sealed using a wrap of alumina insulation fabric. The top of the distributor plate was approximately 2.5 cm below the reactor inlet port of the feeder auger. The alumina reactor tube was sealed at both ends outside the furnace by water-cooled o-ringed flanges. A three-temperature zone furnace was purchased from Applied Test Systems Inc. (Series 3320 split furnace with Watlow EZ-Zone temperature controllers).

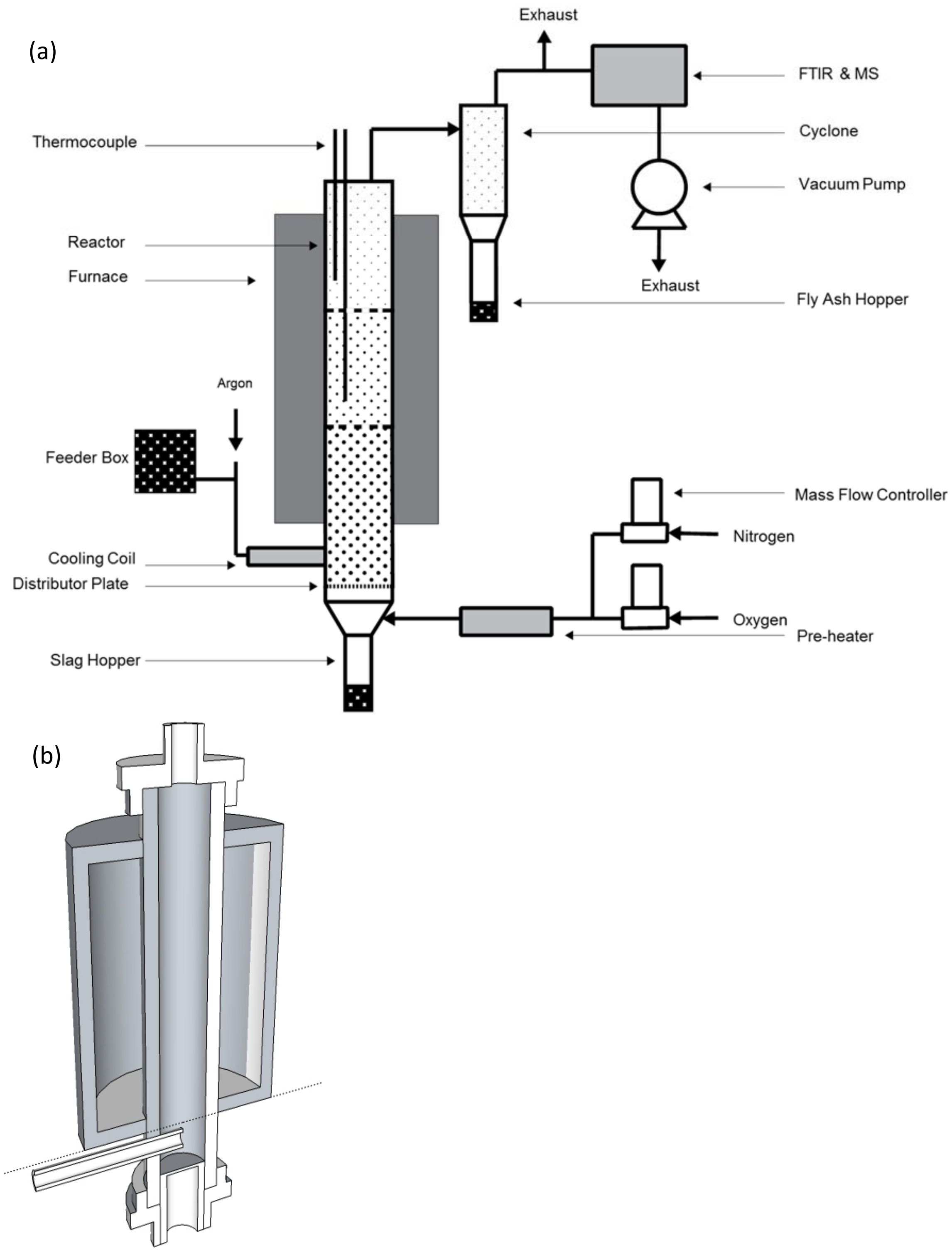

Figure 2.1. Schematic of fluidized bed combustion reactor. *(a) Flow diagram of the combustion system; (b) Rendering of the reactor, feed tube, flanges and gas distributor.*

The solid feed train consisted of a Schenck AccuRate® feeder (where the feedstock was stored) equipped with a 0.32, 0.95 or 1.27 cm helix auger (depending on the feed type), a drop tube, and a main auger driven by a DC motor at ~50 RPM. Two augers were necessary to avoid reaction within the feed train and plugging; the feeder controllably metered out solid feed, which fell through the drop tube, while a second fast auger rapidly pushed feedstock into the reactor just below the hot zone of the furnace. A cooling copper coil was wrapped around the main auger tube to prevent early pyrolysis and combustion due to high temperature at the bottom of the reactor. Fluidizing gas consisting of synthetic air was supplied by parallel mass flow controllers (Brooks Inc.) and preheated to 400 °C using resistive heating tape with temperature control (Watlow PID temperature controller). Heated gas entered the bottom of the reactor below the distributor plate. The gas flowed up, reacted with the solid feedstock and exited from the top to a cyclone system to separate fly ash. During reaction, ash dropped through the distributor plate to the slag hopper. One stream of the flue gas coming out of the cyclone was sent to the online analytical equipment with a vacuum pump. The sampling line included two stainless steel filters (Swagelok, 0.2 and 1 μm pore size) to remove any remaining particles in the sampled gas and prevent the analytical equipment from solid contamination.

The experimentally evaluated combustion conditions are listed in Tables 2.3 and 2.4. In experimental trials, the bottom zone was set to 1200, 1400 or 1600 °C, and the middle zone set to 1100, 1320, or 1550 °C, respectively. The top zone was not directly heated, but thermal conduction from the lower two furnace zones and convection of the up-flowing gases maintained reasonable temperature at experimental conditions. To heat up the reactor from room temperature to experimental conditions, a slow heating/cooling ramp (10 °C/min) was utilized to avoid cracking of the reactor tube due to rapid thermal expansion/contraction. During combustion, a temperature gradient of approximately 200 °C existed from the bottom to the top of the tube. The applied temperature gradient was similar to that exhibited in industrial coal combustion boilers. In each run, the feed rate was varied from 0.50 g/min to 0.61 g/min according to the feed type and maintained 5.0 L/min synthetic air, resulting in about 21% to 46% excess air through the reactor. Control, monitoring and data capture of the gas flows and reactor temperatures was achieved using LabVIEW virtual instrument. All set points were continuously logged. Each test occurred for about 40 to 60 minutes, and the collected data were analyzed at steady state conditions. Solid slag and fly ash were collected after the reactor was cooled below 50 °C.

Table 2.3. Temperature profile of the combustion reactor.

Temperature	Setting Value (°C)			Process Value[a] (°C)			Measured Value[b] (°C)		
	Case 1	Case 2	Case 3	Case 1	Case 2	Case 3	Case 1	Case 2	Case 3
Top Zone	0	0	0	1050	1275	1507	1033	1215	1421
Middle Zone	1100	1320	1550	1100	1320	1550	1118	1314	1530
Bottom Zone	1200	1400	1600	1200	1400	1600	1201	1397	1595

a. The temperature was from furnace outside the reactor
b. The temperature was from thermocouples inside the reactor

Table 2.4. Gas flow rate and feed conditions for pulverized combustion.

Feed type	Air flow rate (mL/min)	Argon flow rate (mL/min)	Feed rate (g/min)	Excess air (%)
coal	5000	20	0.50	21.1
coal/ReEF SL	5000	20	0.50	38.0
coal/ReEF ML	5000	20	0.50	40.0
coal/ReEF SB	5000	20	0.50	43.6
coal/ReEF Trona	5000	20	0.50	46.0
coal/SL	5000	20	0.56	21.1
coal/ML	5000	20	0.56	21.1
coal/SB	5000	20	0.59	21.1
coal/Trona	5000	20	0.61	21.1

2.2.2 Sample Materials

The process and preparation of the ReEF are performed and operated by Accordant Energy Inc. Processing of municipal, institutional and commercial wastes is a sophisticated process which consists of two phases: the Multi-Material Processing Platform (MMPP) and Advanced Product Manufacturing (APM). [8] The recyclable fibers and plastics, metals and inert materials are separated out from MMPP process. Also, a two-step thermal treatment is applied in MMPP process to remove chlorine embedded in the plastics. This will bring the concentration of chlorine down to the comparable levels of other fuels. The final materials from MMPP process are non-recyclable fibers and plastics which are ready to be combusted. On the second APM process, the sorbents are mixed with the non-recyclable fibers and plastics to pelletize into ReEF for transportation. Furthermore, heavy metal content of coal and ReEF SL are list in Table 2.5. There will not be extra heavy metal emission problem since the metal content are so low in coal and ReEF, such as only 0.13 ppm Hg in coal and less than 0.11 ppm in ReEF SL.

Table 2.5. Heavy metal content of coal and ReEF SL.

Metal (ppm)	Coal	ReEF SL
Ag	0.04	<0.8
Al	5100	6620
As	48	1
Ba	71	35.4
Be	1	<0.2
Cd	0.11	0.47
Co	3.6	0.58
Cr	9.9	8
Cu	21	9.2
Fe	8700	1810
Hg	0.13	<0.11
Mn	5.8	159
Ni	3.9	1.8
Pb	6.6	17.7
Sb	1.1	5.7
Se	4.1	<0.99
Ti	200	<0.099
V	17	2.4
Zn	13	16.2

There are three feed types: pure coal, coal/ReEF mixture and coal/sorbent mixture. As shown in Table 2.2, we take ReEF SL and the containing sorbent Sorbacal lime as an example. To testify ReEF as a co-reactant and sorbent for coal combustion, we maintained coal and coal/ReEF SL mixture at the same feed rate, 0.5 g/min. Since sulfur content in fibers and plastic is negligible, coal is counted as the only source of sulfur. To compare the desulphurization capacity of ReEF SL with the corresponding sorbent Sorbacal lime, we maintained the same Ca/S ratio (Table 2.2) in coal/ReEF SL mixture and coal/SL mixture, which is the ratio of white column to black column of each feed type in Figure 2.2. At the same time, we kept the same coal content in coal and coal/SL mixture, after calculation the feed rate would be 0.56 g/min for coal/SL mixture. By the same method, we worked out all the feed rates for each feed materials.

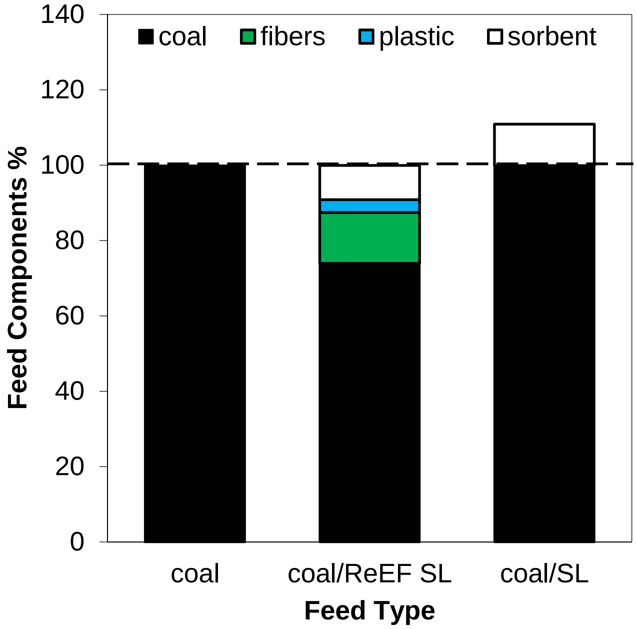

Figure 2.2. Components of the three feed types.

2.2.3 Analytical Methods

Sampled flue gas circulated through an infrared spectrometer (MKS MultiGas 2000), followed by flow through a heated sampling line from the outlet port of the spectrometer cell to a residual gas analyzer. The IR gas cell had a path length of 5.11 meters and 200 mL volume, with antireflection coated ZnSe windows. The gas cell was maintained at a constant 191 °C for comparison to gas concentration standards. The residual gas analyzer was a MKS Cirrus 2 model of quadrupole mass spectrometer with 200 amu mass range.

The crystalline structure of slag samples was determined using X-ray diffraction (XRD, a Philips powder diffractometer, model X'Pert system), with CuKα radiation (λ =

1.54 Å) and an X'Celerator detector. An accelerating voltage of 45 keV was used at a current of 40 mA. Patterns were obtained at a scan speed of (2θ) 7.73°/min. Slag samples were finely ground to ensure random orientation of the crystals so that there were detectable signals at all angles. Also, slag powder was compacted between two glass slides, so that the plane of the powder was aligned with the holder surface.

Experiments were conducted by co-firing coal with ReEF to evaluate combustion performance and emissions reduction. SO_2 and NO_x emissions were measured for all experimental conditions, allowing for comparison between coal, coal/sorbent, and coal/ReEF mixtures. Finally, solid slag and fly ash samples were collected and analyzed by XRD to support the mechanism of in situ sulfur capture by the formation of sulfate salts.

2.3 Combustion Efficiency

Conversion of coal, coal/ReEF and coal/sorbent mixtures was characterized by the permanent gas combustion efficiency, which is an indirect measure of the effectiveness by which heat is generated during combustion. Carbon dioxide and carbon monoxide are also indicators of the reactor capability for converting the complex solid feedstocks to single-carbon gases, for which we calculate the carbon conversion by Equation 2.5,

$$\text{Carbon Conversion}= \frac{\text{Carbon in } CO_2 \text{ and CO from measurement}}{\text{Total carbon content in feedstock}} \tag{2.5}$$

Carbon monoxide emissions ranged between 4 and 6000 ppm for all five blends and comprised less than 2% of carbon content in the feedstock, making CO a minor product compared with CO_2. The results of carbon conversion are compared in Figure 2.3. Carbon conversion during combustion was higher at 1400 °C and 1600 °C than that at 1200 °C. Carbon combustion efficiency increased with addition of ReEF to coal, which was likely due to the relative ease with pyrolysis and combustion of fibers and plastic. Carbon conversion of coal/ReEF mixtures with Na-based sorbent increased by 20-30%, implying that it burned more efficiently than mixtures with Ca-based sorbent. This may be attributed to the degree of excess air, which was 43-46% for coal/ReEF SB and coal/ReEF Trona compared with only 21% for coal (Table 2.4). At 1200 and 1400 °C, combustion efficiency of coal/ReEF ML was higher than that of coal/ReEF SL by as much as 15%.

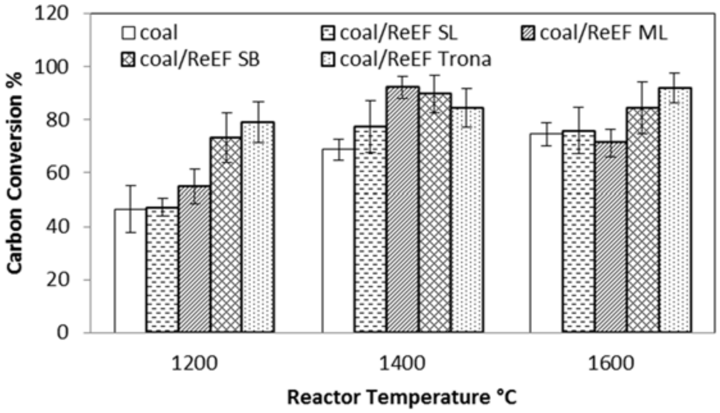

Figure 2.3. Carbon conversion of coal and coal/ReEF mixtures combustion to CO and CO_2 at temperatures 1200, 1400, 1600 °C.

One challenge for efficient combustion of coal/ReEF mixtures may result from melting of sorbent. For example, mixtures of coal/ReEF with Na-based sorbent agglomerated at all three temperatures, since the melting point of sorbents are quite low (50 °C for $NaHCO_3$ and 70 °C for Trona). Sintering has been reported for sodium bicarbonate at temperatures above 316 °C. [39] In experiments, coal/ReEF mixtures with Na-based sorbent fed through the drop tube and augered more smoothly than mixtures with Ca-based sorbent. Despite these issues, high combustion efficiency of coal/ReEF mixtures indicates that ReEF can be mixed with coal in pulverized coal combustors and achieve steady-state combustion for energy production.

2.3.1 Combustion Efficiency for Coal/sorbent Mixture

Enhanced carbon conversion of coal/ReEF mixture combustion proves ReEF as a promising feedstock for coal co-firing, offering economic and environmental benefits. For all four ReEF materials, carbon conversion at 1400 °C was the highest. As less clotting as possible, 1400 °C would be the optimal temperature for co-firing of coal and ReEF. Though sintering problem for coal/ReEF mixture containing Ca-based sorbent occurs only at 1600 °C, Na-based sorbent is not that sticky as Ca-based sorbent. Coal/ReEF with Na-based sorbent fed more easily, thus reducing mechanical problems. Figure 2.4(b) shows carbon conversion of coal/Ca-based sorbent mixture was higher than that of the corresponding coal/ReEF mixture at each temperature generally, whereas in Figure 2.4(c) coal/Na-based sorbent mixture was lower than coal/ReEF with Na-based sorbent. This confirmed that ReEF containing Na-based sorbent burned more sufficiently than ReEF containing Ca-based sorbent in combustion. At 1200 °C and 1600 °C coal/ReEF Trona performed better than coal/ReEF SB by 5%. While at 1200 °C and 1400 °C, combustion efficiency of coal/ReEF ML was higher than that of coal/ReEF SL up to 15%. Since Mississippi lime is a nature material and much cheaper than commercial Sorbacal lime, it’s more economical to use ReEF ML compared with ReEF SL for similar performance. In Figure 2.4(a) carbon conversion of each coal/sorbent mixture is higher than that of pure coal. This may attribute to the higher feeding rate of coal/sorbent mixtures (Table 2.4). It is impossible to achieve perfect blending and control exact feeding rate, thus more feeding may result in higher combustion efficiency.

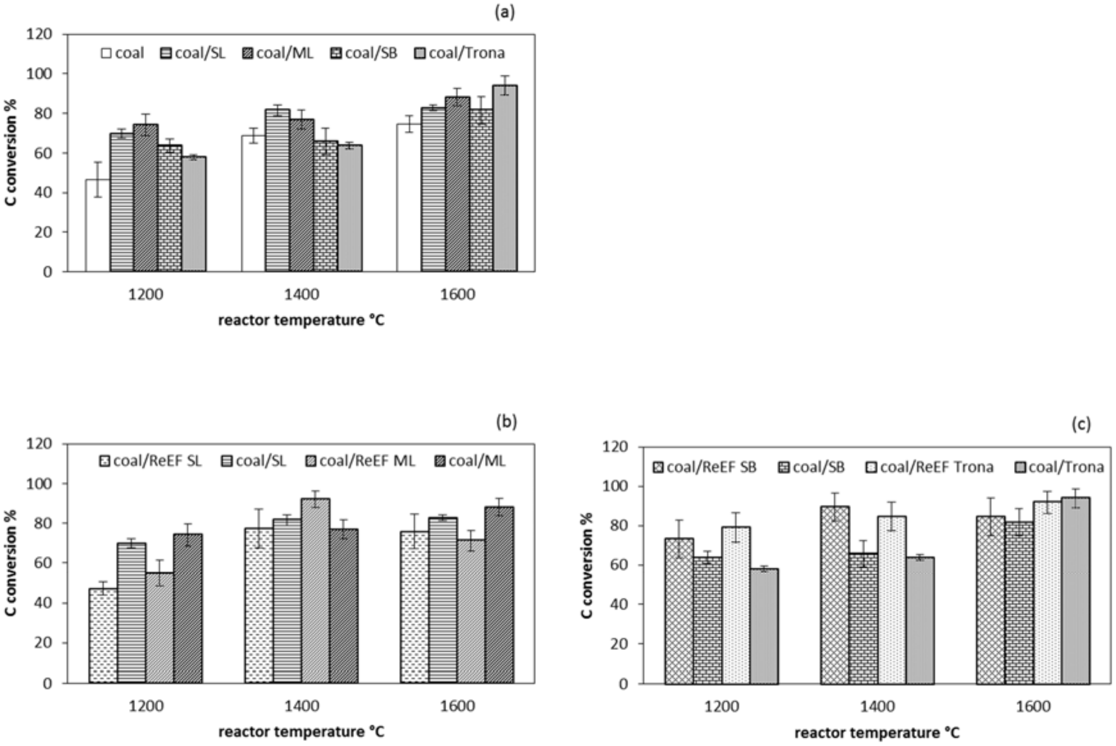

Figure 2.4. Carbon conversion at temperatures, 1200, 1400, 1600 ℃. *(a) coal and coal/sorbent mixtures; (b) mixtures containing Na-based sorbent; (c) mixtures containing Ca-based.*

2.4 SO_2 Emission Reduction

Emission of SO_2 in flue gas from the experimental reactor was found to strongly depend on the addition of sorbent, sorbent type, and reaction temperature. To evaluate SO_2 removal efficiency for each ReEF, we defined SO_2 reduction by Equation 2.6,

$$SO_2 \text{ reduction}= \frac{\text{Theoretical } SO_2 \text{ emission from combusted feedstock-Measured } SO_2\text{concentration}}{\text{Theoretical } SO_2 \text{ emission from combusted feedstock}} \qquad (2.6)$$

Desulfurization performance of coal/ReEF and coal/sorbent mixtures are shown in Figure 2.5, with SO_2 flue gas concentration for pure coal combustion ranging 600~800 ppm from 1200 °C to 1600 °C. By co-firing with ReEF, SO_2 emissions were reduced to less than 200 ppm as shown in Figure 2.5(a). Percentage SO_2 reduction shown in Figure 2.5(d)-(f) demonstrates significant capability of numerous sorbents for removal of SO_2

emission in combustion flue gas by ReEF, with 70~85% of SO_2 reduction achieved for each temperature. Only minor differences of SO_2 reduction was observed between four coal/ReEF mixtures. For example, the maximum difference is 15% between coal/ReEF SL and coal/ReEF SB at 1200 °C (Figure 2.5(d)). For ReEF, adsorption capacity did not significantly vary with temperature. However, ReEF with Na-based sorbents at 1200 °C and 1600 °C, demonstrated a measureable advantage in SO_2 reduction relative to ReEF with Ca-based sorbents (Figure 2.5(d)).

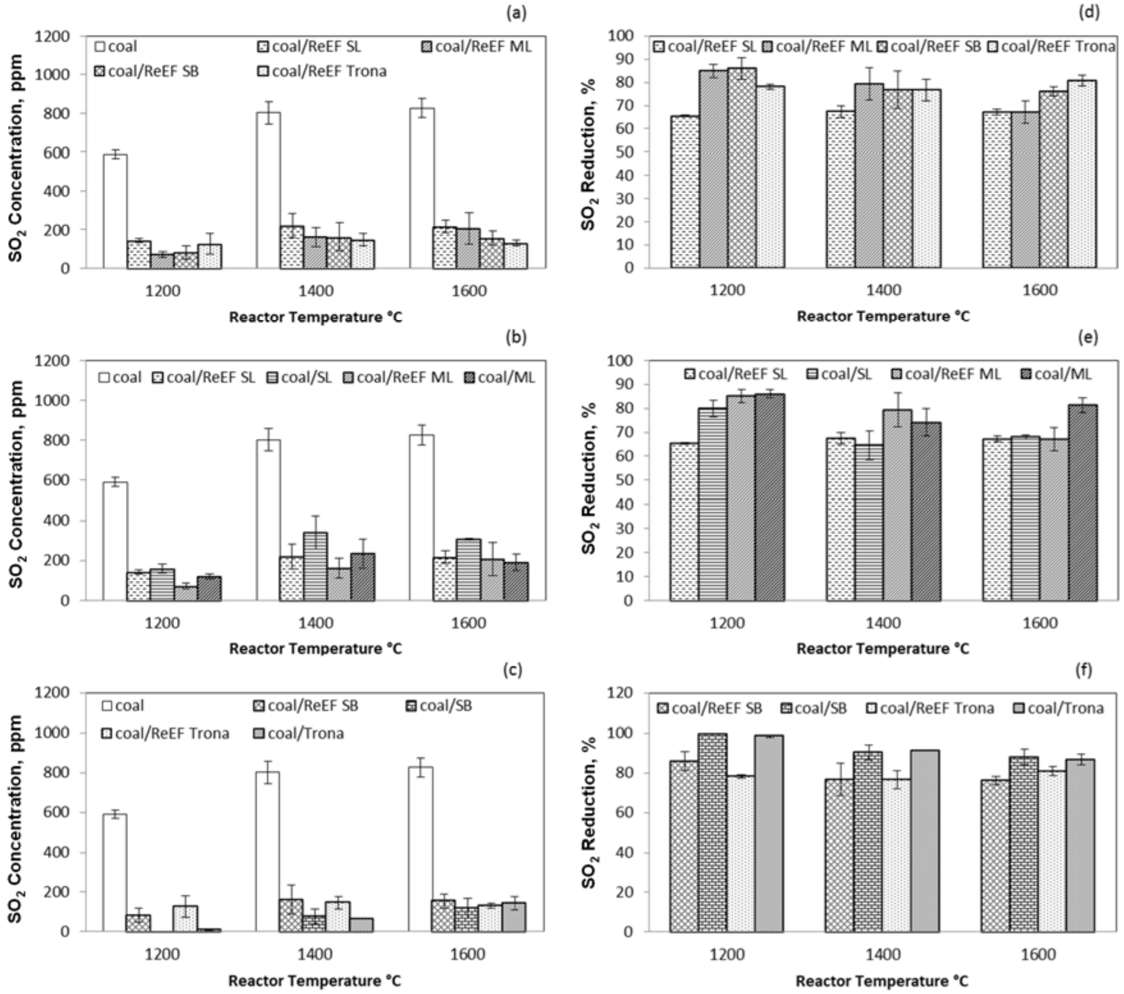

Figure 2.5. Effect of ReEF on sulfur emissions. *The left column is SO_2flue gas concentrations for coal, ReEF and sorbent feedstocks at temperatures 1200, 1400, 1600 ℃: (a) coal and coal/ReEF mixtures; (b) coal and mixtures with Ca-based sorbent; (c) coal and mixtures with Na-based sorbent. The right column depicts extent of SO_2 reduction for coal, ReEF and sorbent feedstocks at temperatures 1200, 1400, 1600 ℃: (d) coal/ReEF mixtures; (e) mixtures with Ca-based sorbent; (f) mixtures with Na-based sorbent.*

Of particular interest to ReEF performance is variation in sorbent surface area. For example, Sorbacal lime is a type of calcium hydroxide which has higher surface area than Mississippi lime. From previous research, higher surface area has led to higher sulfur retention in coal combustion. [34], [35], [49]–[51] However, we observe the opposite trend, such that ReEF with Mississippi lime has slightly better SO_2 removal than Sorbacal lime under the same Ca/S conditions, especially at 1200 °C and 1400 °C (Figure 2.5(b) and (e)). Similar to the combustion efficiency of these two fuels, this further confirmed that ReEF ML exhibited better combustion and emission-capture performance than ReEF SL. As shown in Figure 2.5(b) at each temperature, both coal/ReEF SL and coal/ReEF ML result in less SO_2 flue gas than coal/SL and coal/ML. Furthermore, in Figure 2.5(e) at 1400°C, SO_2 reduction of both coal/ReEF is comparable with coal/Ca-based sorbents. These results indicate that Ca-based sorbent embedded within ReEF capture SO_2 emissions with comparable efficiency to direct utilization of Ca-based sorbents.

While sorbents and ReEF materials do not exhibit dramatic differences in sulfur capture (Figure 2.5), slightly better sulfur capture of Na-based sorbents is consistent with previous studies that have shown Na-based sorbents to have higher reactivity toward SO_2 compared to Ca-based sorbents in dry injection systems. [52] As shown in Figure 2.5(c), coal combustion utilizing ReEF with Na-based sorbent emits very low SO_2 concentrations in the flue gas with only 100~150 ppm. Though the SO_2 concentration and reduction of both ReEF SB and ReEF Trona are nearly the same in Figure 2.5(c) and (f), the (Na/2)/S ratio of ReEF SB is 2.0, which is significantly smaller than that of ReEF Trona (Table 2.2) which is 2.8. Therefore, on a per-sodium-basis, ReEF SB has higher SO_2 adsorption capacity. While the coal/Na-based sorbent mixture performs better than coal/ReEF at 1200 and 1400 °C (Figure 2.5(c) and (f)), ReEF with Na-based sorbent provides comparable sulfur capture performance at 1600 °C.

2.4.1 SO_2 Reduction for Coal/sorbent Mixture

Though the combustion efficiency of ReEF Trona was a little bit higher than that of ReEF SB, considering flue gas desulphurization as a more crucial factor, it's better to choose ReEF SB compared with ReEF Trona. For coal/sorbent mixtures in Figure 2.6, SO_2 concentration in the flue gas by Na-based sorbent is much lower than that by Ca-based sorbent at each temperature (Figure 2.6(a)). Even at 1200 °C, SO_2 emission of Na-based sorbent is less than 10 ppm and SO_2 reduction has reached 99% (Figure 2.6(b)). This is in accordance with literature that Na-based sorbent has a high degree of desulphurization. Figure 2.6(b) shows Na-based sorbent adsorbs about 20% more SO_2 than Ca-based sorbent at each temperature, which further confirms Na-based sorbent is superior to Ca-based sorbent on SO_2 reduction.

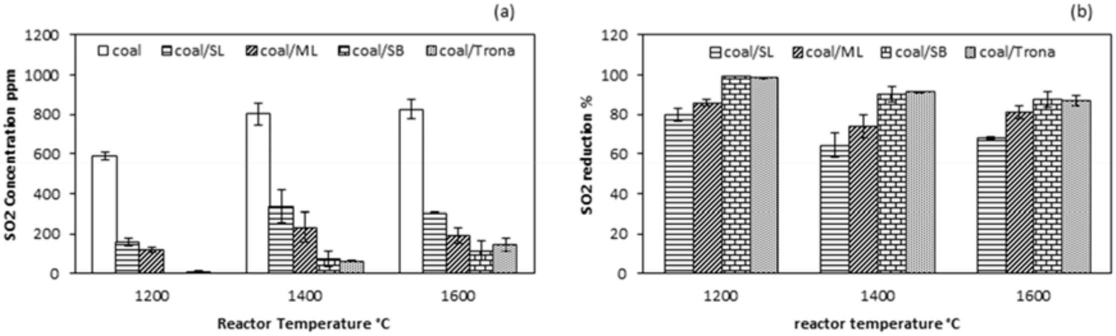

Figure 2.6. Effect of sorbent on SO_2 emission. *(a) SO_2 flue gas concentrations for coal and coal/sorbent mixtures at temperatures, 1200, 1400, 1600 ℃; (b) SO_2 reduction for coal/sorbent mixtures at temperatures, 1200, 1400, 1600 ℃.*

2.5 NO Emission Reduction

Emissions of nitric oxide (NO) from the combustion of coal, coal/ReEF and coal/sorbent mixtures were observed to vary from 50-350 ppm, with negligible quantities of NO_2 observed. Elemental nitrogen in coal was 1.8 wt%, but negligible quantities were measured in the ReEF materials as shown in Table 2.1. Figure 2.7(a) shows the concentration of NO emission from coal and coal/ReEF mixtures, with only a small decrease in NO concentration for all coal/ReEF mixtures compared with coal at 1200 °C. However, the extent of NO production at 1400 and 1600 °C is significantly reduced, decreasing from ~250 ppm for coal to 150-200 ppm for all coal/ReEF mixtures.

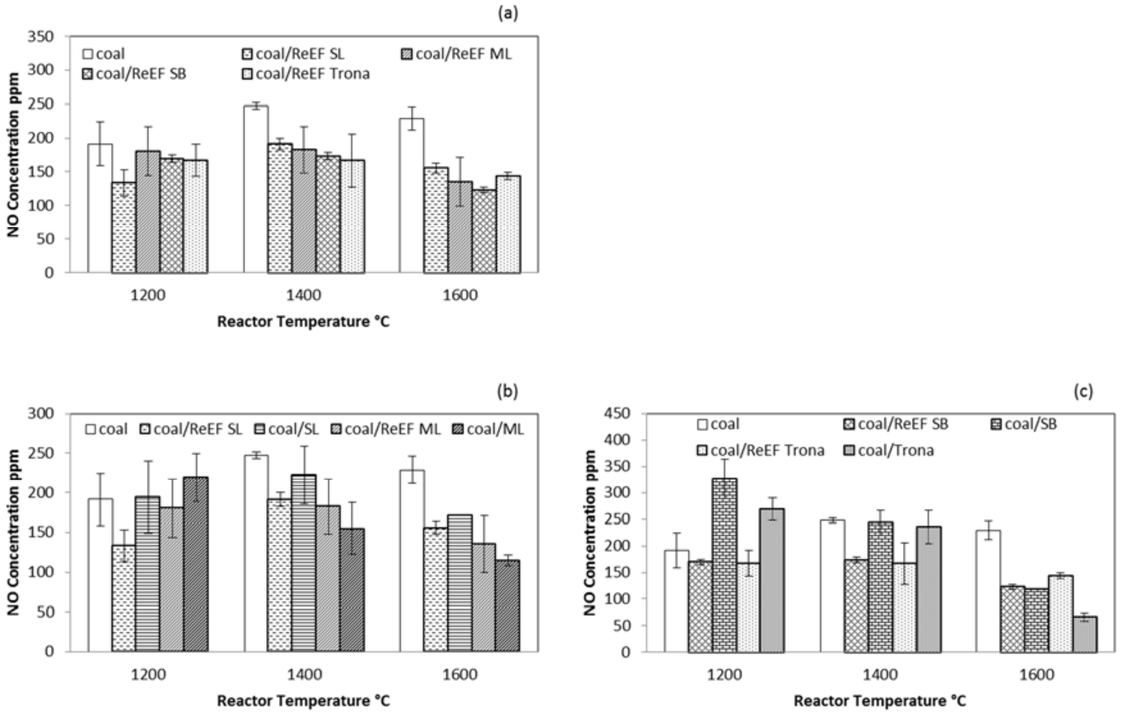

Figure 2.7. Effect of ReEF on NO$_x$ emissions. *Nitric oxide (NO) emission concentrations for different feedstock at temperatures 1200, 1400, 1600 ℃: (a) coal and coal/ReEF mixtures; (b) coal and mixtures with Ca-based sorbent; (c) coal and mixtures with Na-based sorbent.*

Comparison of calcium- and sodium-based sorbents with ReEF indicates slightly superior NO$_x$ emission reduction from ReEF materials. Figure 2.7(b) shows that coal/ReEF SL and coal/ReEF ML have comparable NO emission to coal and coal/sorbent mixtures at 1200 °C. However, ReEF with Sorbacal lime exhibited statistically better NO reduction at 1400 and 1600 °C, coal/ReEF ML experiments at these temperatures were statistically the same. In contrast, both Na-based sorbent containing ReEF exhibited superior NO emissions reduction at 1200 and 1400 °C than pure coal and coal/sorbent feeds, as shown in Figure 2.7(c). These results imply that embedding Na-based sorbent within ReEF is more effective than direct utilization of Na-based sorbents on flue gas capture. At 1600 °C, all coal/sorbent and coal/ReEF mixtures exhibited significant NO emission reduction compared to the pure coal feed.

Generally, NO in flue gas can be generated from three sources: (a) oxidation of nitrogen in the fuel (fuel-bound NO), (b) oxidation of molecular nitrogen from air (thermal NO), and (c) reaction between fuel radicals and atmosphere nitrogen (prompt NO). Prompt NO can be produced directly in the combustion flame zone where the molecular nitrogen reacts with hydrocarbon fragments from fuel. Although we couldn't quantify how much NO emission formed from the prompt NO pathway, it is reported that prompt NO is usually negligible compared to thermal NO. [53] When the reactor temperature exceeds 1600 °C, molecular nitrogen and oxygen react to form thermal NO_x (mostly NO, with smaller amounts of NO_2), with more NO_x produced as temperature increases. As reported in other studies, combustion of coal in air produced 20% more NO_x than in a nitrogen-free atmosphere. [54] The amount of NO also depends on the extent of excess oxygen.

Excess air for coal/ReEF mixtures was about twice that for coal (Table 2.4) which could lead to increased thermal NO generation. However, Figure 2.7(a) shows a decrease of NO concentration for coal/ReEF blends from 1200 to 1600 °C. The reduction in NO formation with ReEF co-feeds can be attributed to either the carbon in the biomass/waste component of ReEF or the sorbent. NO can react with char to form molecular nitrogen. [55]

$$C + NO \rightarrow \tfrac{1}{2}N_2 + CO \tag{2.7}$$

$NO + CO \rightarrow \frac{1}{2}N_2 + CO_2$ (2.8)

Alternatively, lower NO emission can be due to reaction directly with the sorbents; in general, coal/ReEF mixtures emitted 50~100 ppm less NO than pure coal (Figure 2.7(a)). Calcium oxide has previously been studied in pulverized coal combustion and was observed to significantly reduce emissions of both NO and CO. [56] Sodium bicarbonate can be a sorbent for both SO_2 and NO removal. [57]

$NO + \frac{1}{2}O_2 \rightarrow NO_2$ (2.9)

$Na_2CO_3 + 2NO_2 + \frac{1}{2}O_2 \rightarrow 2NaNO_3 + CO_2$ (2.10)

Because mixtures of both coal and pure sorbent also exhibited significant NO reduction (Figure 2.7(b) and (c)) when compared with pure coal conditions, this indicates that the sorbent has a strong effect on NO reduction within the ReEF particle.

2.5.1 NO Reduction for Coal/sorbent Mixture

Generally, coal/ReEF with Na-based sorbent release less NO than coal/ReEF with Ca-based sorbent. This corroborate ReEF with Na-based sorbent works better than ReEF with Ca-based sorbent in coal combustion emission control. In Figure 2.8, NO emission of coal/Na-based sorbent decrease faster than coal/Ca-based sorbent when temperature increases. The adsorption capacity of Na-based sorbent is more temperature sensitive than Ca-based sorbent. This is in accordance with Na-based sorbent functions well at high temperature. At 1200°C, coal/sorbent mixtures produce more NO than pure coal. On one hand, the feeding rate of coal/sorbent mixtures is a bit more. On the other hand, Na-based sorbent didn't react thoroughly with SO_2 at low temperature.

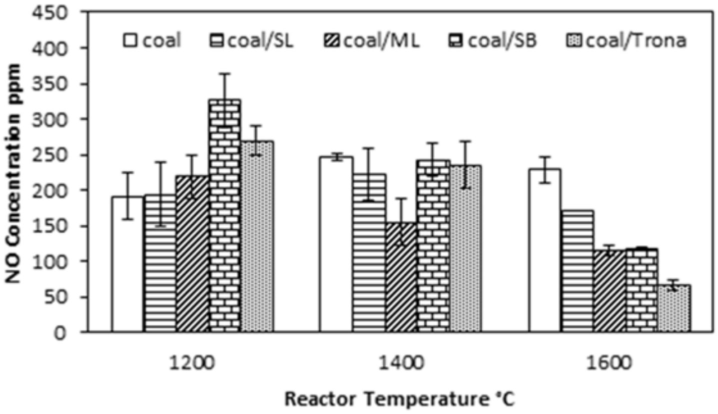

Figure 2.8. NO emission concentration for coal and coal/sorbent mixtures at temperatures, 1200, 1400, 1600 °C.

2.6 Characterization of Slag Ash

Crystallites of slag powder collected from the bottom slag hopper during coal/ReEF combustion were characterized by X-ray diffraction (XRD) to demonstrate sulfur uptake (desulfurization) by Ca-based and Na-based sorbents. XRD patterns were scanned in the 2θ range from 10° to 60°; significant background noise exists in the XRD patterns due to the complexity of bituminous coal in the sample. Figure 2.9 shows the XRD pattern of coal/ReEF ML mixture and coal/ReEF ML slag at 1400 °C. The presence of quartz in the coal/ReEF ML can be observed at 2θ = 22.0°, 27.0°, 36.2° and 42.7°. The intense silicon dioxide peak still exists in the coal/ReEF ML slag, indicating the post-reaction presence of the original quartz. The dominant peaks from commercial Mississippi lime at 2θ equal to 18.3°, 28.9°, 34.4°, 47.3°, 51.0° and 54.1° show that hydrated lime is in the ReEF feedstock and well mixed with coal. Only a low intensity calcium hydroxide peak is observed from the coal/ReEF ML slag, indicating that most sorbent had reacted or decomposed. The XRD pattern of the slag powder indicates that the product slag is mostly anhydrous calcium sulfate (through peaks observed at 2θ: 29.6°, 31.6°, 31.9°, 32.7°, 39.0° and maximum intensity at 25.8°). Mississippi lime from ReEF has also been captured in the fly ash mixed with flue gas. The presence of CaO was found in the XRD pattern of the slag sample (not shown), and excellent agreement with expected CaO patterns was observed at 2θ = 31.9°, 37.6° and 54.1°. Some hydrated lime decomposed to CaO during combustion since the Ca/S ratio was 3.1 for coal/ReEF ML mixture (Table 2.2).

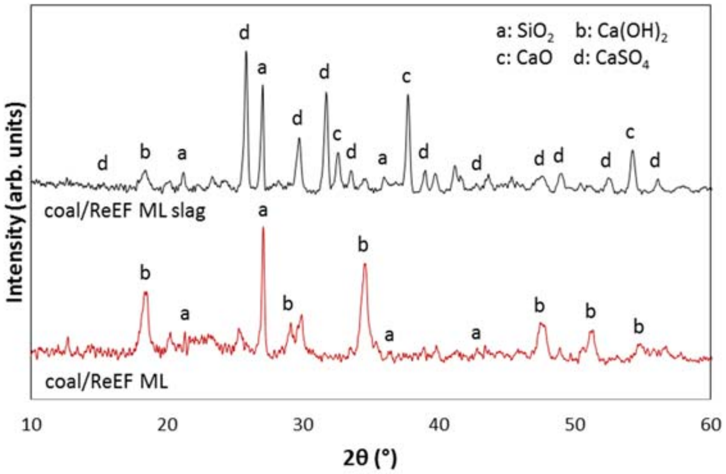

Figure 2.9. XRD pattern of coal/ReEF ML mixture and coal/ReEF ML slag at 1400 °C.

Figure 2.10 shows the XRD pattern of coal/ReEF SB mixture and coal/ReEF SB slag at 1400 °C. Peaks consistent with silicon dioxide were again observed. The XRD pattern of coal/ReEF SB was compared with that of sodium bicarbonate with excellent agreement (through peaks observed at 2θ = 25.9°, 30.1°, 34.9°, 41.1° and 47.7°) which indicates that sodium bicarbonate in ReEF was well-mixed with coal. No $NaHCO_3$ characteristic peak was observed in the measured XRD pattern of coal/ReEF SB slag sample, which implies that $NaHCO_3$ fully decomposed to Na_2CO_3 or adsorbed SO_2. It has been shown that the final desulfurization product by sodium bicarbonate is a mixture of fly ash and sodium salts (sodium chloride, sodium sulfate, sodium fluoride, sodium carbonate and so on) known as Residual Sodium Chemicals (or RSC). [38] However, no solid products connected with desulfurization were identified by XRD in the coal/ReEF SB slag samples (Na_2SO_4, Na_2SO_3, $Na_2S_2O_3$, Na_2S and Na_2CO_3). Wang et al. [58] revealed the existence of two sodium carbonate sulfate double salts as desulfurization products that were similar to a better-known mineral, burkeite — $Na_6(CO_3)(SO_4)_2$. The two double salts were believed to have high porosity and specific surface area which is favorable to the sulfation process. Since the (Na/2)/S ratio is 2 for coal/ReEF SB (Table 2.2), there should be at least as much Na_2CO_3 as Na_2SO_4 in the slag. It should also be noted that the melting point of Na_2SO_4 and Na_2CO_3 are 884 °C and 851°C, respectively. At high temperature, the formation of the double salts can be produced through crystallization from melting aqueous phases of Na_2CO_3 and Na_2SO_4. The proportion of the groups SO_4^{2-} and CO_3^{2-} in the double salts is variable.

$$Na_2CO_3 + Na_2SO_4 \rightarrow Na_4(CO_3)(SO_4) \tag{2.11}$$

$$2Na_2CO_3 + Na_2SO_4 \rightarrow Na_6(CO_3)_2(SO_4) \tag{2.12}$$

Peaks typical of burkeite were found in coal/ReEF SB slag samples (2θ = 21.4°, 23.3°, 25.3°, 26.8°, 32.0°, 33.4° and 34.9°). Observation of sodium-containing sulfates demonstrates that sodium bicarbonate in ReEF has effectively captured sulfur for retention in slag solids.

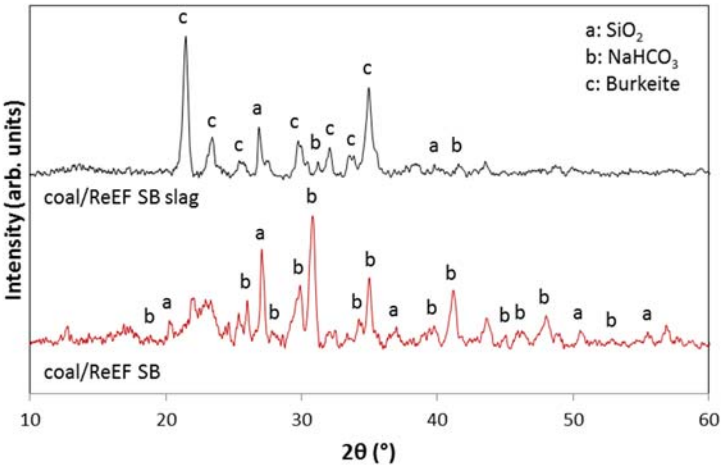

Figure 2.10. XRD pattern of coal/ReEF SB mixture and coal/ReEF SB slag at 1400 °C.

2.7 Mechanism of Co-combustion of Coal and ReEF

The proposed mechanism of integrated sorbents/RDF in ReEF for co-combustion with coal is illustrated in Figure 2.11. As solid feed and reactant gas enter the bottom of the reactor, the fibers and plastics undergo endothermic pyrolysis and protect inorganic sorbents from exposure to high temperature, thus minimizing sintering and/or slagging while the coal burns to release SO_2. When ReEF fragments travel upward and are combusted, sorbents are released to capture SO_2 flue gas, and any remaining residues continue to combust. Within the convection zone, sorbents desulfurize the flue gas where complete burnout and conversion are achieved. Optimal ReEF design minimizes sintering of the sorbent early in the reactor while maximizing gas absorption later at lower temperatures before exiting as gas/solid products.

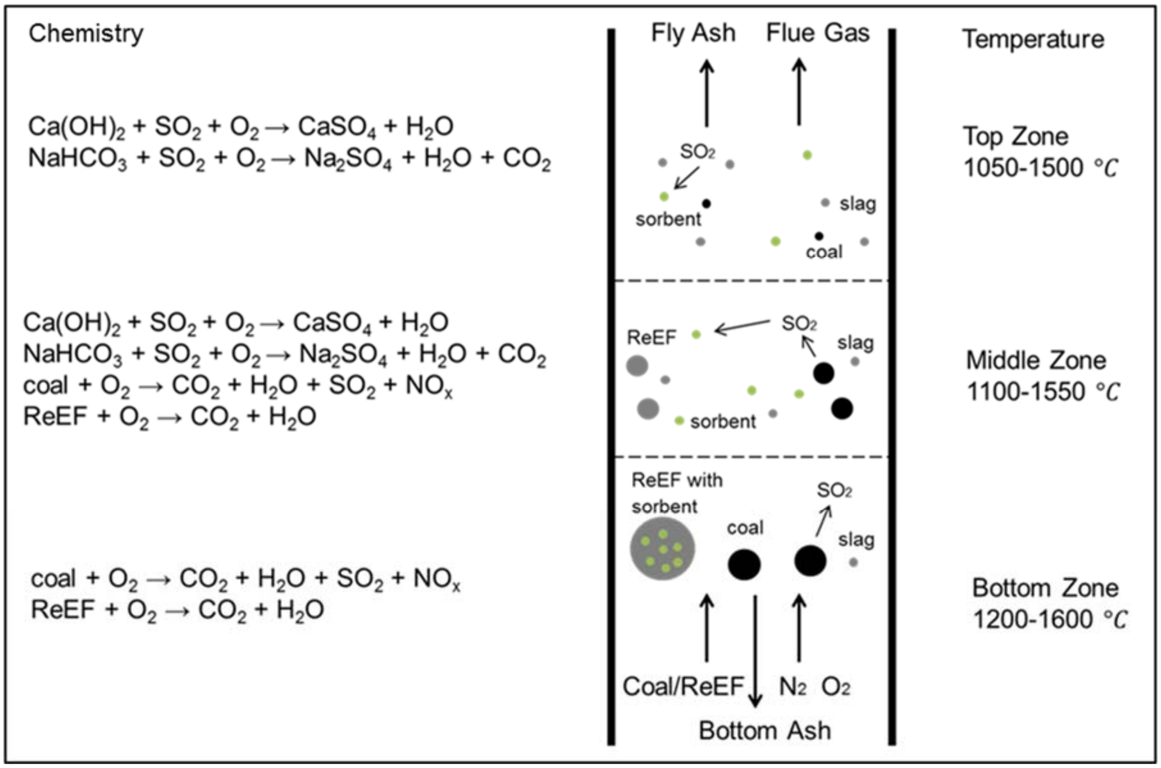

Figure 2.11. Proposed mechanism of co-combustion of coal and ReEF materials. *ReEF pyrolyzes and oxidizes releasing sorbent and producing combustion products,* SO_2*, and* NO_x*. In the middle and top zones, sorbent reacts with oxygen and emissions to form solid sulfate species which are recovered in fly and bottom ash.*

2.8 Conclusions

An experimental study of ReEngineered Feedstock for coal combustion emission control evaluated the fuel for emissions reduction. The results show co-feeding ReEF in coal combustion greatly increases sulfur retention in solid waste (e.g. slag) and slightly decreases NO emission. XRD was utilized to determine the crystallinity and phase of the product solids, which indicated in situ sulfur capture as solid salts. Detailed experimental results are summarized as follows: (1) Enhanced combustion efficiency when co-firing coal and ReEF indicates that ReEF is a promising feedstock for coal combustion. Coal/ReEF mixtures with Na-based sorbent burned more efficiently than mixtures with Ca-based sorbent by 20-30%. (2) Significant reduction of SO_2 emission as high as 70% in combustion flue gas was achieved by premixing coal with ReEF. For the same Ca/S condition, SO_2 reduction by ReEF Mississippi lime (ML) was higher than that by ReEF Sorbacal lime (SL). (3) In general, coal/ReEF mixtures emit less NO than pure coal consistent with less nitrogen content in ReEF. (4) XRD analysis of the slag powder indicates Mississippi lime in ReEF ML effectively captured SO_2 to form calcium sulfate. In addition, sodium bicarbonate in ReEF SB retained sulfur in the slag to form sodium sulfate. The desulfurization product Burkeite forming through crystallization from the melting aqueous phases of Na_2CO_3 and Na_2SO_4 at high temperature was identified in the XRD pattern.

Chapter 3. Sulfation Kinetics of ReEngineered Feedstock on Flue Gas Emissions

3.1 Introduction

The process of converting waste to energy is considered one of the leading methods to achieve maximum energy efficiency and environmental sustainability. Currently, the United States generates about 250 million tons of Municipal Solid Waste (MSW) in 2011 and only about 11.7 % of the waste has been recovered for energy generation. [59] MSW is treated through a series of processes including separation, size reduction, drying and densification, leaving the combustible component called refuse-derived fuel (RDF). RDF has higher heating value and better combustion performance than MSW and can be used for power generation. [60] However, compared with traditional fossil fuels such as coal, RDF has lower energy density. Thus, RDF is commonly used as a second fuel to be co-fired with coal power-generation facilities. Combustion performance and emissions of co-firing RDF and coal have been studied extensively in the last few decades, [9], [27], [28], [61]–[63] and co-firing has gained attention for its benefit in replacing fossil fuels, mitigating greenhouse gases and improving waste management.

Co-firing coal with RDF can reduce CO_2 emissions as RDF is considered to be a CO_2 neutral fuel. Moreover, the low sulfur content in RDF leads to lower SO_2 emissions. However, other pollutants such as hydrogen chloride (HCl) need to be addressed when combusting RDF due to the existence of polyvinyl chloride (PVC). [5], [30], [64] Besides, Cl_2 and HCl emitted from RDF is also an important factor for forming the toxic environmental pollutants—polychlorinated dibenzodioxins and dibenzofurans (PCDDs/PCDFs). [65], [66] The process of reducing flue gas emissions by conventional methods requires construction of scrubbing facilities downstream of power generation facilities, which increases capital and operational costs.

To achieve regulated emission levels, an alternative option is the addition of a third reaction component to decrease pollutants emission via *in situ* sequestration by inorganic sorbents. Commonly, calcium-based sorbents such as calcium oxide, calcium hydroxide and calcium carbonate have been shown effective at removing SO_2 emissions. [67]–[71] Recently, injection of calcium sorbents has also been shown to reduce HCl emissions. [5], [27], [72] Other than emission control, additive inorganic compounds in RDF can serve as binders to densify 'fluffy' RDF. Daugherty et al. examined over 150 potential binders and binder combinations in 1986 [42] with the aim of developing a low-cost binder that would improve combustion of densified RDF pellets. Calcium hydroxide was identified as the top-performing binding agent. [43] In terms of pollutant emission control, Ohlsson carried out a full scale co-combustion test using 88 wt% coal and 12 wt% of densified RDF bonded with 4 wt% calcium hydroxide. The test was conducted in a 440 MW cyclone-fired combustor in a two day period. The results showed that sulfur dioxide was reduced by 17% compared with conventional feeding of coal, with slight decrease in NO_x also observed in their study [43].

3.1.1 ReEngineered Feedstock Technology

In the previous chapter, utilization of sorbent-containing RDF as a fuel substitute and sorbent in coal power facilities has been extended in my study. [73] A new fuel matrix identified as ReEngineered Feedstock^{TM} (ReEF), developed by Accordant Energy Inc.

(Formerly ReCommunity Energy Inc), was evaluated for co-firing with coal in a laboratory scale combustor for its combustion and desulfurization capability. ReEF integrated calcium/sodium inorganics into refuse-derived fuel to achieve both energy generation and emissions control during pulverized coal combustion. Up to 85% of sulfur dioxide reduction was observed when co-firing coal and ReEF.

ReEF was prepared and processed by Accordant Energy, LLC. Collected municipal, institutional and commercial wastes were treated through a series of separations in the Material Recovery Facility (MRF), resulting in different waste streams such as recyclable fibers, recyclable plastics, metal and inert materials. The non-recyclable plastic was further treated by a two-step thermal process to remove chlorine. Materials used in ReEF primarily consisted of non-recyclable fibers and low chlorine content plastics, [7], [8], [74] Sorbent was mixed with hard plastics at temperatures exceeding 200 °C to ensure encapsulation of sorbents into the profile of hard plastics. Finally, the selected soft plastics and fibers were metered and mixed with hard plastics and sorbent to pelletize into ReEF, [75] as shown in Figure 3.1.

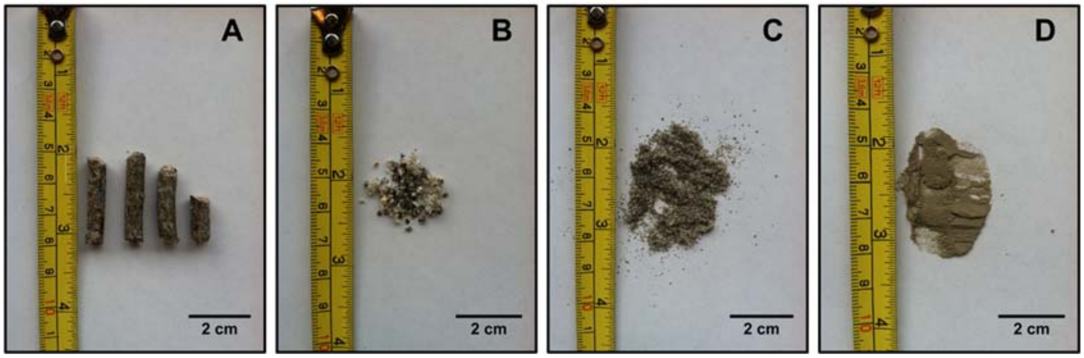

Figure 3.1. Pelletized and ground ReEngineered Feedstock (ReEF). *Pellets of ReEF (A) were ground and sieved to (B) particle sizes larger than one millimeter, (C) particles between 212-500 µm, and (D) particles between 25-53 µm.*

In this work, 35 wt% of high surface area calcium hydroxide (Sorbacal® SP) was selected as sorbent and mixed with 52 wt% non-recyclable fibers and 13 wt% non-recyclable hard plastics to form fuel matrix. Table 3.1 lists the elemental analysis of ReEF, determined by Galbraith Laboratories Inc. [76] Compared to other secondary fuel such as wood waste and agricultural residues, [77] ReEF has lower volatile matter and lower fixed carbon but more ash content. The ash content primarily derives from the sorbent added during the material production process. Low nitrogen and sulfur content was also observed in ReEF. Other than calcium, we also observed silicon, chlorine, aluminum, sodium and magnesium. These components derive from the waste stream, and composition may vary depending on the type of waste selected for inclusion in ReEF. [78] The heat of combustion was measured to be 5787 Btu/lb, which is about half to one third the value of bituminous coal. [79]

Table 3.1. Elemental analysis of ReEngineered Feedstock.

Proximate Analysis (wt%)		**Elements (wt%)**	
Moisture	1.24	Calcium	22.9
Volatile Matter	59.61	Silicon	1.05
Fixed Carbon	5.33	Chlorine	0.69
Ash	33.76	Aluminum	0.66
Ultimate Analysis (wt%)		Sodium	0.41
Carbon	33.76	Magnesium	0.25
Hydrogen	5.08	Iron	0.18
Oxygen	26.11	Potassium	0.04
Nitrogen	0.06	**Heat of Combustion (BTU/lb)**	5787
Sulfur	0.04		

3.2 Experimental Methods

In this study, ReEF containing calcium hydroxide (Sorbacal® SP) was characterized for its morphology and desulfurization capability at combustion conditions. A vertical drop tube reactor system was utilized for continuous characterization of simultaneous combustion, calcination, and desulfurization reactions. To evaluate the effects of combustion conditions on sorbent calcination and sulfation, a horizontal calcination reactor system was utilized for short-time exposure and sampling.

3.2.1 Material Characterization Methods

Particle size distribution of ReEF was determined by sieving pulverized ReEF through a series of U.S. Standard sieves. ReEF was separated into particle size groups: (a) smaller than 25 µm, (b) 25-53 µm, (c) 53-212 µm, (d) 212-500 µm, (e) 500-1000 µm, and (f) larger than 1000 µm. Carbon content was determined by the Galbraith Laboratories, Inc. [76] for each particle size. Calcium hydroxide content variation across particle sizes was characterized by EDTA titration.

The surface area of pure calcium hydroxide and pulverized ReEF particles was measured by nitrogen adsorption at a temperature of -196 °C using Autosorb-1 from Quantachrome Instruments. Degassing of the sample was conducted at 99 °C, and complete degas was achieved when the pressure difference was lower than 25 mtorr. The surface area was calculated using the BET equation and total pore volume was measured at the relative pressure of $P/P^{sat} = 0.95$.

Scanning electron micrograph (SEM) images and elemental mapping of ReEF particles were obtained with an FEI SEM Magellan 400. An accelerating voltage of 3 kv, 7 kv and a current of 50 pA, 0.2 nA was applied for SEM images and EDX mapping, respectively. Ashes collected from ReEF combustion and desulfurization were analyzed by X-ray diffraction with a Philips powder diffractometer, model X'Pert system. The XRD pattern was obtained with an accelerating voltage of 45 kv and a current of 40 mA.

3.2.2 Sulfation Reactor System

Figure 3.2 depicts the first reactor system utilized for studying the kinetics of ReEF particles undergoing simultaneous combustion, calcination, and desulfurization reactions. Composition and flow rate of gas streams consisting of 1400 ppm SO_2, 5% - 30% (v/v) O_2, and nitrogen was controlled by three thermal mass flow controllers (Brooks Instruments). The reactor consisted of a 1 inch outer-diameter quartz tube on the top, which was reduced to ¼ inch after the reaction to minimize residence time and mixing. The reactor was enclosed in a vertical split furnace (Applied Test Systems). An 8 inch length heating element was embedded in the furnace to achieve a maximum temperature of 1700 °C. One K-type thermocouple was placed above the sample platform to measure temperature. This work utilized reactor temperatures of 800 °C, 900 °C and 1000 °C.

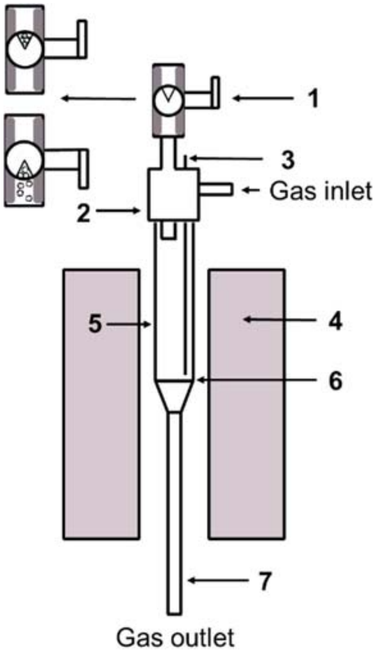

Figure 3.2. Sulfation reactor setup. *Transient sulfation of sorbent was conducted within a 1 inch quartz tube (#5), equipped with a Swagelok tee (#2) which combines gas flows with sorbent injection through a rotary feed valve (#1, amplified in up left corner). Injected sorbent samples are supported within the reactor system on a quartz frit (#6), which is heated by furnace (#4) and monitored with a thermocouple (#3). The reactor downstream reduces to a ¼ inch quartz tube (#7) to minimize residence time, before gases flow to a Bruker Vertex 70 infrared detector.*

In each experimental trial, 10 mg ReEF was loaded into the feeding rotary valve located at the top of the reactor. Gas feed at 1.0 L/min with a concentration of 1400 ppm SO_2 continuously flowed through the reactor system. At the start of the experiment (time zero), ReEF particles dropped into the hot zone (by turning the rotary feed valve) and were supported on a quartz frit located at the bottom of the reactor just prior to the reactor size reducing to ¼ inch. Fibers and plastics from ReEF combusted at once, leaving the sorbent to react with SO_2. Reactor effluent gas was continuously analyzed by an online Bruker Vertex 70 FTIR with a Harrick temperature-controlled gas cell (10 cm path length and 17 ml cell volume), capable of measuring the concentration of SO_2 every 3 seconds.

3.2.3 Calcination Reactor System

A second, horizontal reactor system was utilized for studying the combustion effect on calcination and sulfation of ReEF as shown in the schematic diagram of Figure 3.3. The reactor consisted of a ½ inch diameter quartz tube with Swagelok ultra-torr fittings on both ends. The reactor tube was enclosed in a horizontal split furnace (Thermo Scientific Lindberg/Blue M) with a maximum temperature of 1100 °C. A quartz concave sample holder (1 inch length, ¼ inch depth and width) was attached to a ¼ inch quartz rod. Before calcination, the temperature was set and maintained at constant 800 °C. Specified gas containing oxygen and nitrogen was continuously flowing through the reactor. The sample undergoing calcination was directly inserted via the sample holder into the center of the reactor tube and then collected after a specified time interval. This experimental setup had the advantage of allowing precise control of the duration of sample calcination. Additionally, sorbent could be transferred into the collecting vial immediately after it was taken out of the hot reactor/furnace, and fast cooling minimized potential sorbent sintering. The collected sample was then purged with nitrogen and sealed for *ex situ* analysis.

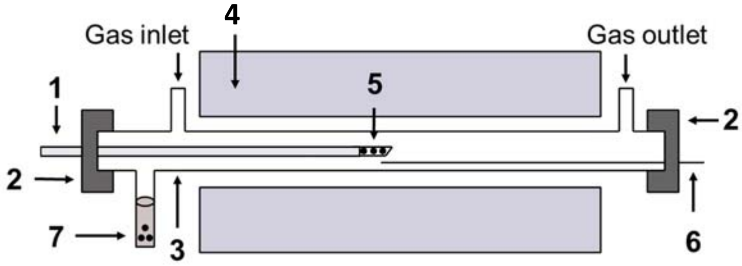

Figure 3.3. Calcination reactor setup. *Calcination of sorbents was evaluated within a quartz reactor (#3) heated with a furnace (#4) and monitored for temperature by a thermocouple (#6). Sorbents were supported within a quartz sample holder (#5), which was moved into and out of the reactor with a quartz rod (#1) sealed with a Swagelok ultra-torr fitting (#2). During experiments, gas continuously entered and exited the system. Following calcination, sorbent samples were transferred to a collection vial (#7) sealed within the reaction system.*

ReEngineered Feedstock^{TM} (ReEF) containing calcium hydroxide as sorbent was compressively characterized in my work. The sulfation of ReEF was conducted in a custom-built drop tube reactor. The effects of combustion of fibers and plastics on sorbent sulfation were analyzed, which revealed the mechanism of ReEF desulfurization.

3.3 Characterization of ReEF

Figure 3.4 illustrates the content of calcium hydroxide and carbon in varying ReEF particle sizes. Calcium hydroxide content decreased from small to large ReEF particles. In contrast, the large particles contain the most carbon, indicative of more fibers and plastics in ReEF. Although sorbent was mixed with RDF in the material preparation process, it may detach from the RDF surface during pulverization due to strong mechanical forces and vibration. The surface area of sieved ReEF particles was analyzed by nitrogen adsorption. As listed in Table 3.2, ReEF particles have lower surface area and pore volume than that of pure calcium hydroxide, which indicates that ReEF is a generally non-porous material consistent with its large proportion of non-porous fibers and plastics.

Table 3.2. Surface area of ReEngineered Feedstock and calcium hydroxide.

Sample	Surface area (m^2/g)	Pore volume ($*10^{-3}$ cm^3/g)
Calcium hydroxide (< 90 μm)	34.8	190
ReEF (<25 μm)	2.5	7.5
ReEF (25-53 μm)	4.1	10.7
ReEF (53-212 μm)	2.4	7.2

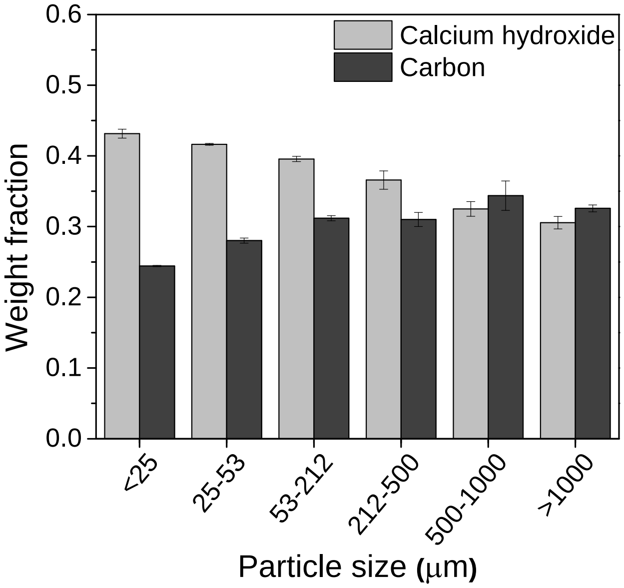

Figure 3.4. Calcium hydroxide and carbon content of ReEF particles.

The geometric aspect ratio of ReEF with varying particle sizes was characterized by microscopic images (visible light) as shown in Figure 3.5. The circularity of each particle size was calculated by Equation 3.1,

$$\mathrm{Ci} = \mathrm{Circularity} = \frac{4\,\pi * \mathrm{Area}}{\mathrm{Perimeter}^2} \tag{3.1}$$

with perfect circles exhibiting Ci=1. Smaller ReEF particles were found to be more circular (with Figure 3.5A, B, and C having circularity of 0.63, 0.58, and 0.41, respectively). Fibrous, stringy particles were observed for sizes between 53-212 μm (Figure 3.5C). Larger particles were formed by the clumping of fibers and plastics as shown in Figure 3.5D. Another property of ReEF particles was their flaky shape, which was visibly different from more spherical coal particles.

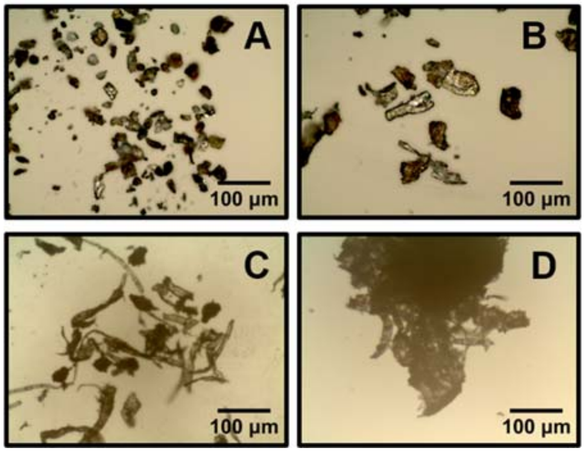

Figure 3.5. Microscopic images of ReEF particles. *Ground ReEF was separated and imaged by light microscopy at particle sizes (A) less than 25 μm, (B) 25-53 μm, (C) 53-212 μm, and (D) 212-500 μm.*

Calcium sorbent distribution on the RDF surface was evaluated using scanning electron microscopy. Figure 3.6A presents the SEM image of a ReEF particle from the sieved group of 25-53 μm. This particle group exhibited small light particles randomly dispersed on the rough surface as shown in Figure 3.6B. Energy-dispersive X-ray spectroscopy (EDX) was used to analyze the white rectangular area in Figure 3.6B, and the results of elemental mapping on the surface are shown in Figure 3.6C and 3.6D. Major elements on the surface were carbon, oxygen and calcium, which are the main elemental components of ReEF. Calcium was detected almost everywhere on the surface, which indicates an even distribution of calcium hydroxide. Other than calcium, detected inorganic elements included sodium, magnesium, aluminum, silicon and chlorine on the surface, which are known resulting from waste materials. The elemental maps of aluminum and silicon overlapped with each other, indicating that these elements derived from the same source (aluminosilicates).

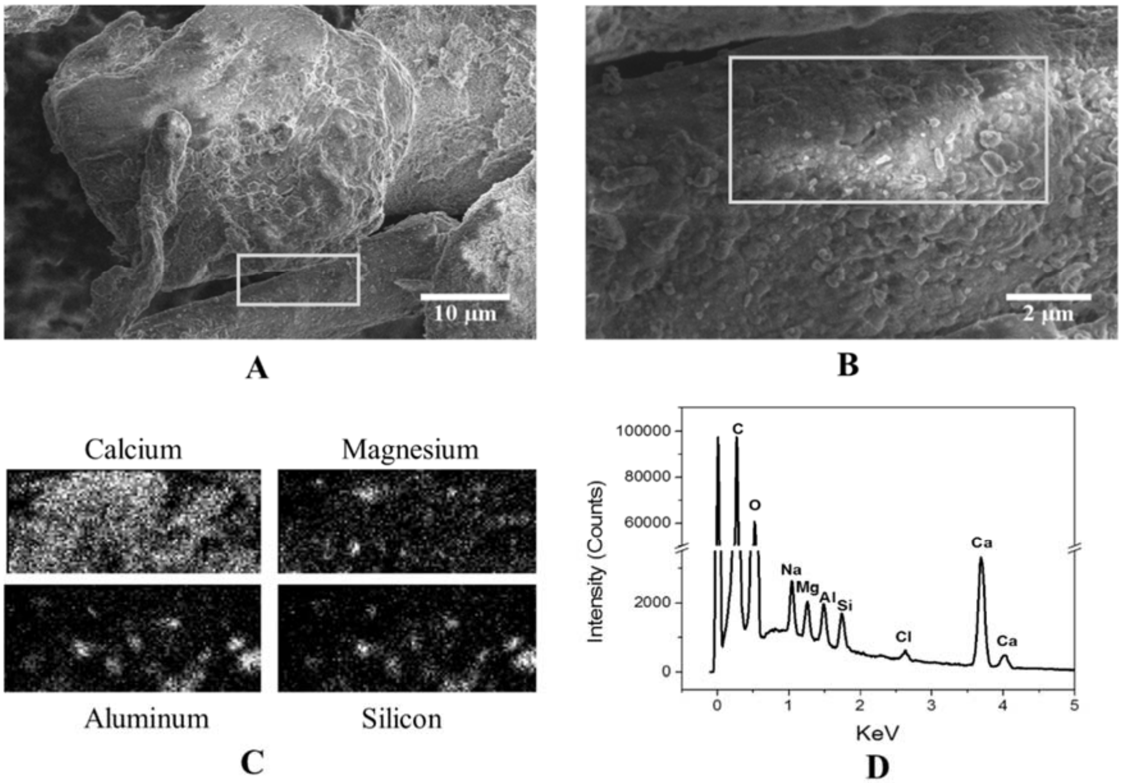

Figure 3.6. SEM-EDX of ReEngineered Feedstock. *(A) SEM image of ReEF (25-53 µm). (B) Enlarged SEM micrograph of white box area in panel A. (C) EDX mapping of white box area in panel B. (D) EDX spectrum of white box area in panel B.*

3.4 Process of ReEF Combustion and Sulfation

Injection of ReEF particles into the hot zone of the sulfation reactor initiated a series of reactions described in Figure 3.7. Fibers and plastics in ReEF initially heat up to dry, and pyrolyze to generate volatile organic compounds; the volatile matters then mix with oxygen and combust. Finally, the remained char combusts to emit CO and CO_2 with inorganic ashes. As for calcium hydroxide sorbent in ReEF, calcination takes place first. With $Ca(OH)_2$ decomposes, a fresh CaO layer forms. It has been reported that the CaO layer is highly porous and active to react with SO_2. [51], [80] The outer CaO layer undergoes sintering and sulfation simultaneously as the inner $Ca(OH)_2$ continues decomposing. A $CaSO_4$ product layer forms when CaO reacts with O_2 and SO_2. Since the molar density of $CaSO_4$ is larger than that of CaO, the $CaSO_4$ layer is considered to be non-porous, which has strong resistance for SO_2 and O_2 diffusing in and contacting the internal CaO. When the product layer completely covers the interior CaO, the sulfation reaction is subjected to slower solid state diffusion control. In this case, Ca^{2+} and O^{2-} ion transport outward to the surface of product layer to achieve SO_2 capture. [81], [82] Because of extremely slow of solid diffusion, the conversion of sorbent becomes slow and appears to stop at the timescale of the experiment.

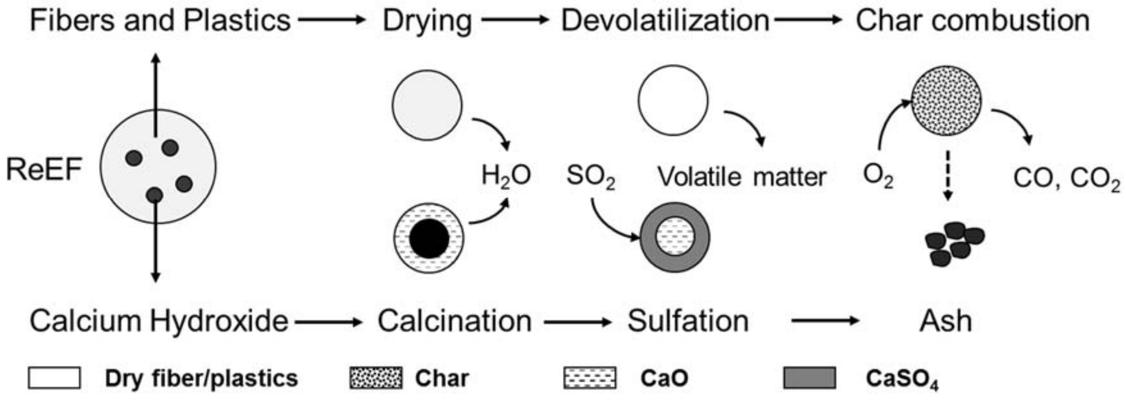

Figure 3.7. Process of ReEF particle combustion and sulfation.

3.5 Sulfation Kinetics of ReEF

Kinetics of ReEF sulfation in Figure 3.7 was characterized by measuring sulfur dioxide concentration with time via FTIR, as shown in Figure 3.8. Before the experiment start, SO_2 concentration within the flow gas remained at 1400 ppm. At time zero, ReEF was dropped into the reactor and calcium hydroxide sorbent began to adsorb and react with SO_2. The concentration of SO_2 decreased to a minimum value immediately before exhausting the calcium hydroxide sorbent and returning asymptotically to its original value of 1400 ppm. The reaction rate of the conversion of calcium hydroxide to calcium sulfate was determined by the change in SO_2 concentration with time and calculated by Equation 3.2,

$$\frac{dX}{dt} = \frac{PV(Y_{SO2,in} - Y_{SO2,out})/RT}{W*a/M(Ca(OH)_2)} \tag{3.2}$$

where X was the molar conversion of calcium hydroxide, P the reactor pressure, V the gas flow rate, Y the concentration of sulfur dioxide, R the gas constant, T the reaction temperature, W the weight of ReEF sample, “a” the weight fraction of sorbent in the ReEF (usually between 0.3-0.43) , and M the molecular weight of calcium hydroxide. Integration the resulting values of dX/dt (Equation 14) provided the conversion of calcium sorbent as a function of time, X(t).

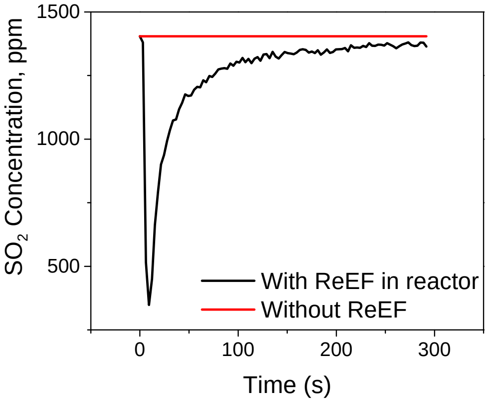

Figure 3.8. Sulfur dioxide concentration profile for ReEF sulfation at 800 °C. *Injection of 25-53 µm ReEF particles into the sulfation reactor at 800 °C with flowing SO_2 (1400 ppm, 5% O_2 in nitrogen) produces a transient reduction in SO_2 during ReEF sulfation.*

ReEF sulfation kinetics was measured at three temperatures (800 °C, 900 °C and 1000 °C) with varying oxygen concentration (5%, 10%, 20% and 30% in nitrogen). Both ReEF samples (10 mg) of different particle sizes and pure calcium hydroxide were injected into the reactor in separate experimental trials, while maintaining the same quantity of total calcium hydroxide in each trial. Figure 3.9 shows the conversion of calcium hydroxide to calcium sulfate as the function of time when using 25-53 μm ReEF particles at 900 °C. Conversion of both reactants (ReEF and pure calcium hydroxide) was similar in the first 50 seconds, while statistically different behavior was observed thereafter. At lower oxygen concentration (Figure 3.9A), the difference of sorbent conversion in pure calcium hydroxide and ReEF was negligible. However, as oxygen concentration increased (Figures 3.9B, C, and D), higher sorbent conversion was observed in pure calcium hydroxide samples.

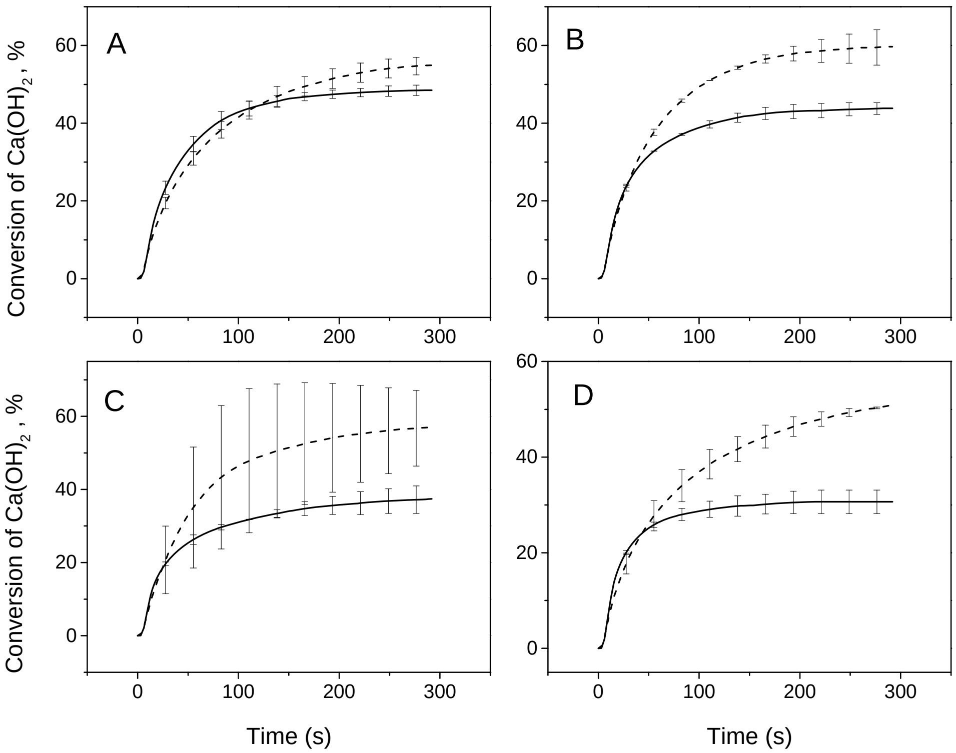

Figure 3.9. Sorbent conversion with reaction time at 900 °C. *Pure calcium hydroxide (dashed line) and sorbent in ReEF (solid line) reacting in: (A) 5%* O_2*, (B) 10%* O_2*, (C) 20%* O_2*, and (D) 30%* O_2*.*

Reduced sorbent conversion in ReEF compared with pure calcium hydroxide is potentially due to an enhanced rate of sintering. Since same mass of calcium hydroxide was used in all experimental trials, the combustion of fibers/plastics in ReEF provided the difference. ReEF Combustion produces carbon dioxide and water; both gases have been shown to accelerate sintering of calcium oxide, [51] which would result in lower sorbent conversion in a higher oxygen environment. Besides, combustion of fibers and plastics generates additional heat that can increase the temperature and enhance sintering, thereby lowering sorbent conversion within ReEF.

Extent of sorbent conversion within ReEF was found to depend on oxygen concentration and particle size; only a weak dependence on reaction temperature was observed. Figure 3.10 depicts the conversion of calcium hydroxide in ReEF to calcium sulfate after 5 minutes by varying the oxygen concentration between 5, 10, 20, or 30% in nitrogen with 1400 ppm SO_2. For small ReEF particles in Figure 3.10A and B (25-53 μm and 53-212 μm), increasing oxygen concentration decreased calcium hydroxide conversion from about 60% to 30%. However, in larger particles depicted in Figure 3.10C (212-500 μm), no discernible difference was observed in sorbent conversion within experimental error, similar to pure calcium hydroxide samples in Figure 3.10D. The effect of temperature on sorbent conversion in ReEF was different from that of pure calcium hydroxide. In ReEF particles, sorbent conversion was always lowest at 900 °C; pure calcium hydroxide exhibited no clear pattern in conversion with respect to temperature.

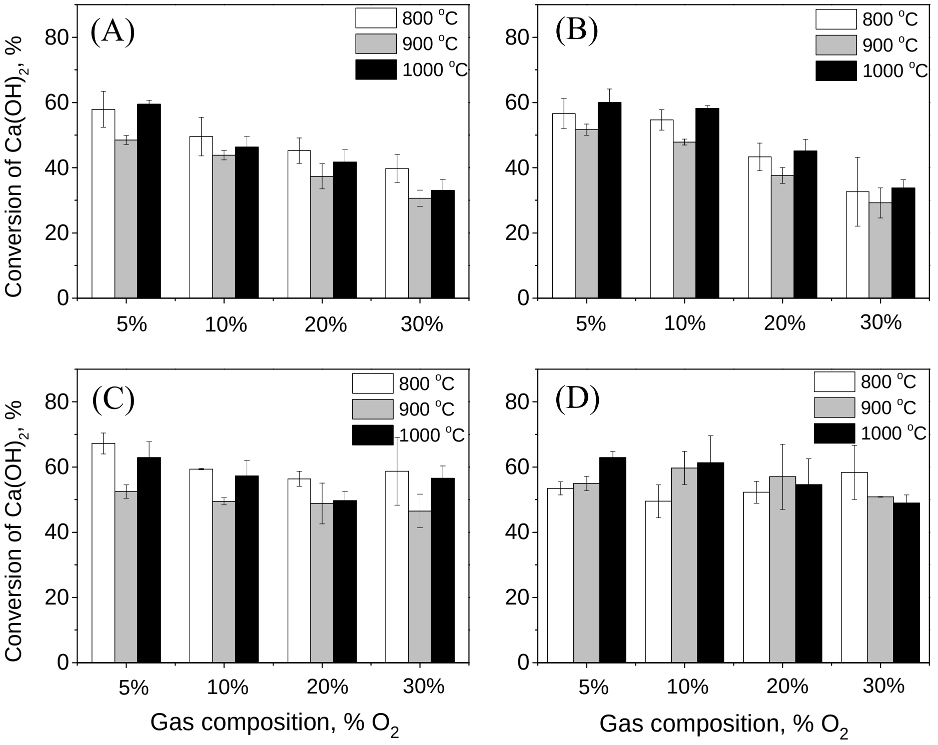

Figure 3.10. Conversion of calcium hydroxide in ReEF. *ReEF containing calcium hydroxide sorbent reacted at 800, 900 and 1000 °C with variable oxygen gas (5%, 10%, 20%, or 30% in nitrogen). Conversion is reported after five minutes for ground ReEF sieved to: (A) 25-53 µm, (B) 53-212 µm, (C) 212-500 µm, and pure calcium hydroxide (D).*

Figure 3.11 presents the normalized reaction rate of sulfation for pure calcium hydroxide (dashed black line) and calcium hydroxide in ReEF (solid red line). A time delay was observed between the maximum reaction rates of pure calcium hydroxide and ReEF. For pure calcium hydroxide, the time of maximum sulfation rate always happened earlier than that of ReEF, which indicates that the combustion of fibers and plastics in ReEF can delay or slow the sorbent sulfation reaction. The time delay (Δt) of the maximum reaction rate in various reaction conditions are listed in Table 3.3. When conducted in lower oxygen concentration, the time delay was found to be as long as six seconds for large particles (212-500 µm).

Table 3.3. Time delay on the maximum reaction rate of sulfation for ReEF.

ReEF particle	25-53 µm			53-212 µm			212-500 µm		
Temperature (°C)	800	900	1000	800	900	1000	800	900	1000
Time delay (s)									
5% O_2	3	3	6	3	3	3	6	5	5
10% O_2	3	3	3	3	3	3	3	3	3
20% O_2	3	3	3	3	3	3	3	3	5
30% O_2	3	3	3	3	3	2	0	0	3

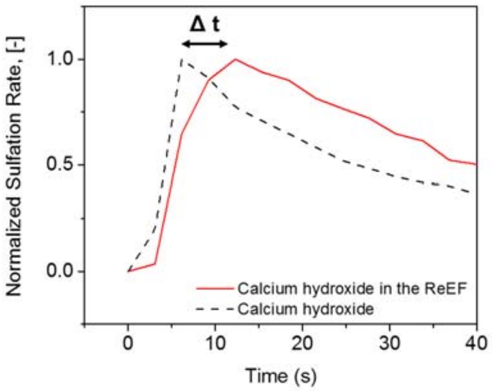

Figure 3.11. Normalized sulfation reaction rate of calcium hydroxide and ReEF. *ReEF particles and pure calcium hydroxide exposed to flowing gas containing 1400 ppm SO_2 at 800 °C exhibits an initial increase in reaction rate followed by a slow decrease as the sorbent saturates with sulfur dioxide. Maximum reaction rate of sorbent sulfation in ReEF is delayed by several seconds relative to that of pure calcium hydroxide sorbent.*

A possible explanation for time delay in ReEF desulfurization is the formation of a film or cloud of gaseous volatile organic compounds around the ReEF particle (generated by combustion of plastics/fibers) which prevent sulfur dioxide from initially contacting the sorbent. Eventually, combustion of plastics and fibers slows down and volatile matters reduce, thus allowing sulfur dioxide to penetrate the remaining sorbent/char matrix and undergo the sulfation reaction. This delay in sulfation provides a tunable design parameter in ReEF preparation of value when co-firing with coal. By designing ReEF with a built-in time delay for sorbent exposure to sulfur dioxide, the sulfation reaction will happen later after sorbents travel upward into the lower temperature zone of the reactor where sulfation is more thermodynamically favorable.

3.6 Calcination of ReEF

As we mentioned above, when a ReEF particle drops into the flue gas, the combustion of fiber/plastics, the calcination of sorbent, and the sulfation reaction happens simultaneously. To further evaluate the effects of fiber/plastics combustion on sorbent calcination and sulfation, ReEF calcination was studied independently. The calcination reactor of Figure 3.3 was utilized for simultaneously combusting and calcining ReEF for defined increments of time. The sample was inserted into the hot zone of reactor in the presence of oxygen flow; fiber and plastics combusted while the sorbent thermally decomposed at high temperature. The calcined ReEF was then subjected to sulfation reaction to evaluate their capability for desulfurization.

Calcination of sorbent in ReEF was found to require longer time than pure calcium hydroxide. 10 mg ReEF and pure calcium hydroxide was inserted into the calcination reactor at 800 °C separately. The gas flow was set at 2 L/min with an oxygen concentration of 21% in nitrogen to simulate air. At these conditions, calcination was measured as a function of time. Samples at each time period were analyzed by XRD and SEM to characterize their physical and chemical structures. Figure 3.12 presents the XRD patterns of combusted/calcined ReEF at 60 (spectrum C) and 120 seconds (spectrum D). For comparison, the XRD spectra of calcined pure calcium hydroxide are shown in Figure 3.12 at 30 and 60 seconds (spectra A and B, respectively). After 30 seconds of calcining pure calcium hydroxide, characteristic peaks of calcium hydroxide were still observed (labeled

"2" in Figure 3.12). However, all calcium hydroxide has disappeared by 60 seconds (Figure 12B), with complete conversion to CaO. While, when ReEF was subjected to the same conditions (60 seconds), the peaks from calcium hydroxide were still observed in the calcined ReEF as shown in Figure 3.12C. Calcium hydroxide within ReEF was not fully converted to CaO until 120 seconds as indicated in Figure 3.12D.

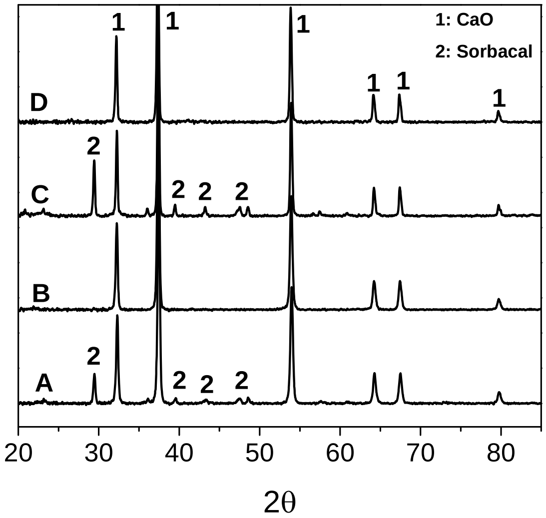

Figure 3.12. X-Ray Diffraction (XRD) pattens of calcined sorbents. *Sorbents exposed to 21% O_2 in nitrogen at 800 °C included: (A) calcium hydroxide for 30 seconds, (B) calcium hydroxide for 60 seconds, (C) ReEF for 60 seconds, and (D) ReEF for 120 seconds.*

3.7 Oxygen Concentration on ReEF Calcination and Sulfation

The concentration of oxygen was also varied in calcination experiments to evaluate its effects on ReEF calcination. Surface morphology of calcined sorbents was characterized by SEM. Figure 3.13 shows the surface of ReEF after 2 min calcination in 21% and 100% oxygen, respectively. At lower oxygen concentration of 21% O_2 in nitrogen (Figure 3.13A), neck formation was observed between small grains, indicative of sintering during calcination. However, in the Figure 3.13A, pores are still observed on the surface. The extent of sintering was not as severe as in pure oxygen, in which the surface consists almost entirely of fused sorbent grains. In the Figure 3.13B, the pores are diminished and a solid continuous surface is observed. From nitrogen adsorption, the porosity of the calcined ReEF in 21% oxygen was 8.4%, while porosity was 3.6% when calcined in pure oxygen. Thus, oxygen content has a strong effect on sorbent sintering.

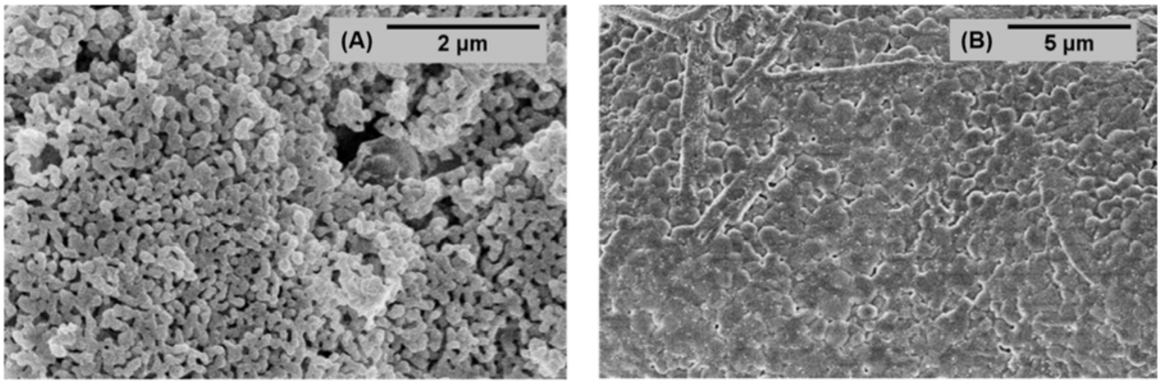

Figure 3.13. SEM micrographs of calcined ReEF. *Images depict: (A) ReEF calcined at 800 °C for 120 seconds in 21%* O_2 *in nitrogen, and (B) ReEF calcined at 800 °C for 120 seconds in 100%* O_2*.*

Calcined ReEF prepared through exposure to different oxygen concentrations were then tested for their ability to desulfurize the flowing SO_2. Figure 3.14 depicts the desulfurization extent of calcium sorbent in ReEF pre-calcined in 21% O_2 (panel A) and 100% O_2 (panel B). For ReEF calcined in lower oxygen environment, the conversion of sorbent was observed to increase continuously over a five-minute experimental trial. In this case, SO_2 can still diffuse through the existing pores into the inner surfaces to continuously react with CaO; longer time will be required before complete pore closure resulting from the formation of $CaSO_4$ layer. Thus, a gradual increase in sorbent conversion was observed. However, for ReEF calcined in high oxygen concentration (100% O_2), the conversion of sorbent achieved an asymptotic value after only two minutes; this behavior was readily apparent for the experiment at 800 °C (Figure 3.14B). Due to the severely sintered particles,

SO_2 reacted only on the sorbent surface. The product $CaSO_4$ layer rapidly covered the surface which generated strong transport resistance for SO_2 penetrating inside to react with CaO.

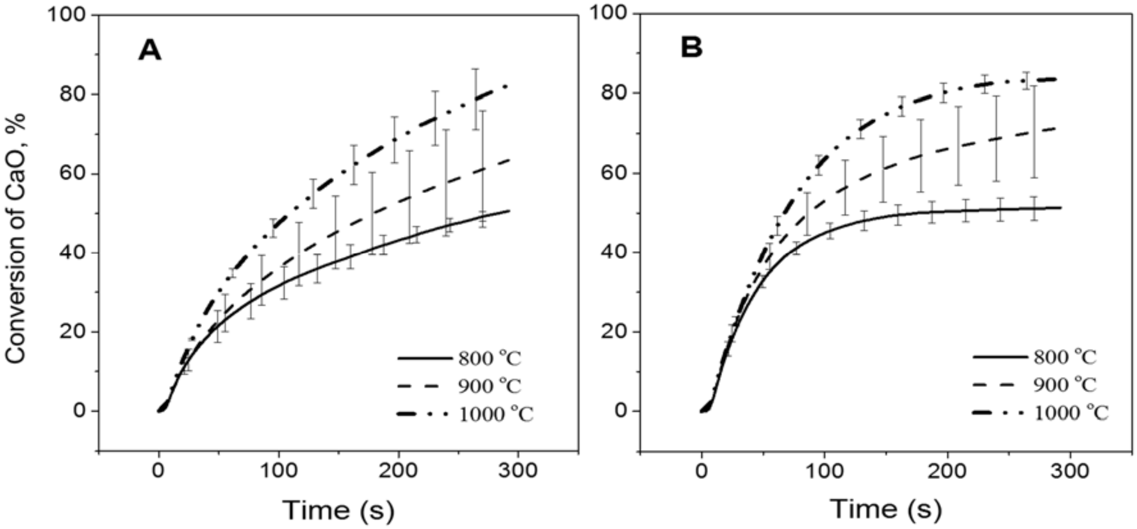

Figure 3.14. Sulfation behavior of calcined ReEF. *(A) ReEF calcined at 800 °C, 120 seconds, 21%* O_2 *in nitrogen. (B) ReEF calcined at 800 °C, 120 seconds, 100%* O_2*.*

3.8 Conclusion

Refuse-derived fuel (RDF) integrated with calcium sorbent named ReEngineered Feedstock^{TM} was evaluated for its capability to desulfurize coal combustion emissions. ReEF contained about 35 wt% of high surface area calcium hydroxide and 65 wt% of non-recyclable fibers and plastics. The compositions of calcium sorbent and RDF varied slightly with different particle sizes of pulverized ReEF. SEM-EDX of ReEF surface indicated that calcium sorbent was evenly dispersed on the surface of RDF in addition to other impurities from wastes. The desulfurization performance of ReEF was evaluated in a drop tube sulfation reactor. Combusting ReEF in a low-oxygen environment led to a high sorbent sulfur uptake at long times (>5 min). Comparing sulfation performance between ReEF and pure calcium hydroxide, the sulfation of ReEF was delayed by the presence of fibers and plastics combustion, which were thought to slow SO_2 diffusion to the sorbent surface. In addition, the combustion of ReEF can enhance the sintering of sorbents, which leads to a sintered non-porous material with lower capability for sulfur uptake.

Chapter 4. Alkaline Earth Metal Catalyzed Thin-film Pyrolysis of Cellulose

4.1. Introduction

The need for renewable feedstocks and sustainable energy to address climate change remains one of the major challenges in the 21st century. Lignocellulosic biomass is a clean, renewable energy source that can be converted to transportation fuels and commodity chemicals via thermochemical pyrolysis. In 2010, worldwide biofuel production reached 28 billion gallons, which is an increase of 17% from 2009, and biofuels provided 2.7% of the world's fuels for automotive/truck transportation, a contribution largely comprised of ethanol and biodiesel. [83] The International Energy Agency has a goal for biofuels to meet more than a quarter of world demand for transportation fuels by 2050 to reduce dependence on petroleum and coal. [84] Fast pyrolysis of solid biomass offers a fast, low-cost technology to meet these goals. [10], [11], [85]

Lignocellulosic biomass is comprised of a porous, cellular microstructure of which cell walls consist primarily of three components: cellulose, hemicellulose, and lignin. [86] During biomass pyrolysis, biomass is heated to high temperatures (400-600 °C) in the absence of oxygen producing a short-lived intermediate liquid phase, which ultimately breaks down to form organic volatiles and permanent gases. [87] In addition, spontaneous ejection of aerosols has been observed via high speed photography. [12] In an effort to simplify the reacting system, prior work has focused on cellulose since it is the most abundant component in woody biomass with a well-defined structure. [88]

Catalysts that alter the reaction rate and distribution of bio-oil mixtures via pyrolysis have recently been categorized as either natural, primary, or secondary depending on the specific reactions upon which they act. [89] While secondary catalysts upgrade pyrolysis vapors outside the particle, primary and natural catalysts can catalyze reactions of the biopolymer and/or the volatile organic compounds within the biomass melt phase. For example, impregnation of supported noble metals has recently shown that organic products such as the furan class of chemicals can be tuned to minimize the formation of aldehyde functional groups. [90] Biomass contains inorganic impurities (e.g. alkali and alkaline metallic species) which can act as natural catalysts, having a dramatic effect on the yield and product distribution of bio-oil. [91]–[93] Understanding the molecular-level role of these natural catalysts is important to optimize the biofuel production processes.

4.1.1 Natural Inorganic Catalysts

Inorganic species within biomass range from less than 1% up to 15% of the total mass, depending on the biomass species and the content of the originating soil. [94] Inorganic ions such as potassium, calcium, and magnesium are the most abundant in biomass/lignocellulosic feedstocks. [95] At the operating temperatures of fast pyrolysis (400-600 °C), inorganic metals are retained within the char, indicating that they likely interacted with the biomass to catalyze biopolymer degradation. [96], [97] Müller-Hagedorn et al. [98] studied the catalytic effect of both sodium and potassium chloride and showed that these metals lowered the decomposition onset temperature of biomass and decreased the production of levoglucosan (LGA). Liu et al. [99] investigated the catalysis of three potassium inorganic salts on cellulose pyrolysis using TGA–FTIR and found that the presence of potassium salts lowered the activation energy and increased the reaction rate of pyrolysis. Kawamoto et al. [100] reported that magnesium and calcium chlorides promoted char formation and suppressed the formation of levoglucosan under N_2 at 400 °C. Khelfa et al. [101] concluded that $MgCl_2$ promotes dehydration at low temperatures as observed both by TGA and pyrolysis analyzed by mass spectrometry. Patwardhan et al. [93] examined varying concentrations of inorganic salts and the following trends were observed in levoglucosan yield in the order of strongest to mildest influence: (a) cations—$K^+ > Na^+ > Ca^{2+} > Mg^{2+}$; (b) anions—$Cl^- > NO_3^- \approx OH^- > CO_3^{2-} \approx PO_4^{3-}$.

4.1.2 Sample Preparation Methods

There are three experimental methods used in the literature to investigate the catalytic effect of inorganic species on the product distribution of bio-oil. Acid washing of biomass with HCl, H_2SO_4, or HNO_3 has been shown to remove naturally present inorganic species allowing for pyrolysis studies in their absence. [102] Raveendran et al. [92] studied the pyrolysis of 12 different biomass feedstocks and observed that the yield of pyrolysis vapors, devolatilization rate, and the initial decomposition temperature increased, while the char yield decreased upon demineralization of the biomass samples. However, significant chemical degradation of biomass can occur during acid demineralization, resulting in a structurally modified biomass that is not representative of the original material. [103]

A second experimental method dopes pure biomass (such as cellulose) with inorganic species via dry mixing or wet impregnation. [102] Shimada et al. [104] impregnated alkali metal and alkaline earth metal chlorides in cellulose, and both significantly changed the low molecular weight product composition even at a low concentrations of catalyst. However, both wet impregnation and dry mixing introduced inorganic species to the biomass as an inorganic salt, such that it is difficult to determine if the observed effects on the degradation of the biomass are caused by the inorganic cations (Ca^{2+}, Mg^{2+}, Na^+, etc…), or the corresponding anions (Cl^-, NO_3^-, OH^-, etc…), or some combination of both. [102]

Ion-exchange is a third method used to prepare samples that simulate the effect of inorganic species chemically bonded to biomass. Dry mixing does not produce bonding between the lignocellulosic material and the added salts, while impregnation is primarily a physical adsorption on the surface of the biomass particles. *Ab initio* modelling of chelated structures formed during ion-exchange (Figure 4.1) indicates that metal ions form one of several interactions with hydroxyl and ether groups in the cellulose structure. [105] Molecular dynamics simulations investigating NaCl interaction with cellulose has shown that the two hydroxyl oxygens (O2, O3) and the hydroxymethyl oxygen (O6) of cellulose are the primary interaction with Na^+. [106] There is also a high affinity of Na^+ to be in a "bridging" position between the O2 and O3 backbone oxygens. [106] Therefore, using the ion-exchange method enables the study of how inorganic species (Ca^{2+} and Mg^{2+}) bonded directly to cellulose affect cellulose pyrolysis.

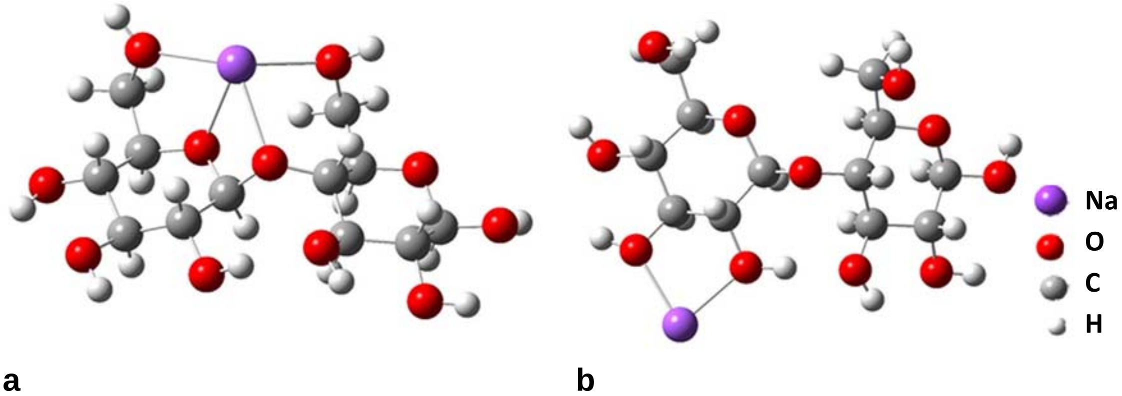

Figure 4.1. Geometry optimized ground state structure of Na$^+$-cellulose. *(a) Na$^+$ near C6-OH group; (b) Na$^+$ near C2-OH group.* [105]

4.1.3 Thin-film Pyrolysis

A major finding of pyrolysis chemistry is that cellulose decomposes through a liquid state before fully converting to a gas. [13], [107] This short-lived intermediate liquid (Figure 4.2) can exist as a molten mixture of depolymerized cellulose, dissolved gases (H_2O, CO, CO_2) and natural catalysts (e.g., Ca^{2+}, Mg^{2+}). [10], [13], [87] The pyrolysis chemistries are competitive with numerous types of transport phenomena including heat transfer through the fluid, mass transfer within the liquid, and external gas-phase mass transfer. Eliminating heat and mass transport effects will be imperative for measuring intrinsic catalytic reactions.

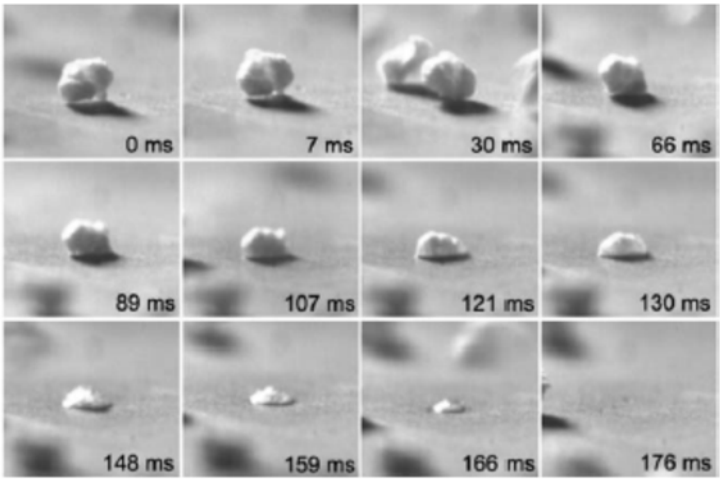

Figure 4.2. Millisecond visualization of cellulose particle decomposition. *Particles of pure cellulose (300 μm) on a high temperature (700 °C)* *Al_2O_3* *surface, observable by high speed photography, rapidly decompose to a liquid intermediate and further boil to vapors.* [87]

In order to achieve isothermal conditions at high temperatures (>400 °C), our group has developed a thin-film deposition technique that produces a micrometer-scale film which allows for extremely high temperature changes (greater than 1000000 °C/min). [14] This temperature increase is much faster than previous pyrolysis techniques, such as powder pyrolysis (1000 °C/min) and thermogravimetric analysis (1−150 °C/min). [108] The criteria for isothermal pyrolysis are defined by comparing pyrolysis reaction kinetics with conductive and convective heat transfer using the dimensionless pyrolysis (Py) and Biot (Bi) numbers. Py^{I} is the ratio of reaction and conduction time scales, Py^{II} is the ratio of reaction and convection time scales, and Bi is the ratio of conduction and convection time scales.

$$\mathrm{Py}^{\mathrm{I}} = \frac{\tau_{\mathrm{reaction}}}{\tau_{\mathrm{conduction}}} = \frac{\lambda}{\rho C_p L^2 k} \tag{4.1}$$

$$\mathrm{Py}^{\mathrm{II}} = \frac{\tau_{\mathrm{reaction}}}{\tau_{\mathrm{convection}}} = \frac{h}{\rho C_p L k} \tag{4.2}$$

$$\mathrm{Bi} = \frac{\tau_{\mathrm{conduction}}}{\tau_{\mathrm{convection}}} = \frac{hL}{\lambda} \tag{4.3}$$

The thermal conductivity, density, and heat capacity of cellulose are represented by λ, ρ, and C_p, respectively. [109] The characteristic length scale is represented with L, the heat transfer coefficient between the biomass sample and the ambient with h, [110], [111] and the reaction rate coefficient for cellulose pyrolysis with k. [112] Plotting the pyrolysis numbers versus the Biot number for different temperatures in Figure 4.3A results in four unique pyrolysis zones: an isothermal and reaction-limited region (where the entire particle is one uniform temperature), a conduction-limited region, a convection-limited region, and a reaction-limited but nonisothermal region (where the particle reaches the reaction temperature quickly but does so with large temperature gradients throughout the particle). [14], [88] Figure 4.3A shows that for fast pyrolysis at 500 °C, the characteristic length scale must be less than 10 μm for isothermal pyrolysis.

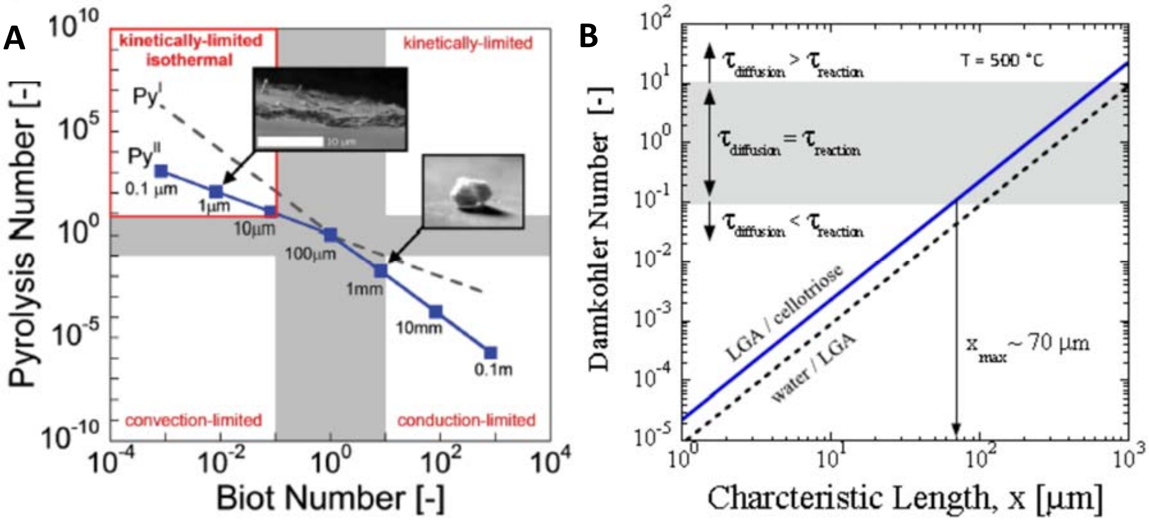

Figure 4.3. Thin-film pyrolysis design. *(A) Reaction-heat transfer map for cellulose pyrolysis, Pyrolysis and Biot Numbers (eqn (1)–(3)) are used to compare heat transfer and reaction time scales. (B) Reaction-mass transfer map, Damkohler number (eqn (4.4)) compares liquid-phase diffusion and reaction timescales as a function of characteristic length scale.* [14]

In addition to rapid heating of biomass samples, thin films also decrease the time scale of product diffusion (<1 ms) through the intermediate liquid by 2 to 4 orders of magnitude relative to powder pyrolysis. The Damkohler Number (Da) is used to compare the ratio of diffusion ($\tau_{diffusion}$) and reaction ($\tau_{reaction}$) timescales:

$$\mathrm{Da} = \frac{\tau_{\mathrm{diffusion}}}{\tau_{\mathrm{reaction}}} = \frac{\mathrm{L}^2\mathrm{k}}{\mathrm{D_A}} \tag{4.4}$$

L is the characteristic length scale, k is the reaction rate [113] and D_A is the liquid-phase diffusivity calculated using the semi-empirical Wilke-Chang method. [114] We calculated high and low diffusivity estimates using two model binary mixtures including water diffusing through levoglucosan (water/LGA) and levoglucosan diffusing through cellotriose (LGA/cellotriose). Reaction and liquid-phase diffusion timescales are calculated as a function of characteristic length. [14] Figure 4.3B shows that for fast pyrolysis at 500 °C, the diffusion rate is about equal to the pyrolysis reaction rate for samples with characteristic length scales greater than or equal 70 μm. This calculation indicates that for the thin-films (3-10 μm in thickness), liquid-phase diffusion is much faster than pyrolysis reactions.

Figure 4.3 uses dimensionless numbers to estimate the isothermal pyrolysis length scale limit as 10μm. In addition to this analysis, we have calculated transient temperature profiles in our thin-film as to determine the rate and uniformity by which biomass samples are heated. MATLAB was used to solve the following transient, one dimensional heat transport equation:

$$\frac{\partial \mathrm{T}}{\partial \mathrm{x}} = \frac{\lambda}{\rho \mathrm{C_p}}\left(\frac{\partial^2 \mathrm{T}}{\partial \mathrm{x}^2}\right) + \frac{\mathrm{R}\Delta \mathrm{H_{rxn}}}{\mathrm{C_p}\rho} \tag{4.5}$$

with boundary conditions,

$$\frac{\partial \mathrm{T}}{\partial \mathrm{x}}(\mathrm{x} = 0, \mathrm{t}) = \frac{\mathrm{h_s}(\mathrm{T} - \mathrm{T_s})}{\lambda} \tag{4.6}$$

$$\frac{\partial T}{\partial x}(x = L, t) = \frac{h_a(T - T_a)}{\lambda} \tag{4.7}$$

$$T(x, t = 0) = 25\ ^{\circ}C \tag{4.8}$$

The values used in the model for cellulose physical properties (λ, C_p, ΔH_{rxn} and ρ; taken from [109]), reaction rates (R; calculated from [113]) and the solid-solid heat transfer coefficient (h_s; intermediate value of 2000 W/m^2K based on previous work [87], [111]) are the same as those mentioned in the main body of the chapter. The heat transfer coefficient between the thin-film and the ambient gas-phase (h_a) was assumed to be 20 W/m^2K. The characteristic length (L) is the cellulose thin-film thickness (i.e., 3 μm) which is determined from scanning electron microscopy (SEM). Using these parameters, thermal profiles for the cellulose thin-film were calculated.

Figure 4.4 shows the temperature as a function of position within the cellulose thin-film at several times. These profiles indicate that axial (i.e., along x-coordinate or thin-film thickness) temperature gradients within the thin-film are minor (< 3 °C) and that the cellulose sample is heated from ambient to reaction temperature in a few milliseconds, producing a temperature ramp greater than 1,000,000 °C/min. This heat transfer time scale is 1-2 orders of magnitude faster than the time it takes for cellulose particles to volatilize in ablative pyrolysis reactors. [87] These simulations, coupled with the dimensionless analysis presented in the main paper, suggest that cellulose thin-films are heated isothermally and faster than pyrolysis reactions.

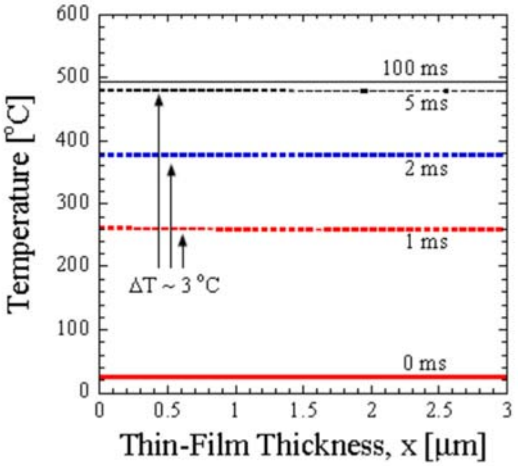

Figure 4.4. Transient temperature profiles for cellulose thin-film pyrolysis at 500 °C. *One dimensional MATLAB simulations indicate that the cellulose thin-film is heated up to reaction temperature in approximately 5 milliseconds. In these calculations, an intermediate solid-to-solid heat transfer coefficient is assumed (2000 W/m^2K).* [87], [111] *Cellulose physical properties are taken from previous work,* [109] *and the thin-film thickness is assumed to be 3 µm as determined via SEM imaging.*

A second issue regarding the role and form of natural catalysts is the question of whether they catalyze the pyrolysis of the original polymer (i.e. primary reactions) and/or the reaction of product organic compounds within the melt-phase prior to evaporation (i.e. secondary reactions). It was previously shown that pyrolysis can be conducted under conditions called ‘thin-film pyrolysis’ which have negligible secondary reactions (reactions that occur under diffusion-limited conditions within the melt-phase). [88], [115] Alternatively, preparation of thicker biomass samples allows for evaluation of the extent of melt-phase reactions of volatile products; for example, levoglucosan was shown using ^{13}C and ^{2}H isotopic labeling to undergo secondary reactions to pyrans and light oxygenates. [116] However, while the catalytic role of alkaline earth metals has been demonstrated, it is not known whether these catalysts primarily operate on either primary or secondary reactions of cellulose.

4.2 Experimental Description

In this study, cellulose was doped with calcium and magnesium ions and the corresponding oxides at different concentrations. Prepared samples were pyrolyzed at two different length scales (thin-film and powder) using the Frontier micropyrolyzer coupled with GC/MS. Additionally, the influence of alkaline earth metal on cellulose secondary reaction was investigated by impregnating levoglucosan with the nitrate salts.

4.2.1 Ca and Mg doping methods

Calcium nitrate and magnesium nitrate were selected for study due to their function in plant biology [95], [117] as well as their low decomposition temperatures of 500 °C and 330 °C, respectively. [118] Metal ion concentrations of 0.0125, 0.025, 0.05, 0.125, 0.25, and 0.5 mmol/g cellulose were selected to simulate those present in lignocellulosic biomass. [93], [94], [98], [119], [120] To produce an ion-exchanged sample, a known amount of nitrate salt ($Ca(NO_3)_2{\bullet}4H_2O$, purchased from Acros, ACS grade with > 99% purity, or $Mg(NO_3)_2{\bullet}6H_2O$, purchased from Alfa Aesar, 99.999%) was dissolved in 20 mL of deionized water. One gram of microcrystalline cellulose (obtained from Alfa Aesar; Part Number: A17730) was immersed in the nitrate salt solution, and stirred at room temperature for two hours. Cellulose was then filtered and dried in an oven at 70 °C overnight to obtain the ion-exchanged sample. Ion-exchanged cellulose was prepared without rinsing the sample with deionized water. Dry mixed samples were prepared by mixing solid oxides (CaO, purchased from Sigma, 95%; MgO, purchased from Alfa Aesar, 99.95%) with one gram of cellulose. Because levoglucosan is soluble in water, filtration does not allow of separation in the manner of ion-exchange preparation. Therefore, levoglucosan samples were prepared via the incipient wetness impregnation method, where 100 mg of levoglucosan (LGA, purchased from Sigma, 99%) was added to a 2.5 mL nitrate salt solution and dried in an oven at 90 °C overnight.

4.2.2 Thin-film and powder sample preparation

'Powder' samples refer to preparation of cellulose with characteristic length scales on the order of one millimeter to allow for diffusion limitations, which leads to secondary reactions within the intermediate melt phase at pyrolysis temperatures. [88], [115] Powder samples were prepared by depositing approximately 1.5 milligrams of dry mixed cellulose samples, ion-exchanged cellulose samples, or impregnated LGA samples directly into a pyrolysis crucible using a five point balance. [88], [115], [116] Thin-film samples were prepared to be one-to-ten microns thick such that the samples can react at temperatures as high as 500 °C without heat or mass transfer limitations. Thin films were prepared by first suspending microcrystalline cellulose or dissolving LGA powder in water. Then, 25 μL of the suspension (1.0 wt% cellulose or LGA) was transferred to a 4 mm × 8 mm (diameter × height) cylindrical pyrolysis crucible. The water was removed by evaporation at room temperature under a vacuum (25 in Hg), leaving behind a micrometer-scale film of cellulose or LGA on the inner wall of the crucible. Based on previous work, the thin-film length scale is on the order of three microns while the powder length scale is around 780 microns [88] as depicted in Figure 4.5A and F.

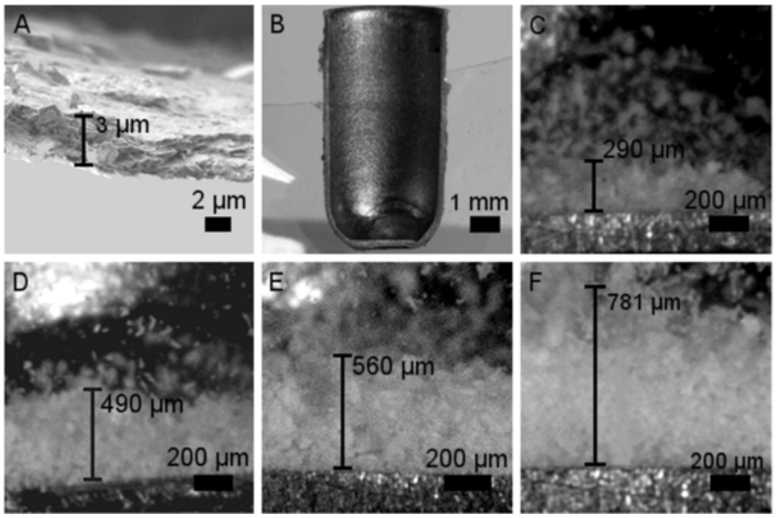

Figure 4.5. Sample loading dimensions. *(A) SEM image of a 250 μg cellulose thin-film. (B) Empty pyrolysis crucible. (C) Photograph of a 240 μg sample loading. (D) Photograph of a 460 μg sample loading. (E) Photograph of a 1020 μg sample loading. (F) Photograph of a 1540 μg sample loading.* [88]

4.2.3 Analytical methods for ion-exchanged sample

For ion-exchanged samples, calcium and magnesium ions doped in cellulose were quantified by inductively coupled plasma optical emission spectrometry (ICP-OES, PerkinElmer Inc. Optima 4300 DV) analysis via an acid digestion procedure (ASTM D5198–92). [121] One gram of ion-exchanged cellulose was dissolved in 10 mL of 34.5 wt% ACS reagent grade nitric acid (purchased from Acros Organics, > 99.9995% pure by metal basis; 69% pure by weight) in a flask. This suspension was covered and heated at 95 °C for two hours with constant stirring. Then the solution was cooled to room temperature, and 5.0 mL of concentrated nitric acid (69 wt%) was added in the solution and stirred for another 30 min. After acid digestion was complete, 50 mL of Milli-Q water was added to the flask, and the contents filtered into a 250 mL volumetric flask. The solution was diluted to 250 mL and analyzed using ICP-OES. Residual anion characterization was determined by Galbraith Laboratories Inc. using ion chromatography (IC).

Interactions of alkaline earth metal ions (Ca^{2+}, Mg^{2+}) with cellulose for ion-exchanged samples have been investigated by laser Raman spectroscopy (WITec alpha300 R confocal Raman microscope with UHTS300 spectrometer and DV401 CCD detector). Raman spectra were excited with the 514.5 nm line of an argon laser, using approximately 50 mW of radiant power at the sample. The single spectrum was collected on a 10 seconds integration time and triple accumulations.

4.2.4 Pyrolysis methods and product identification

Thin-film and powder pyrolysis was performed with a single shot Frontier 2020 micropyrolyzer, directly connected to an Agilent 7890A gas chromatograph (GC) coupled with 5975C mass spectrometer (MS), in which the GC was installed with a thermal conductivity detector (TCD) and a flame ionization detector (FID). [88], [115], [116], [122] The volatile and gaseous products were separated using multidimensional chromatography with cryogenic temperatures, while char was quantified via post-reaction burnoff by injecting oxygen into the pyrolysis furnace. [88], [116] Products were identified by comparing retention times of analytes to those of pure standards using GC/MS. All pyrolysis experiments were performed in triplicate. 28 organic compounds were identified and quantified similar to the method reported previously. [88] Product yields were reported as averages with a 90% confidence interval to illustrate experimental error, and these compounds contributed to 71% to 103% of the carbon balance (based upon the moles of carbon in the initial cellulose sample). Typically, the standard deviation for individual thin-film and powder pyrolysis products was 1−10% of the yield.

In this study, varying concentrations of calcium and magnesium were doped in cellulose and levoglucosan (LGA) for evaluation at powder and thin-film pyrolysis conditions. The pyrolysis products obtained in the presence of metal ions were the same as those from pure cellulose pyrolysis, but the yields of each species were different, indicative of the promoted pathways of calcium and magnesium catalysts.

4.3 Characterization of Ca-loaded samples

Table 4.1 shows the amount of calcium and magnesium doped in powder and thin-film samples for different preparation methods. Ca^{2+}/cellulose and Mg^{2+}/cellulose samples were prepared by ion-exchange using increasing $Ca(NO_3)_2$ and $Mg(NO_3)_2$ concentrations; calcium and magnesium concentrations in cellulose were determined by ICP-OES and were in the desired concentration range (0.01-0.5 mmol/g cellulose). For dry mixed samples, calcium oxide and magnesium oxide loadings were selected such that the metal concentrations were the same as the ion-exchanged samples with additional oxide loadings increased by tenfold; nominal concentrations were 0.125, 0.25, 0.5, 1.25, 2.5, and 5 mmol/g cellulose. Actual calcium and magnesium content in dry mixed samples are listed in Table 4.1. For impregnated samples, calcium and magnesium present in powder and thin-film pyrolysis were calculated based on the amount of nitrate salts added during preparation. Thus, metal loading concentrations of all methods of sample preparation were nearly identical.

Table 4.1. Metal content of cellulose and levoglucosan samples.[a]

Sample Preparation Method	Ca^{2+} [mmol/g cellulose]	Mg^{2+} [mmmol/g cellulose]
Dry mixing	0.127	0.125
	0.256	0.257
	0.501	0.496
	1.252	1.260
	2.518	2.488
	5.014	4.999
Ion-exchange[b]	0.017	0.011
	0.028	0.033
	0.056	0.063
	0.115	0.106
	0.320	0.283
	0.460	0.692
Impregnation	0.014	0.013
	0.026	0.025
	0.051	0.050
	0.128	0.127
	0.251	0.252
	0.503	0.501

[a] Prepared samples were used in both powder and thin-film experiments.
[b] Powder and thin-film samples prepared by ion-exchange were characterized using ICP-OES, while all other sample concentrations were determined by calculation.

Table 4.2 lists the nitrate concentration quantified by ion chromatography (IC) analysis of selected ion-exchanged samples both for Ca^{2+}/cellulose and Mg^{2+}/cellulose samples. As expected, there was no detectable nitrate (0.000 mmol/g cellulose, Table 4.2) in pure cellulose. However, when using the ion-exchange preparation method, there was some unavoidable nitrate residue remaining in the sample. Based on metal cation concentrations listed in the second column of Table 4.2 and the chemical formula of nitrate salts, the nitrate content could be as much as 1.0 mmol/g cellulose. However, for both Ca^{2+}/cellulose and Mg^{2+}/cellulose samples, the actual nitrate content was less than 10% of the theoretical maximum, with greater than 90% of nitrates removed in the filtrate. Any effect of using the ion-exchange method on cellulose pyrolysis samples is therefore primarily caused by metal cations (Ca^{2+} and Mg^{2+}) and not nitrate anions (NO_3^-).

Table 4.2. Nitrate content of selected ion-exchanged samples.

Ion-exchanged Sample		Metal Ion[a] [mmol/g cellulose]	Nitrate[b] [mmol/g cellulose]
Pure Cellulose		0.000	0.000
Ca^{2+}	Lowest loading cellulose	0.017	0.003
	Highest loading cellulose	0.460	0.094
	Heat-treated highest loading cellulose[c]	0.460	0.096
Mg^{2+}	Lowest loading cellulose	0.011	0.002
	Highest loading cellulose	0.692	0.103
	Heat-treated highest loading cellulose[c]	0.692	0.067

[a] Calcium and magnesium concentrations were determined by ICP-OES.
[b] Nitrate concentrations were determined by ion chromatography.
[c] Heat treatment was applied to ion-exchanged cellulose sample with the highest metal ion concentration at 150 °C for 3h under nitrogen flow.

Nitrate salts decompose upon heating to release nitrogen dioxide. To evaluate nitrate removal from the ion-exchanged cellulose samples, heat treatment was applied to the highest loading samples of cellulose for both calcium and magnesium at 150 °C for three hours under nitrogen flow. As listed in Table 4.2, the nitrate content of the heat-treated calcium sample (0.094 mmol/g cellulose) was the same as the non-treated calcium sample (0.096 mmol/g cellulose), which indicates that heat treatment does not remove nitrates in calcium-doped ion-exchanged samples. In contrast, the heat-treated sample with magnesium (0.067 mmol/g cellulose) had less nitrate than the non-treated one (0.103 mmol/g cellulose), which is likely due to the lower decomposition temperature (330 °C) of magnesium nitrate. [118]

Figure 4.6 shows the Raman spectra for pure cellulose (green line), 0.5 mmol/g Ca^{2+}/cellulose (blue line), and 0.5 mmol/g Mg^{2+}/cellulose (red line) samples in the interval 0-4200 cm^{-1}. Pure cellulose gives the characteristic band at 1100-1120 cm^{-1} and 2900 cm^{-1}. While for ion-exchange samples no matter doped with calcium or magnesium ions, an increase of intensity was observed at these two bands, which indicates chemical bonding formed between metal ions and the hydroxyl or ether groups in cellulose. Other than enhanced intensity, new band appears at 1050 cm^{-1} proving the existence of calcium and magnesium ions in cellulose. Raman spectra changes between the pure cellulose and ion-exchange samples show that calcium and magnesium ions were successfully doped into cellulose.

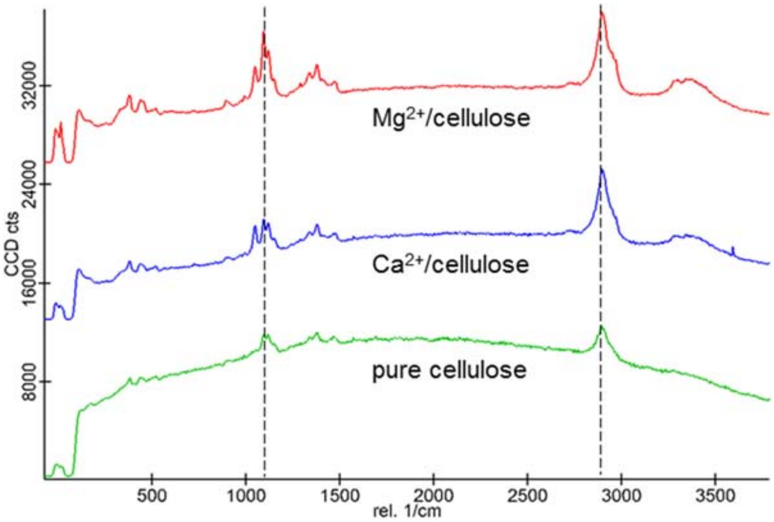

Figure 4.6. Raman spectra of ion-exchanged cellulose samples.

4.4 Effect of CaO and MgO on Cellulose Pyrolysis

The product distribution and yields from cellulose powder pyrolysis at varying metal oxide loadings for both calcium and magnesium are depicted in Figure 4.7. The yield of anhydrosugars, including levoglucosan, 1,6-anhydroglucofuranose (AGF), and dianhydroglucopyranose (DAGP), decreased slightly at high CaO loadings (5 mmol/g cellulose, Figure 4.7A), while adding MgO had no effect (Figure 4.7B). Both CaO and MgO exhibited negligible influence on the yield of pyrans (1,5-anhydro-4-deoxy-D-glycero-hex-i-en-3-ulose (ADGH), 2,3-dihydro-3,5-dihydroxy-6-methyl-4H-pyran-4-one (DHMDHP), and 3,5-dihydroxy-2-methyl-4H-pyran-4-one (DHMP)) or furans (hydroxymethylfurfural, furfural, furan, etc). However, the presence of CaO doubled the yield of light oxygenates (consisting of formaldehyde, glycolaldehyde, methyl glyoxal, etc) from 11% to 24% at a loading of 5.0 mmol/g cellulose. At the same time, permanent gases (CO and CO_2) increased slightly from 2.6% to 5.3% as more CaO was added (Figure 4.7A). In contrast, MgO did not alter the yield of any product class, as shown in Figure 4.7B. Char formation with CaO and MgO was approximately the same (~12%) for all conditions.

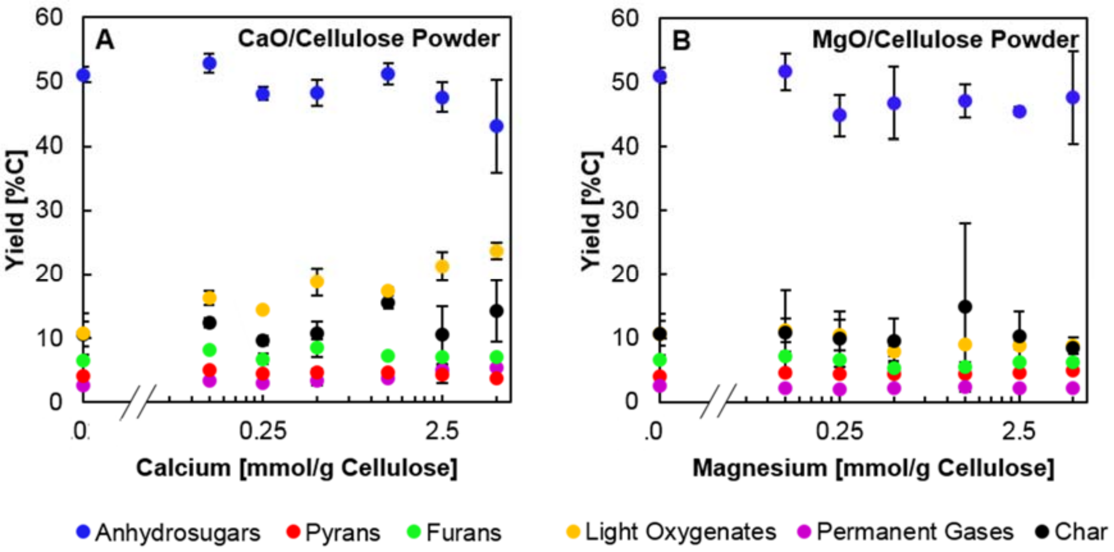

Figure 4.7. Pyrolysis product distribution for CaO/cellulose and MgO/cellulose samples. *Yields of anhydrosugars, pyrans, furans, light oxygenates, permanent gases, and char are shown for (A) CaO/cellulose powder pyrolysis; (B) MgO/cellulose powder pyrolysis. Error bars represent a 90% confidence interval and are not shown if smaller than the width of symbols.*

Figure 4.8 shows the yield of selected light oxygenates from CaO/cellulose and MgO/cellulose powder pyrolysis. Among light oxygenates, formaldehyde and hydroxyacetone (Figure 4.8A and B) increased the most (+8% and +2%, respectively) for CaO/cellulose pyrolysis, which accounts for the majority of the increase in light oxygenates yield. Hydroxyacetone and formaldehyde yields were unaffected by the addition of MgO to cellulose pyrolysis. High loading of calcium oxide had a minor effect on anhydrosugar and light oxygenate yields, while magnesium oxide addition had negligible effect. This suggests that metal oxides found in biomass pyrolysis char [96], [97] do not affect pyrolysis and that any naturally present alkaline earth metals must be present in a non-oxide form to be catalytically active.

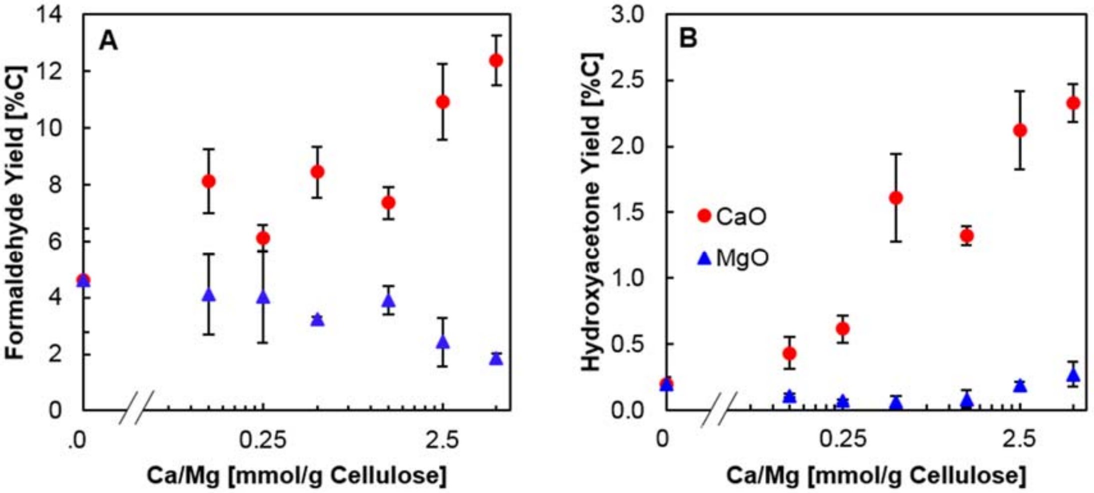

Figure 4.8. Comparison of product yields for CaO/cellulose and MgO/cellulose powder pyrolysis. *CaO/cellulose results (red circles), MgO/cellulose results (blue triangles). Yields of (A) formaldehyde and (B) hydroxyacetone are compared for CaO/cellulose and MgO/cellulose powder experiments as a function of metal ion loading. Error bars represent a 90% confidence interval and are not shown if smaller than the width of symbols.*

4.5 Effect of Ca^{2+} and Mg^{2+} on Cellulose Pyrolysis

To examine the influence of calcium and magnesium on primary and secondary cellulose pyrolysis, thin-film samples were prepared to eliminate secondary chemistry and transport limitations. [88] The product distribution of thin-film pyrolysis was compared to that of powder samples. Figure 4.9 shows the pyrolysis product yields from Ca^{2+}/cellulose powder (Figure 4.9A) and thin-film (Figure 4.9C) samples as well as Mg^{2+}/cellulose pyrolysis at powder and thin-film conditions (Figure 4.9B and D, respectively). Under diffusion-limited conditions (powder pyrolysis), the results in Figure 4.9A indicate that yield of anhydrosugars declined from 51% from pure cellulose to 13% from 0.5 mmol Ca^{2+}/g cellulose. The yield of light oxygenates increased more than twofold from 11% to 29%, and permanent gases rose to 12%. In contrast, the yield of anhydrosugars (Figure 4.9B) only declined to 31% with Mg^{2+}/cellulose powder pyrolysis. Interestingly, doping of magnesium into cellulose did not significantly change the yield of light oxygenates, and only char yield significantly increased from 11% to 25%, compared to only 15% for Ca^{2+}/cellulose powder pyrolysis (Figure 4.9A). Inorganic metal ions have been reported to catalyze cellulose fast pyrolysis, including depolymerization, dehydration, ring opening, and repolymerization reactions. [86], [101] Liu et al. [86] showed that stronger Lewis acids, Mg^{2+} and Ca^{2+}, are more effective than alkali metal ions (Na^+ and K^+) at catalyzing dehydration of sugars, leading to the formation of more cross-linked cellulose and, eventually, char. This is consistent with experimental results; both calcium and magnesium catalyzed char formation in cellulose powder pyrolysis.

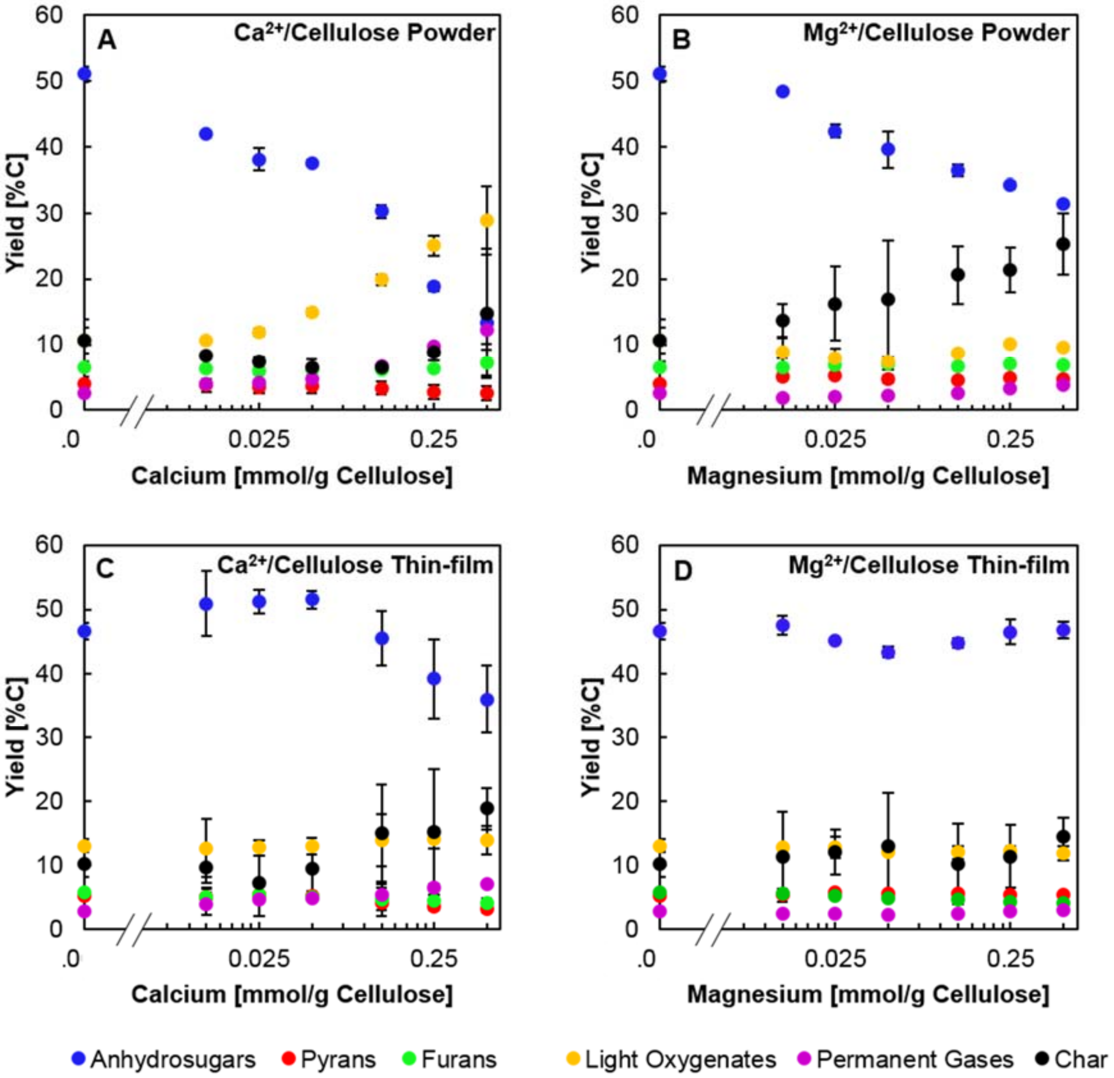

Figure 4.9. Pyrolysis product distributions for Ca^{2+}/cellulose and Mg^{2+}/cellulose powder and thin-film samples. *Yields of anhydrosugars, pyrans, furans, light oxygenates, permanent gases, and char are shown for (A) Ca^{2+}/cellulose powder pyrolysis; (B) Mg^{2+}/cellulose powder pyrolysis; (C) Ca^{2+}/cellulose thin-film pyrolysis; (D) Mg^{2+}/cellulose thin-film pyrolysis. Error bars represent a 90% confidence interval and are not shown if smaller than the width of symbols.*

Calcium and magnesium ions affected pyrolysis product distribution significantly less in thin-film pyrolysis than powder pyrolysis (Figure 4.9C and D). Yield of anhydrosugars for Ca^{2+}/cellulose thin-film was reduced by 11% (Figure 4.9C), which was much less than the 38% observed in powder pyrolysis (Figure 4.9A). The yield of light oxygenates, pyrans, and furans did not change in calcium thin-film pyrolysis. Char yield increased by the same amount in both thin-film and powder reactions, which is indicative of a primary catalytic reaction of cellulose to char. No significant change was observed in the yield of anhydrosugars or any other major product class from Mg^{2+}/cellulose thin-film pyrolysis (Figure 4.9D). Of particular note, char yield did not significantly increase with magnesium addition at thin-film conditions, implying that magnesium ions only affect secondary char formation and not primary.

From the comparison of product distributions for Mg^{2+}/cellulose powder and thin-film pyrolysis, it is clear that magnesium ions primarily catalyze secondary pyrolysis reactions. While the distribution of cellulose pyrolysis products from magnesium-doped samples was unchanged under thin-film conditions, the significant reduction in anhydrosugars yield and increase in char yield from powder pyrolysis indicates that levoglucosan reacted within the cellulose melt phase prior to evaporation. In contrast, calcium catalyzed both the initial cellulose depolymerization reactions to volatile species as well as the secondary melt-phase reactions. Figure 4.8 shows that calcium is more active within molten cellulose than magnesium. This important distinction is apparent in the parity plots of Figure 4.10, which compare the pyrolysis reaction products between pure cellulose and the highest loading of calcium/magnesium for both thin-film (Figure 4.10C and D) and powder (Figure 4.10A and B) conditions. Both parity plots for calcium exhibit significant scatter, indicative of significant change in the product distribution resulting from calcium ion doping. However, the difference between Figure 4.10B and D clearly shows that magnesium has almost no effect on the primary reactions of cellulose while catalyzing secondary reactions within the cellulose melt phase.

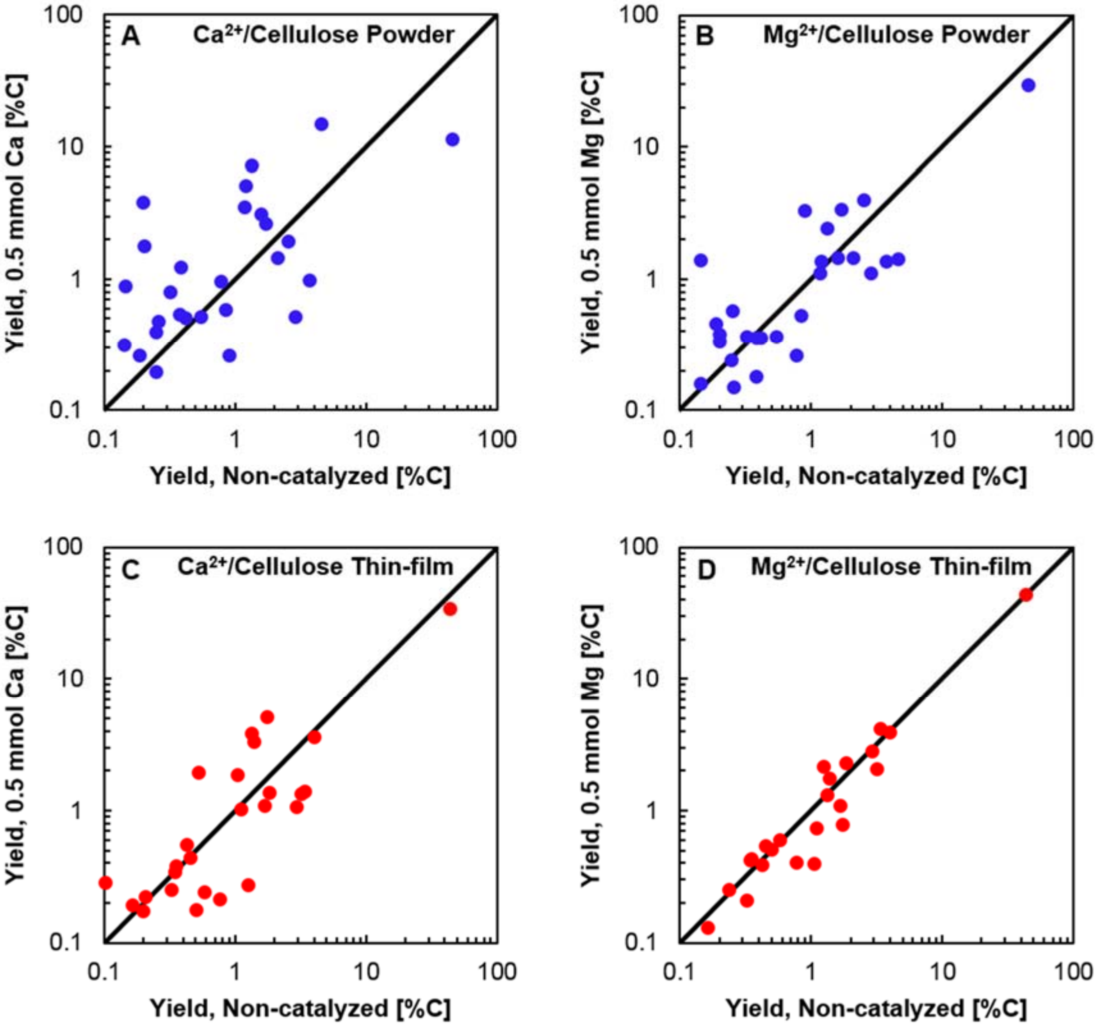

Figure 4.10. Comparison of Ca^{2+}/cellulose and Mg^{2+}/cellulose powder and thin-film samples with pure cellulose pyrolysis. *Yields from pure cellulose are compared with yields from (A) 0.5 mmol/g Ca^{2+}/cellulose powder sample; (B) 0.5 mmol/g Mg^{2+}/cellulose powder sample; (C) 0.5 mmol/g Ca^{2+}/cellulose thin-film sample; and (D) 0.5 mmol/g Mg^{2+}/cellulose thin-film sample.*

Figure 4.11 compares product yields between Ca^{2+}/cellulose and Mg^{2+}/cellulose powder (transport-limited) and thin-film (isothermal) pyrolysis for six selected compounds. As the most abundant anhydrosugar, levoglucosan (LGA) yield dropped significantly from 46% to 11% for the calcium sample and 29% for the magnesium sample in powder pyrolysis (Figure 4.11A). This suggests that calcium and magnesium ions promote LGA breakdown after it was formed via primary transdeglycosylation. [123] Since the yield of light oxygenates increases upon calcium and magnesium ion doping, it is likely that secondary reactions of LGA, catalyzed by these alkaline earth metals, are the cause of the increased light oxygenates yield.

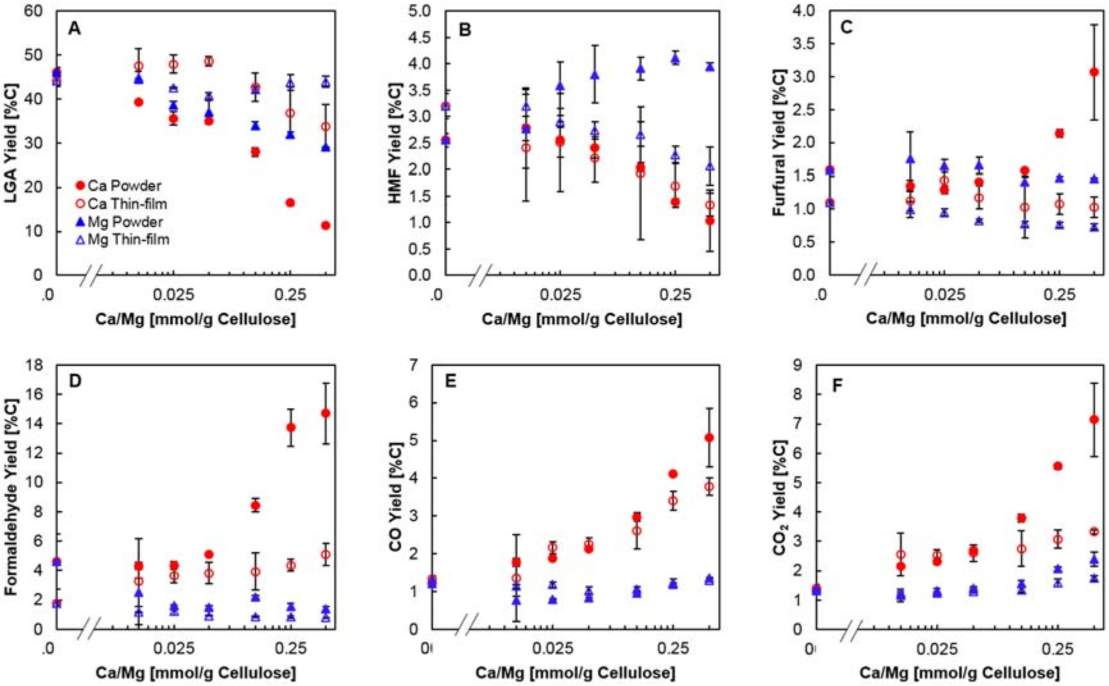

Figure 4.11. Comparison of product yields for Ca^{2+}/cellulose and Mg^{2+}/cellulose powder and thin-film samples. *Ca^{2+}/cellulose powder results (red solid circles), Ca^{2+}/cellulose thin-film results (red hollow circles), Mg^{2+}/cellulose powder results (blue solid triangles), Mg^{2+}/cellulose thin-film results (blue hollow triangles). Yields of (A) LGA, (B) HMF, (C) furfural, (D) formaldehyde, (E) CO, and (F) CO_2 are compared for powder (millimeter scale) and thin-film (micrometer scale) experiments as a function of Ca^{2+} and Mg^{2+} loading amount. Error bars represent a 90% confidence interval and are not shown if smaller than the width of symbols.*

Figure 4.9 indicates that the total yield of furans remained primarily unchanged in the presence of calcium or magnesium ions. However, inspection of individual furan yields reveals that natural catalysts alter single furan production. Among furan species, hydroxymethylfurfural (HMF; the most abundant furan) yield was reduced by 1.5%, while furfural (the second most abundant furan) yield increased by 1.5% (Figure 4.11B and C) during Ca^{2+}/cellulose powder. This suggests functional groups bonded to the furan ring, such as the hydroxymethyl group of HMF, are catalytically cleaved by calcium ions to produce smaller furans such as furfural, and coincides with an increase in C1 products such as formaldehyde (Figure 4.11D), carbon monoxide (Figure 4.11E), and carbon dioxide (Figure 4.11F). The observation that furfural remains constant with variable catalyst loadings under thin-film condition indicates that the natural catalysts likely catalyze the secondary reaction of HMF to form furfural. While calcium ions showed significant activity, the activity of magnesium to catalyze the conversion of HMF to furfural was considerably less.

With regard to permanent gas yields, CO_2 yield was higher than CO yield for every cellulose pyrolysis trial, whether doped with calcium or magnesium ions (Figure 4.11E and 4.11F). Both CO and CO_2 exhibited the same trend of increased yield with increased catalyst concentration. While CO yield was similar for thin-film and powder conditions, the yield of CO_2 from powder experiments was significantly higher than from thin-film experiments, especially at high calcium ion loadings. This indicates that calcium ions promote CO_2 formation via secondary reactions.

4.6 Effect of Ca^{2+} and Mg^{2+} on Levoglucosan Pyrolysis

To further examine the influence of calcium and magnesium ions on secondary reactions, levoglucosan (LGA) was doped with calcium and magnesium ions under thin-film and powder pyrolysis conditions. Based on previous work, LGA does not break down when pyrolyzed alone (in the absence of metal ions or other co-reactants). [116], [124] However, the presence of calcium and magnesium had a strong effect on LGA pyrolysis and dramatically lowered the yield of anhydrosugars in both thin-film and powder experiments (Figure 4.12A-D). A similar trend was observed for all four conditions: (i) levoglucosan yield decreased significantly, (ii) char yield increased to between 8% and 12%, and (iii) light oxygenates and permanent gases were produced from levoglucosan. Calcium ions were more active than magnesium ions, and as expected, the extent of levoglucosan conversion was greater in diffusion-limited powder pyrolysis experiments. Ca^{2+}/LGA powder and thin-film pyrolysis produced more light oxygenates and permanent gases than Mg^{2+}/LGA samples (Figure 4.12A vs. B and Figure 4.12C vs. D). LGA thin-film pyrolysis produced negligible amounts of pyrans and furans regardless of calcium or magnesium concentrations, while small amounts were produced during powder pyrolysis. The decrease in LGA yield, as well as the formation of secondary products, demonstrates that calcium and magnesium ions catalyze secondary levoglucosan reactions.

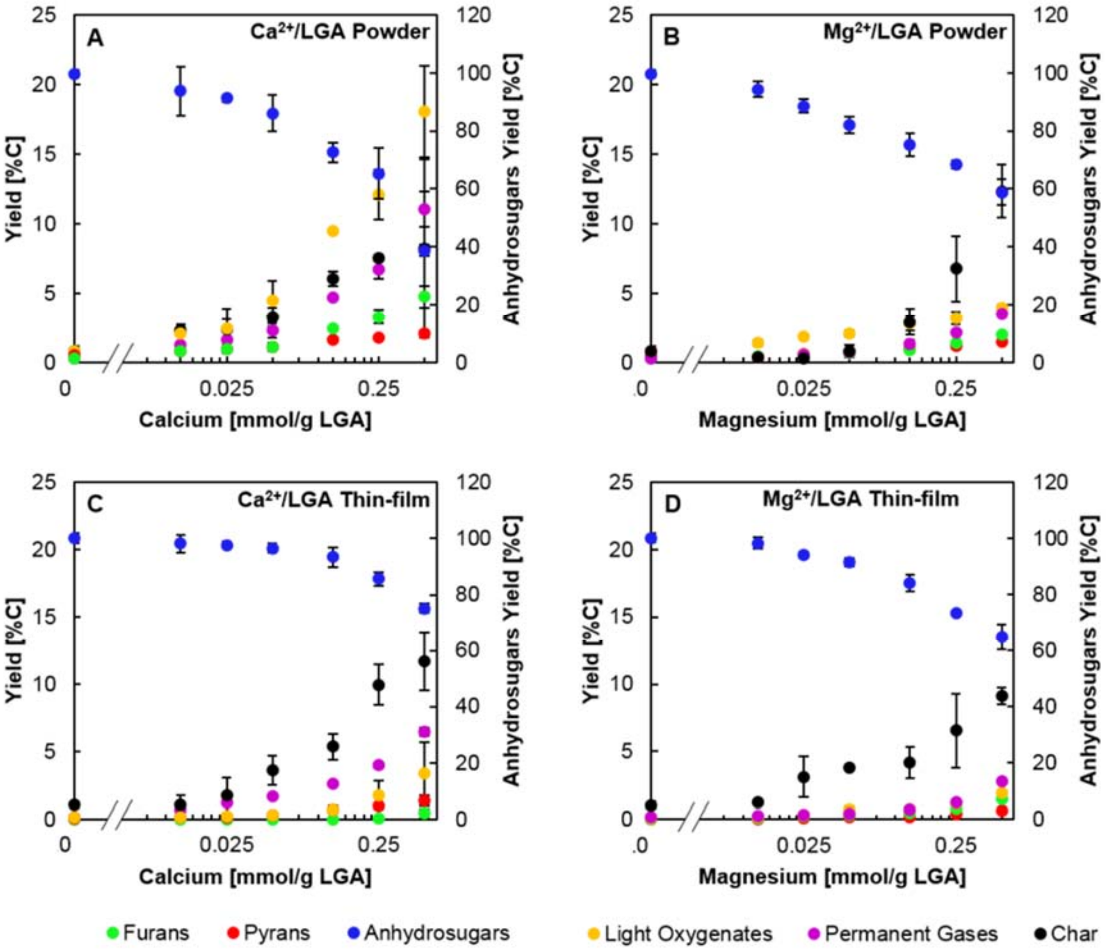

Figure 4.12. Pyrolysis product distribution for Ca^{2+}/LGA and Mg^{2+}/LGA powder and thin-film samples. *Yields of anhydrosugars, pyrans, furans, light oxygenates, permanent gases, and char are shown for (A) Ca^{2+}/LGA powder pyrolysis, (B) Mg^{2+}/LGA powder pyrolysis, (C) Ca^{2+}/LGA thin-film pyrolysis, and (D) Mg^{2+}/LGA thin-film pyrolysis. Error bars represent a 90% confidence interval and are not shown if smaller than the width of symbols.*

The impact of calcium and magnesium ions on the yields of HMF, furfural, and formaldehyde for both powder (millimeter scale) and thin-film (micrometer scale) pyrolysis are depicted in Figure 4.13. Levoglucosan reacts to form increasing amounts of HMF (Figure 4.13A), furfural (Figure 4.13B) and formaldehyde (Figure 4.13C) with increasing calcium and magnesium ions concentration. Of particular note is the concurrent increase in formaldehyde and furfural yields (Figure 4.13B and C) for Ca^{2+}/cellulose powder pyrolysis, which further suggests that HMF undergoes secondary reactions to form furfural and formaldehyde within the melt phase. Again, calcium ions are found to be more active than magnesium in catalyzing secondary reactions.

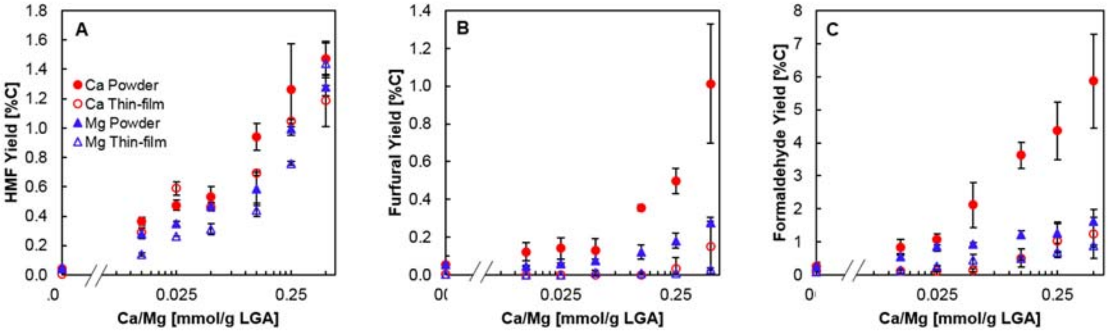

Figure 4.13. Comparison of product yields for Ca^{2+}/LGA and Mg^{2+}/LGA powder and thin-film samples. *Ca^{2+}/LGA powder results (red solid circles), Ca^{2+}/LGA thin-film results (red hollow circles), Mg^{2+}/LGA powder results (blue solid triangles), Mg^{2+}/LGA thin-film results (blue hollow triangles). Yield of (A) HMF, (B) furfural, and (C) formaldehyde are compared for powder (millimeter scale) and thin-film (micrometer scale) experiments as a function of metal ions loading amount. Error bars represent a 90% confidence interval and are not shown if smaller than the width of symbols.*

4.7 Overall Impact of Natural Catalysts on Bio-Oil Quality

The effect of alkaline earth metals on bio-oil production from cellulose pyrolysis can be evaluated by the overall yield of organic vapors as well as the quality of the vapor products. Figure 4.14 depicts the total bio-oil yield (Figure 4.14A), average carbon number (Figure 4.14B), and carbon-to-oxygen (C/O) ratio (Figure 4.14C) of bio-oil produced from cellulose powder and thin-film pyrolysis with both calcium and magnesium catalysts. Metal ions reduced the total bio-oil yield of powder cellulose pyrolysis (73%) to 53% from calcium-doped cellulose and 54% from magnesium-doped cellulose as shown in Figure 4.14A. Bio-oil yield was also reduced under thin-film conditions, but not to the same extent. Loss in yield resulted from increased char production as well as an increased formation of permanent gases.

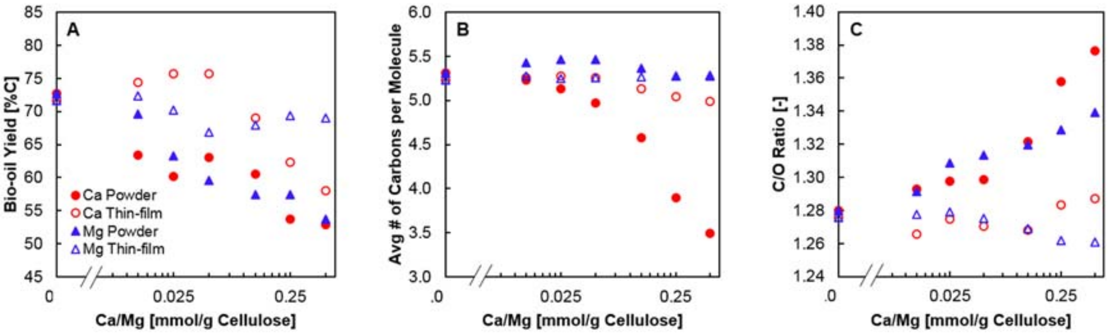

Figure 4.14. Bio-oil quality. *(A) Total bio-oil yield, (B) average carbon number, and (C) carbon-to-oxygen ratio of liquid bio-oil as a function of metal ion concentration are shown for* Ca^{2+}*/cellulose and* Mg^{2+}*/cellulose powder and thin-film pyrolysis.*

Magnesium-catalyzed cellulose pyrolysis exhibited no significant change in carbon number, with 5.3 carbons per molecule under all conditions (Figure 4.14B). In contrast, calcium ions significantly reduced the average carbon number from 5.3 to 3.5 under powder pyrolysis conditions, corresponding to a bio-oil comprised of smaller molecular weight species. This is consistent with our previous results that calcium ions enhance secondary decomposition of levoglucosan (C6) to light oxygenates (C2-C4). Determination of the C/O ratio reveals a significant decrease of oxygen content in bio-oil produced from catalytic powder pyrolysis. As shown in Figure 4.14C, the C/O ratio remains about constant under thin-film pyrolysis conditions for all catalyst loadings. However, under diffusion-limited conditions, the C/O ratio increases from about 1.28 to about 1.35 for both calcium and magnesium ions.

4.8 Ca^{2+} and Mg^{2+} Promoted Pathways in Cellulose Pyrolysis

A key question regarding cellulose pyrolysis is whether the most abundant pyrolysis product, levoglucosan, undergoes secondary reactions during fast pyrolysis. Zhou et al. [125], [126] included no LGA secondary reactions in their computational model because no degradation of pure LGA was observed under fast pyrolysis condition. LGA has a boiling point of 384 °C, which they argued would lead to LGA volatilization before any secondary decomposition could take place at a typical pyrolysis temperature of 500 °C. Lin et al. [108] proposed that LGA can undergo isomerization and dehydration reactions to form other anhydro-monosaccharides followed by subsequent fragmentation and retro-aldol condensation reactions to produce low molecular weight species. Additionally, co-pyrolysis of LGA and fructose showed that LGA reacts within molten biomass to form pyrans and light oxygenates. [116] Here, we find evidence that when exposed to alkaline earth metals, LGA reacts to form small molecular species such as furans and light oxygenates.

5-Hydroxymethylfurfural (HMF) and furfural are the most abundant furans with 1.5% and 1.0% yield from Ca^{2+}/LGA powder pyrolysis (Figure 4.13A and B). A secondary reaction pathway of LGA catalyzed by metal ions therefore must include production of furans, as shown in Figure 4.15. Such a reaction is likely initiated by cleavage of the carbon-oxygen bridge as well as the pyran ring to form a C1 carbonyl group. [115] Saddawi et al [105] found that the C5-O5 bond in LGA was weakened by the interaction between oxygen and metal ions, which implies that pyran ring opening reactions are catalyzed by metal ions. This is followed by re-closure of the ring at the C2 carbon, and formation of a hydroxyl group at the C6 carbon. [115] Paine et al [127] have also shown that the five-membered carbon-oxygen furan ring structure is formed via cyclization at C2 carbon followed by dehydration. Further dehydration of the intermediate, 2,5-anhydro-D-mannose, then yields one HMF molecule and two water molecules. [125] The yield of HMF from Ca^{2+}/cellulose powder pyrolysis decreased as the calcium loading was increased (Figure 4.11B), which coincides with an increase in furfural yield (Figure 4.11C). This suggests that calcium ions catalyzed breaking of the C5-C6 bond in HMF to form furfural and a C1 species, possibly carbon monoxide or formaldehyde, both of which also increase in yield with increased calcium loading. While this reaction could account for some of the increased formaldehyde production, it cannot account for all of it, as the yield of formaldehyde increased by 5.6% (Figure 4.13C) compared to 1.5% for furfural. Therefore, other catalytic routes must exist to form formaldehyde.

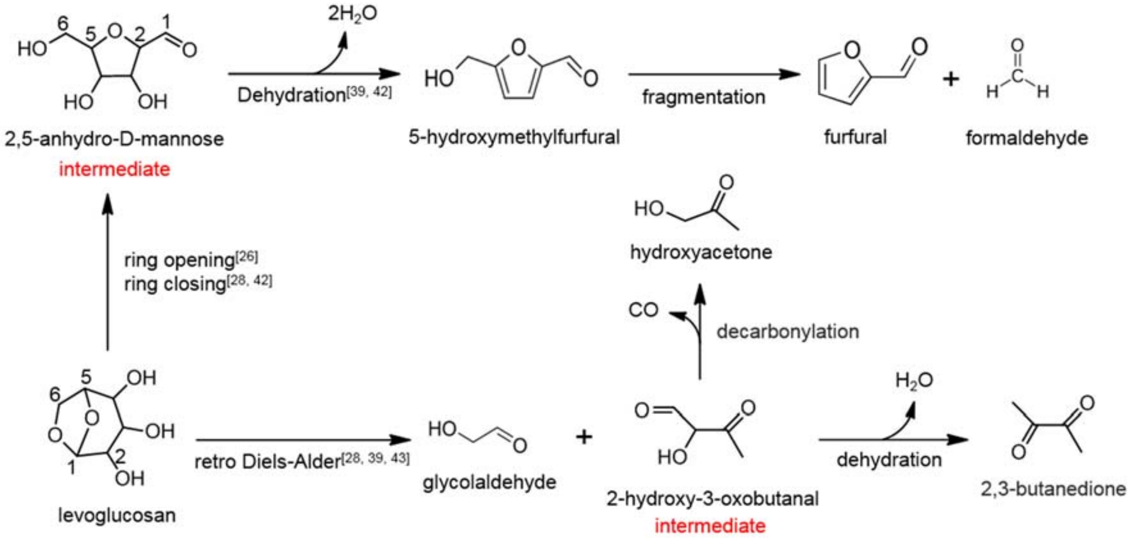

Figure 4.15. Mechanism of levoglucosan secondary reactions to form furans and C2-C4 products.

Another secondary pathway catalyzed by metal ions is LGA conversion to C2-C4 light oxygenates. Yields of glycolaldehyde (two-carbon species) and 2,3-butanedione (four-carbon species) both increase to 1.0% in Ca^{2+}/LGA powder pyrolysis. This nearly identical increase in yield suggests that the two-carbon glycolaldehyde and four-carbon 2,3-butanedione are produced through the same reaction. The retro Diels-Alder reaction has been reported to be important for the formation of glycolaldehyde during cellulose pyrolysis. [125], [128] As depicted in Figure 4.15, the reaction is initiated with C4–C5 bond scission, accompanied by the breaking of the carbon-oxygen bridge in LGA. Since the C5 carbon is short of one valence bond, it forms another carbonyl group with the O5 oxygen, resulting in the cleavage of the C1–O5 bond. [115] This process leads to the formation of glycolaldehyde and another C4 compound, 2-hydroxy-3-oxobutanal, which can undergo dehydration to produce 2,3-butanedione and water or decarbonylation to yield hydroxyacetone and carbon monoxide.

Figure 4.16 summarizes the primary (thin-film) and secondary (powder) pathways of cellulose pyrolysis. Thin-film length scale reduces the residence time of volatiles within the intermediate liquid and minimizes secondary reactions. Therefore, any effect on pyrolysis yields caused by the addition of calcium or magnesium ions during thin-film pyrolysis is actively catalyzing primary reactions. From the thin-film studies, we can conclude that calcium ions catalyze the reactions that form primary char at the expense of LGA production. Magnesium ions, however, have no significant effect on the primary chemistry that determines the product distribution of cellulose thin-film pyrolysis.

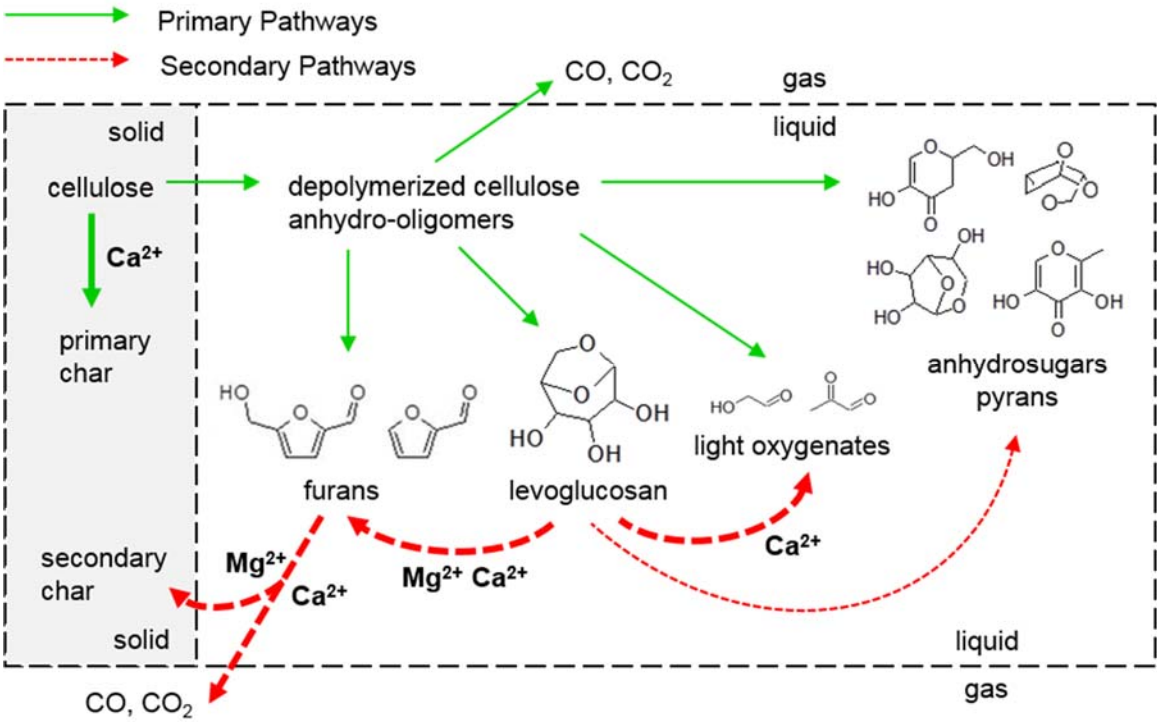

Figure 4.16. Effect of natural inorganic catalysts on primary and secondary pyrolysis chemistry. *Calcium catalyzes primary char formation and secondary reactions to light oxygenates and permanent gases, while magnesium mainly catalyzes secondary char formation.*

The most significant effect of calcium and magnesium ions is the promotion of specific secondary reactions. This secondary chemistry only exists when the pyrolysis length scale is sufficiently large for mass transfer limitations to occur. In such a case, as products are formed, they must diffuse through the cellulose melt and can react before volatilizing and leaving the particle/droplet. Powder (mass transfer-limited) experiments revealed that secondary reactions of anhydrosugars (especially LGA) are catalyzed by calcium and magnesium ions. This is especially evident in the increase of light oxygenates yield from Ca^{2+}/cellulose (Figure 4.9A) and Ca^{2+}/LGA powder experiments (Figure 4.12A), where calcium ions largely catalyze LGA to decompose to light oxygenates. In contrast, magnesium ions do not appear to influence this reaction since light oxygenates yield is unaffected by magnesium concentrations in Mg^{2+}/cellulose powder pyrolysis (Figure 4.9B).

The formation of secondary char was also strongly catalyzed by alkaline earth metals. This is most evident from the Mg^{2+}/cellulose powder and thin-film experiments. During thin-film experiments, the char yield was approximately 12% (Figure 4.9D) regardless of the magnesium concentration, which shows that the formation of primary char is unaffected by magnesium ions. A different result was observed from the Mg^{2+}/cellulose powder experiments where the char yield increased to approximately 25% (Figure 4.9B). The difference in char yields between the thin-film and powder experiments can only be explained by magnesium ions catalyzing the formation of secondary char. The same result (if less extreme) is observed with the addition of calcium ions. In contrast, calcium ions do catalyze the formation of primary char and so the true extent of secondary char formation is more difficult to determine. The source of secondary char is likely furan species and light oxygenates. Brewer and coworkers [129] carried out the characterization of char formed from biomass pyrolysis and revealed that char was of high aromaticity, largely contributed by ether groups which are likely from furans. Aldehydic furans, alcohols and aldehydes serving as char precursors are prone to form char through polymerization reactions such as aldol-condensation. [130] While the yields of furans remain mostly constant during Ca^{2+}/cellulose and Mg^{2+}/cellulose powder pyrolysis (Figure 4.9A and B), they do increase during Ca^{2+}/LGA and Mg^{2+}/LGA powder experiments (Figure 4.12A and B). This suggests that calcium and magnesium ions catalyze secondary reactions of LGA to furans, followed by consumption of furans to from secondary char. Char formation was also associated with the production of permanent gases like CO and CO_2, which both increased in Ca^{2+}/cellulose (Figure 4.9A) and Ca^{2+}/LGA (Figure 4.12A) powder pyrolysis.

4.9 Conclusions

The catalytic effect of alkaline earth metals on primary and secondary cellulose pyrolysis was studied by doping cellulose and levoglucosan with calcium or magnesium nitrate salts and their oxides. Metal oxides were shown to have negligible impact on the distribution of cellulose pyrolysis products, while metal ions doped via ion-exchange were active for cellulose decomposition. Comparison of cellulose pyrolysis products under isothermal (thin-film) and transport-limited (powder) conditions revealed that alkaline earth metals primarily act on secondary (diffusion-limited) reactions of volatile species within molten cellulose. Calcium ions were more active than magnesium ions, and they were capable of promoting primary formation of char from cellulose, conversion of levoglucosan to light oxygenates and furans, and consumption of furans to secondary char and permanent gases. The addition of either calcium or magnesium ions to cellulose increased the C/O ratio of the bio-oil suggesting that there is some benefit (i.e. deoxygenation) to the presence of these metal ions, despite the decrease of bio-oil yield and increase in low molecular weight species.

Chapter 5. Kinetics of Cellulose Glycosidic Bond Cleavage

5.1 Introduction

Thermochemical conversion of lignocellulosic biomass to renewable transportation fuels occurs at high temperatures (300 – 800 °C) to decompose large biopolymers (20,000 to 400,000 a.m.u.) into smaller molecules with higher stability and energy content. [3] Gasification above 800 °C produces one-carbon synthesis gas products, while pyrolysis targets C2-C6 organic compounds which condense to a moderately stable liquid referred to as 'bio-oil'. [131], [132] While existing thermochemical processes are potentially economical, [133], [134] widespread implementation requires detailed design based on detailed understanding of the molecular reactions of biomass. [89]

Cellulose is the primary component of lignocellulose, comprising over 50% of common biomass feedstocks considered for renewable energy applications. Cellulose is a linear homopolymer of glucose monomers formed by condensation polymerization; β-(1-4) glycosidic bonds connect monomers forming long chains which crystallize into dense sheets. [135] Thermal fragmentation above 300 °C produces aerosols [12] and hundreds of volatile organic compounds including anhydrosugars, furans, pyrans, permanent gases, and light oxygenates such as glycolaldehyde or 2,3-butanedione. [115], [136] At lower temperatures (<400 °C), increased char formation is observed, [137] while cellulose rapidly liquefies and evaporates near 500 °C where optimum yield of volatile organic compounds is obtained. [110], [138]–[140]

While numerous kinetic models have been proposed to characterize cellulose decomposition, the specific chemical reaction mechanisms to form volatile components remain unknown. Global kinetic models comprised of lumped species organized by phase (e.g. solid char, intermediate ‘active’ cellulose) characterize the overall conversion of cellulose, but a broad range of fitted kinetic parameters (activation energies, E_a, of 10 to 63 kcal/mol) indicate that lumped models are too simple to capture the complexity of cellulose chemistry above 400 °C. [141] More detailed molecular models have been proposed based on the formation of glucose via hydrolysis as a key intermediate for formation of light oxygenates, furans, pyrans and permanent gases. [126], [142]–[144] However, glucose has been shown to produce a substantially different distribution of products relative to cellulose, [122] and glucose has not been observed as a reactive intermediate in cellulose decomposition. Moreover, development of molecular models of cellulose has utilized calculated activation energies and fitted model parameters. Due to the complexity of the chemistry and extent of unknown parameters, model comparison with cellulose product yields provides insufficient temporal detail for model development and validation.

5.1.1 Identification of Cyclodextrin as Cellulose Surrogate

Insight into the chemistry of cellulose decomposition has been gained from comparison of the pyrolysis product yields of cellodextrins. Pyrolysis of films of cellulose (10-20 μm thick) are sufficiently thin to undergo reaction without heat or mass transport limitations; organic vapors produced under thin film conditions are thus indicative only of the intrinsic cellulose chemistry. [115]

One important insight was the observation that the pyrolysis product yields of cellulose and α-cyclodextrin, a six-monomer ring polysaccharide, were identical within experimental error. [115] Figure 5.1A shows that α-cyclodextrin yields agree well with those of cellulose for nearly all major products (with the exception of formic acid). This agreement shows that α-cyclodextrin is largely representative of cellulose in flash pyrolysis. In addition to α-cyclodextrin, two other commercially-available cyclodextrins were also compared to cellulose. Figure 5.1B and C show that β- and γ-cyclodextrin, like α-cyclodextrin, produce similar pyrolysis products to cellulose and are appropriate surrogates as well.

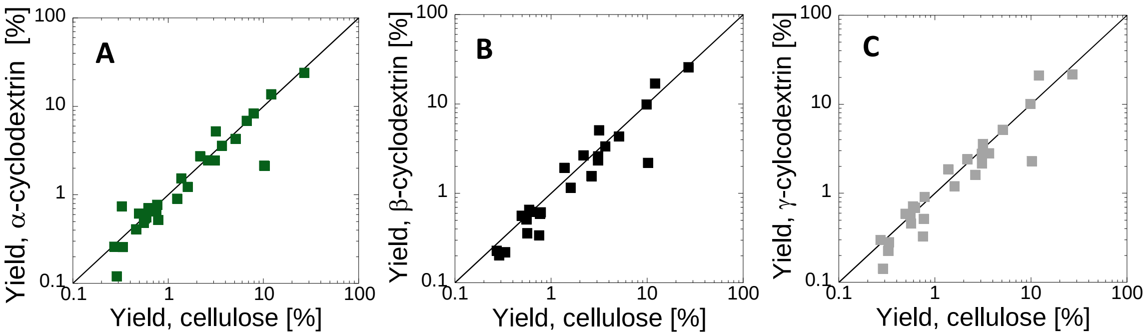

Figure 5.1. Comparison of major thin-film pyrolysis products of α-cyclodextrin. *(A), β-cyclodextrin (B) and γ-cyclodextrin (C) to cellulose at 500 °C.* [115]

These cyclic polymers are comprised of six, seven, or eight α-linked glucose monomers. They all have an end-group to monomer ratio of zero making them similar to cellulose in this respect (cellulose has an end-group to monomer ratio that is near zero: 0.01-2%). This information indicates that end-group-to monomer ratio, which is very different between glucose (100%), cellohexaose (33%) and cellulose (0.01–2%) but similar between α-cyclodextrin (0%) and cellulose, is a vital descriptor of cellulose pyrolysis chemistry. Based on this finding and the demonstrated similarities in product yields, α-cyclodextrin is found to the appropriate surrogate for cellulose.

Another important difference between α-cyclodextrin and cellulose is the linkage type. Glucose monomers that make up cellulose are connected by equatorial ether bridges (β-linkage) while α-cyclodextrin is constructed from axial ones (α-linkage). To evaluate the effect of linkage type on pyrolysis products, we compared two sets of maltodextrins (α-linked) and cellodextrins (β-linked). Figure 5.2A shows pyrolysis product yield for maltobiose and cellobiose at 500 °C, whereas Figure 5.2B compares maltohexaose and cellohexaose. By thin-film pyrolysis of feedstocks which differ only by the linkage type, it is apparent that identical products are obtained from either feedstock; polysaccharides undergo the same mechanisms with either α-(1-4) or β-(1-4) glycosidic bonds. [115]

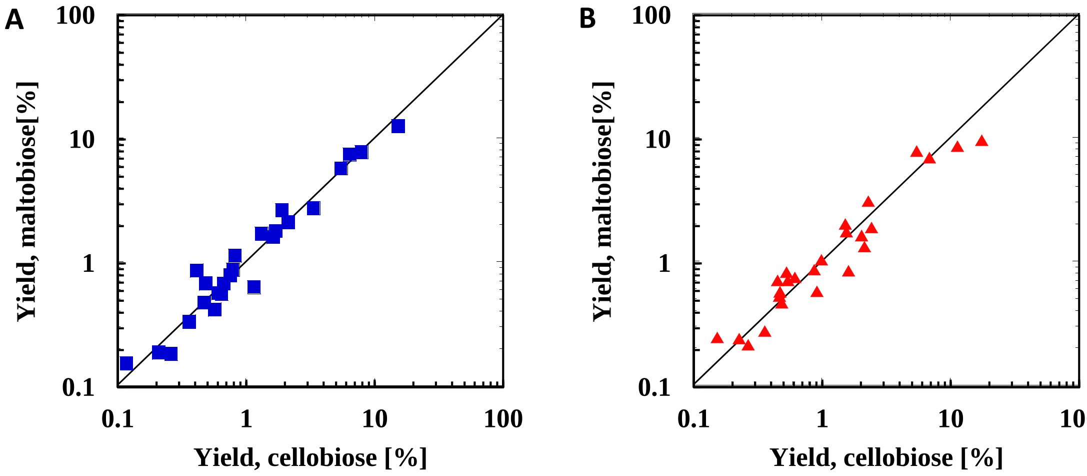

Figure 5.2. ***Role of glycosidic linkage.*** *The effect of glycosidic linkage is shown by comparing α-linked (maltodextrins) and β-linked (cellodextrins) glucose polymers. Pyrolysis products are used to compare maltobiose and cellobiose (A) as well as maltohexaose and cellohexaose (B). The reaction temperature was 500 °C.* [115]

5.1.2 Design and Validation of PHASR System

Current pyrolysis mechanisms and nature of intermediates are proposed based on initial and final pyrolysis compositions from a variety of experimental reactors and conditions which are inadequate to capture kinetics. [10]–[14] Thus, quantifying the role of alkaline earth metals within the intermediate liquid requires an entirely new experimental apparatus. We solved this problem by building an innovative device called "Pulse-Heated Analysis of Solid Reactions," short for PHASR reactor, capable of capturing kinetic data in extremely short timescale of milliseconds. [145] Thin-film samples were made to study reaction chemistry and kinetics that are absent of heat and mass transfer limitations. [14], [88] This method rapidly heats thin films of cellulose (>10^6 °C/min), maintains the cellulose film at a prescribed temperature (e.g. 460 °C), and then rapidly quenches.

Requirements for heating and cooling timescales are determined using a combined heat transfer and Shafizadeh lumped kinetics model. [113] It has been shown that the pyrolysis of cellulose at low pressure (1.5 Torr) can be described by a three reaction model. In this model, it is assumed that an "initiation reaction" leads to formation of an "active cellulose" which subsequently decomposes by two competitive first-order reactions, one yielding volatiles and the other char and a gaseous fraction. Over the temperature range of 259-341 °C, the rate coefficients of these reactions, k_1 (for cellulose → "active cellulose"), k_2 (for "active cellulose" → volatiles), and k_3 (for "active cellulose" → char + the gaseous fraction) are given by $\mathrm{k_1 = 1.7 \times 10^{21} e^{-(58000/RT)} min^{-1}}$, $\mathrm{k_2 = 1.9 \times}$

$10^{16}e^{-(47300/RT)}\mathrm{min}^{-1}$, and $k_3 = 7.9 \times 10^{11}e^{-(36600/RT)}\mathrm{min}^{-1}$. From the lumped kinetic rate equations,

$$\frac{dY_{cellulose}}{dt} = -k_1 Y_{cellulose} \tag{5.1}$$

$$\frac{dY_{int.liq.}}{dt} = k_1 Y_{cellulose} - k_2 Y_{int.liq.} \tag{5.2}$$

$$\frac{dY_{vol.prod.}}{dt} = k_2 Y_{int.liq.} \tag{5.3}$$

At the same time, we defined the temperature profile as

$$t < t_0, T = 273K \tag{5.4}$$

$$t \geq t_0, T = 273K + \frac{\Delta T}{\Delta t}(t - t_0), \text{up to } T_{max} = 773K \tag{5.5}$$

$$t \leq t_1, T = 773K - \frac{\Delta T}{\Delta t}(t - t_1), \text{down to } T_{min} = 273K \tag{5.6}$$

These equations were modeled using MATLAB and the mass fraction and temperature profile change of cellulose pyrolysis obtained from these calculations are shown in Figure 5.3.

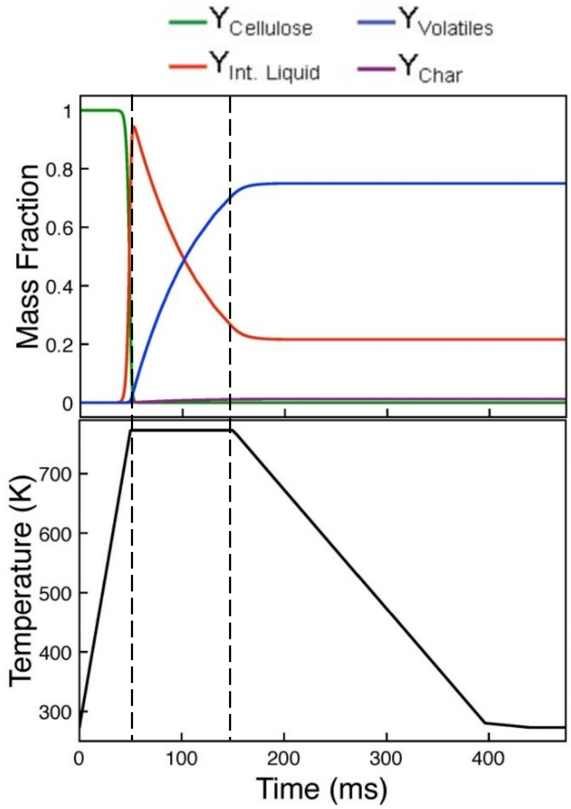

Figure 5.3. Mass fraction and temperature profile change of cellulose pyrolysis. *(A) Mass fraction of cellulose, intermediate liquid, volatiles, and char; (B) temperature profile of cellulose pyrolysis as reaction time evolves. Minimum heating and cooling times of 50 ms and 250 ms at 500 °C, respectively, indicates minimal volatiles formation (<5%) during the heating and cooling stages, serving as targets for experimental validation of the PHASR reactor.* [145]

To reduce reaction during the heating stage from 0 to 500 °C (Figure 5.3B), cellulose should be heated up in 50 ms to keep mass fraction as one (Figure 5.3A). When the temperature reached 500 °C and holding, solid cellulose converted to intermediate liquid at once and decomposed to volatiles and char (Figure 5.3A). To acquire accurate composition of the pyrolysis intermediate, we need to cool down the reactor from 500 to 0 °C fast enough before mass fraction of intermediate liquid goes to zero and avoid further reaction during cooling stage as well. Thus, samples must be heated in under 50 ms and cooled in under 250 ms to obtain isothermal and purely kinetic data without any transport limitations. The PHASR system has a capability to precisely program the temperature between 250 °C and 1350 °C. As depicted in Figure 5.4, heating from room temperature to 500 °C can be achieved in 30 ms and cooling down in 150 ms such that less than 3% of volatiles and char products are produced during this heating and cooling procedure.

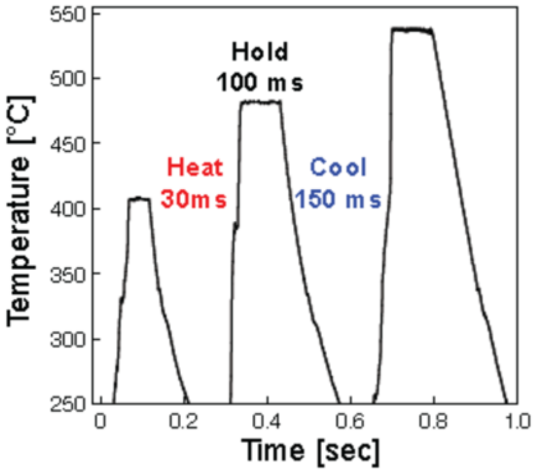

Figure 5.4. Temperature-time profiles generated using PHASR reactor. *It shows capability to heat in less than 35 ms and cool in under 150 ms.* [145]

The schematic of the PHASR reactor shows the micro-reactor consists of two sections namely heating and cooling block (Figure 5.5). An electrical insulator made of aluminum nitride is used between the heating element and the cooling block to avoid short circuit and provide rapid thermal conduction in the meanwhile. The requirement of high cooling rates is addressed by employing Syltherm which is a silicone fluid as a coolant. High-velocity coolant flows through the micro-finned heat exchanger in the cooling block which can rapidly cool the sample after heating phase. Helium is used as a carrier gas which quenches the gas-phase reactions by quickly sweeping pyrolysis products into gas chromatograph held at cryogenic temperatures. The helium residence time in the PHASR reactor is extremely short, about 10 milliseconds. Cartridge heaters are applied at the outlet of the micro-reactor to prevent pyrolysis products (such as levoglucosan) from condensation before flowing into the GC column.

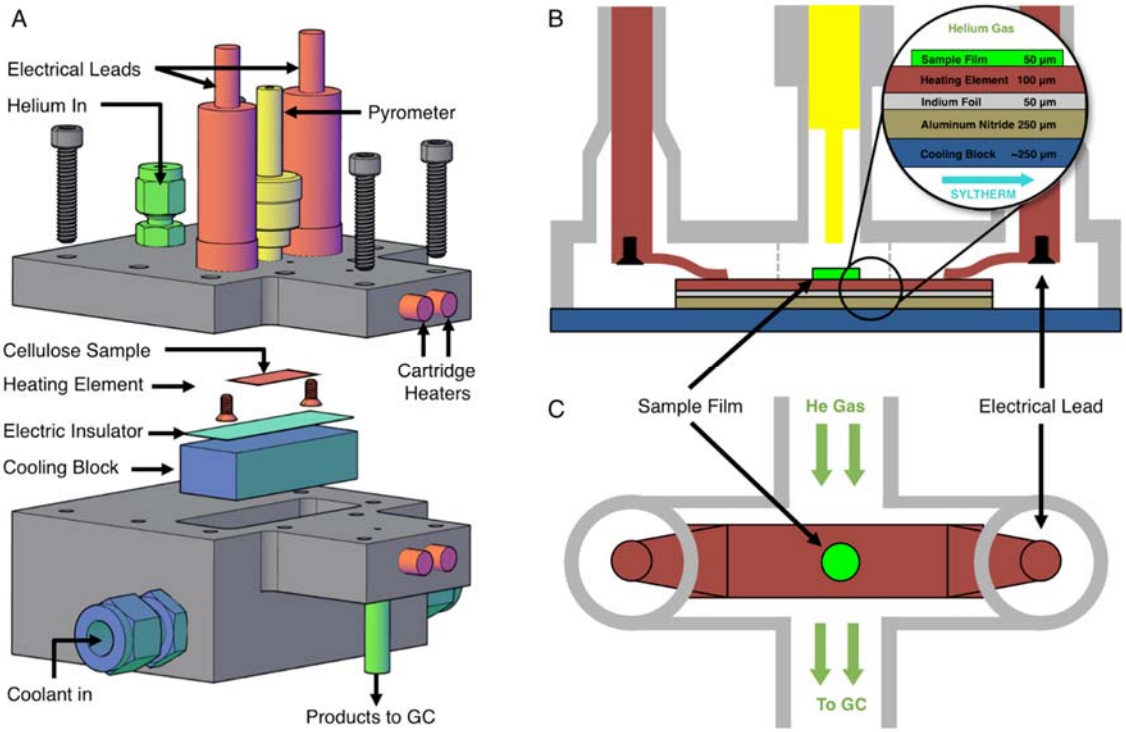

Figure 5.5. PHASR Reactor Diagram. *A. Exploded diagram of the PHASR (Pulse-Heated Analysis of Solid Reactions) system. Cellulose film samples on a heating element are attached to electrical leads within a helium-flow chamber; gas/vapor effluent flows into a gas chromatograph. A lower chamber contains continuously flowing silicon-based coolant. B. Gas flow chamber contains curved metal contacts connecting copper electrical leads and the heating element. Multiple layers of heating element, indium foil, aluminum nitride and a copper micro-channel cooling block transport heat between the gas and liquid chambers. Optical pyrometer in yellow measures the temperature at 1000 Hz. C. Top-down view of the heating element.* [145]

Shown in Figure 5.6, the PHASR reactor has a capacity to handle biomass samples from 10 to 500 μg. Sample loaded on the steel heating element is resistively heated via electrical leads connected to a transformer. A 1000 Hz optical pyrometer is used for measuring the pyrolysis temperature with a signal converter translating the thermal radiation to electrical signals sent to the 2000 Hz PID control unit. PID parameters used for the power supply are modelled and optimized by MATLAB Simulink to achieve precise control of temperature. As the heating element needs large current, a transformer of ratio 1:72 is applied to convert the low current of the power supply to 2 kA for the resistive heating. Pyrolysis products from the PHASR reactor are identified and quantified via GC-MS analysis. The PHASR micro-reactor is the first technology for measuring high temperature millisecond-scale solid state reactions, providing capability to elucidate kinetics of previously immeasurable reactions, such as cellulose decomposition.

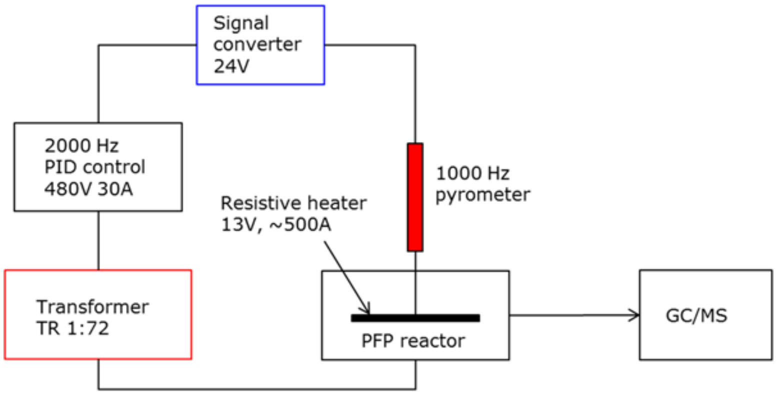

Figure 5.6. Schematic diagram of the PHASR heating system. *It shows the layout of the 1000 Hz PID heating controller and direct integration with analytical equipment.*

5.2 Experimental Methods

By employing the PHASR reactor, the products of cellulose pyrolysis including unreacted cellulose residue and volatile organic products are quantified for the prescribed reaction time, and the rate of conversion and formation of high temperature materials is calculated.

5.2.1 PHASR Reactor

Precise temperature control of reacting cellulose and α-cyclodextrin films was achieved with the PHASR method, by which reactant samples were subjected to rapid thermal pulses for prescribed temperatures and time intervals. The PHASR reactor incorporated millisecond heating and cooling of samples with analytical integration for identification and quantification of gas and volatile products. The reactor housing, shown in Figure 5.5A, combined an upper heating section with integrated electrical leads and optical temperature measurement and a lower cooling section with a micro-structured heat exchanger for cooling.

The top and bottom sections of the PHASR reactor were custom machined from 316 stainless steel with micro-welded fittings for electrical feedthroughs (MPF Products Inc. PN: A1016-1-W) and the pyrometer (Swagelok UltraTorr, PN: SS-4-UT-A-4). The two reactor halves closed together with a custom-cut polytetrafluoroethylene (PTFE) gasket to form the reaction chamber, through which helium carrier gas flowed into the top portion of the reactor via an NPT fitting (Swagelok PN: SS-100-1-1) and out through a welded fitting (Vici Valco PN: ZLTA41). The bottom section of the PHASR reactor incorporated a custom micro-machined heat exchanger (MicroCooling Concepts, PN: SA-5A), through which high velocity heat transfer fluid (Dow Chemical, Syltherm-800) was pumped. The PHASR reactor was heated via five cartridge heaters (Omega, P/N: 00034) and a custom nozzle heater (Nexthermal) for complete transfer of volatile products to the gas chromatograph.

Inside the PHASR reaction chamber, shown in Figure 5.5B and 5.5C, the electrical leads were connected to custom-machined and bent copper contacts, which pressed down onto the heating element to provide electrical contact. The custom cut heating elements were in thermal contact with the micro-machined heat exchanger across an aluminum nitride layer (Stellar Industries, PN: ALN 2.0" x 2.0" x 0.010"), which electrically insulated the heating element from the reactor, and an optional indium foil layer (Indium Corporation, PN: Ribbonin-10101), which reduced cooling times by enabling improved thermal contact. During a thermal pulse, the indium foil melted (T_M ~ 250 °C) to form a molten interface between the heating element and the aluminum nitride layer, improving heat transfer. After a pulse, the indium layer re-solidified for easy sample removal.

Millisecond temperature control of reactant samples via electrical resistive heating was achieved using an integrated resistive heating power supply and 2000 Hz PID controller (Amada-Miyachi HF2 with IT-1140-T transformer) and an infrared optical pyrometer (Impac PN: IGA-50-LO with sapphire light pipe PN: LP2-18.5mm), which measured the sample temperature via optical emission spectroscopy at 1000 Hz for feedback to the controller. The 0-20 mA output from the pyrometer was converted to a 0-10 V signal for feedback to the PID controlled using a signal converter (Phoenix Contact PN: 2811284). The pyrometer light pipe was inserted into the Swagelok UltraTorr fitting on the PHASR reactor to directly measure the sample temperature. Custom manufactured electrical leads connected the resistive heating transformer to the PHASR reactor using a bus-bar interconnect (Tyco Electronics PN: 6648234-1) which attached to the electrical feedthroughs.

The resistive heating power supply was operated in ‘dual-pulse’ mode; a first pulse with preset current and duration heated the sample above 250 °C, and a second pulse incorporated the PID feedback temperature to complete sample heating and held the sample at reaction temperature for a preset duration. At the completion of a pulse, the power supply turned off and the cooling system quenched the sample.

To achieve rapid cooling of PHASR samples, the Syltherm heat transfer fluid was circulated through the micro-machined heat exchanger. The silicon-based coolant was selected for its high thermal stability, ensuring rapid cooling after a pulse. Coolant temperature was held at 3 °C, and flow was maintained using a refrigerated circulating bath

(Thermo-Fisher PN: Isotemp 4100, R20). During a thermal pulse, the overall coolant velocity was increased using an in-line booster pump (McMaster-Carr PN: ShurFlo 4272K21). All components of the cooling loop were connected via 3/8” copper tubing.

The PHASR reactor was integrated with an Agilent 7890A gas chromatograph (GC) with Agilent 220 Ion Trap mass spectrometer (MS). The reactor was spliced between the helium electronic pressure controller (EPC) and the inlet. The outlet of the PHASR reactor fed directly into the Agilent split/splitless inlet via 1/16” stainless steel wide-bore tubing. Gas and volatile products that evolved from the reacting films were transferred to the GC, which contained a dual-column, dual-detector configuration with cryogenic focusing. First, products were transferred to an Agilent DB-5 column (320 μm x 30m, 1.5 μm stationary phase), through which permanent gases (CO, CO_2) rapidly eluted onto a second gas separation column (Agilent Plot-Q, 320 μm x 30m, 20 μm stationary phase) via a GC-integrated switching valve (Vici Valco, 4 port). After gases were transferred to the secondary column, a valve switch sent all remaining eluents to a splitter, which split flow to a flame ionization detector (FID) for quantification and MS for identification. Permanent gases eluting from the Plot-Q column were quantified using thermal conductivity detector. Separation of gas and volatile products was performed using a 90 minutes GC method, which ramped from -30 °C to 260 °C.

To perform a PHASR reaction, a heating element containing a sample was loaded into the reactor, and the two reactor halves were sealed together. Cartridge heaters were pre-heated while the GC method was activated to begin helium flow through the reactor and cool the oven to cryogenic temperatures. Upon initiation of a PHASR reaction, current was applied to the resistive heating element to heat the sample to the desired reaction temperature in under 30 ms, after which sample temperature was maintained at the desired reaction temperature via PID feedback control for 0-2000 ms. At the completion of a PHASR pulse, the power supply turned off and the sample was rapidly quenched in under 150 ms via the high velocity coolant. Completion of the thermal pulse triggered the start of the GC/MS method, from which gas and volatile products evolving from the reactant sample during the thermal pulse were identified and quantified. PHASR pulses of increasing length were performed to quantify the evolution of products and the consumption of reactants, as depicted in Figure 5.7A.

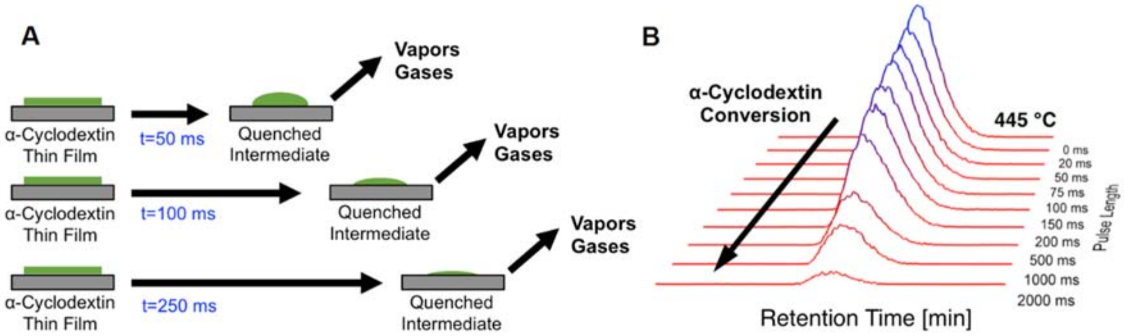

Figure 5.7. PHASR reactor diagram and method. *A. Millisecond-duration pulses enable prescribed reaction times followed by rapid quenching to produce product vapors and quenched intermediate samples. B. Liquid chromatography of quenched intermediate samples of α-cyclodextrin reacted at 445 °C for sequential pulse lengths (20 ms to 2000 ms).*

5.2.2 Cyclodextrin Film Preparation

PHASR samples were prepared via solvent deposition and drying on steel heating elements. PHASR heating elements were cleaned using a butane torch until they turned blue, after which they were allowed to sit for 24 hours. A 1.0 wt% solution of α-cyclodextrin in water was prepared and 5.0 µl pipetted onto the center of the heating element, corresponding to 50 µg of sample. Samples were then placed in a vacuum at 25 in Hg and held at 40 °C for 3 hours. In order to generate 100 µg samples, two solvent depositions and drying procedures were performed in series. This film preparation method generated a uniform, circular film 3 mm in diameter and 20 microns in thickness.

5.2.3 Product Analysis

Quantification of remaining α-cyclodextrin reactant after a pulse was performed via solvent extraction and liquid chromatography with light scattering detection. Heating elements containing partially reacted samples were removed from the PHASR reactor and cut into a small circle that contained only the sample film. The cut heating element was placed into a 1.5 ml PTFE filter vial (Whatman PN: UN203NPEPP). 300 µl of HPLC grade water was pipetted into each vial containing a heating element and vials were sonicated for five minutes to ensure complete dissolution of α-cyclodextrin. After sonication, the remaining metal heating element was removed from the vial and the filter plunger was depressed to remove any remaining particulate. 100 µl of filtered samples were injected into a high performance liquid chromatograph (HPLC, Shimadzu Prominence) with a carbohydrate separation column (Agilent Na Hi-Plex, PN: PL1171-6140) light scattering detector (ELSD-LTII) and water mobile phase. Quantification of the α-cyclodextrin peak from the ELSD for PHASR pulses of increasing length yielded the consumption of reactant with time, shown as a series of stacked chromatograms in Figure 5.7B.

The considered experiments evaluated the conversion of cyclodextrin for a range of temperatures (385 – 505 °C) and reaction times (20 ms to 2000 ms). As shown in Figure 5.8, the PHASR reactor was designed to permit experimental evaluation of solid reactions with variable pulse length and temperature. The depicted thermal pulses demonstrate the potential variation of 20 ms pulses at 385 °C in blue to 2000 ms pulses at 505 °C in purple.

All other combinations of reaction time and temperature were achievable and utilized in the conducted experiments.

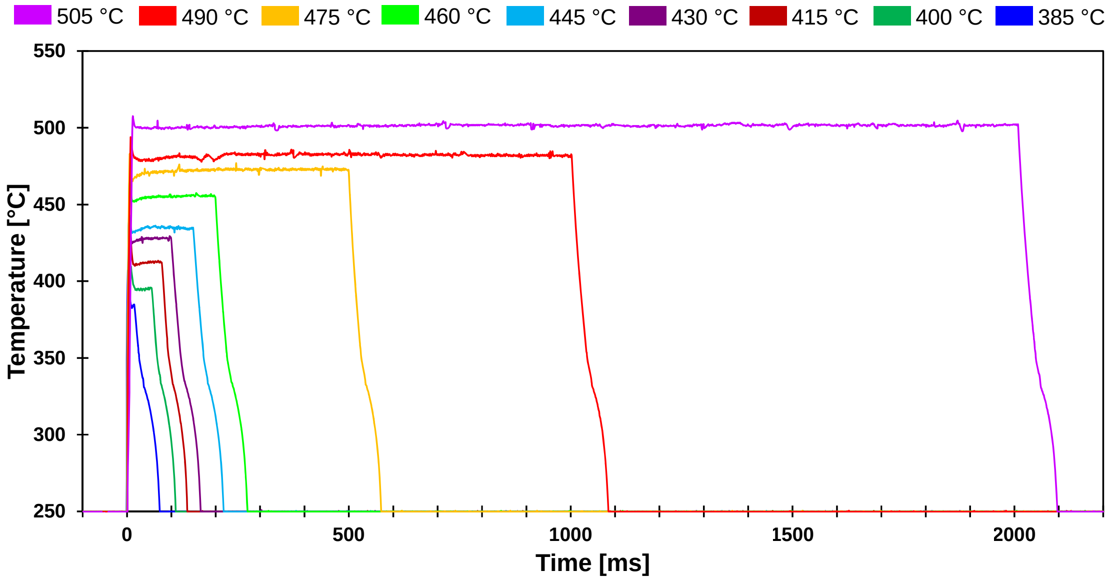

Figure 5.8. PHASR reactor pulse temperatures. *Film samples of α-cyclodextrin were exposed to thermal pulses varying from 20 ms to 2000 ms at temperatures varying from 385 °C to 505 °C.*

5.3 Cyclodextrin as Kinetic Surrogate

Prior experiments with thin films of cellulose and α-, β-, or γ-cyclodextrin demonstrated that these cyclic carbohydrates produced the same yield of pyrolysis products at complete conversion. [115] In a new set of experiments, α-cyclodextrin was evaluated as a kinetic surrogate of cellulose by comparing the rate of formation ($mol_{product}*mol_{cellulose-monomer}^{-1}*s^{-1}$) of pyrolysis products from both α-cyclodextrin and cellulose. Figure 5.9 depicts the rate of formation at five temperatures (400, 425, 450, 475, 500 °C) of eight compounds: carbon dioxide, 2,5-dimethylfuran, 1,2-cyclopentanedione, furfural, 2,3-butanedione, 2(5H)-furanone, levoglucosenone, and 1,4:36-dianhydro-α-d-glucopyranose. By comparison of the product formation rates on individual parity plots, it is evident that both feedstocks (cellulose and cyclodextrin) exhibit identical product formation rates within experimental error. By this analysis, cyclodextrin can be utilized as a kinetic surrogate for the experimental characterization of cellulose decomposition.

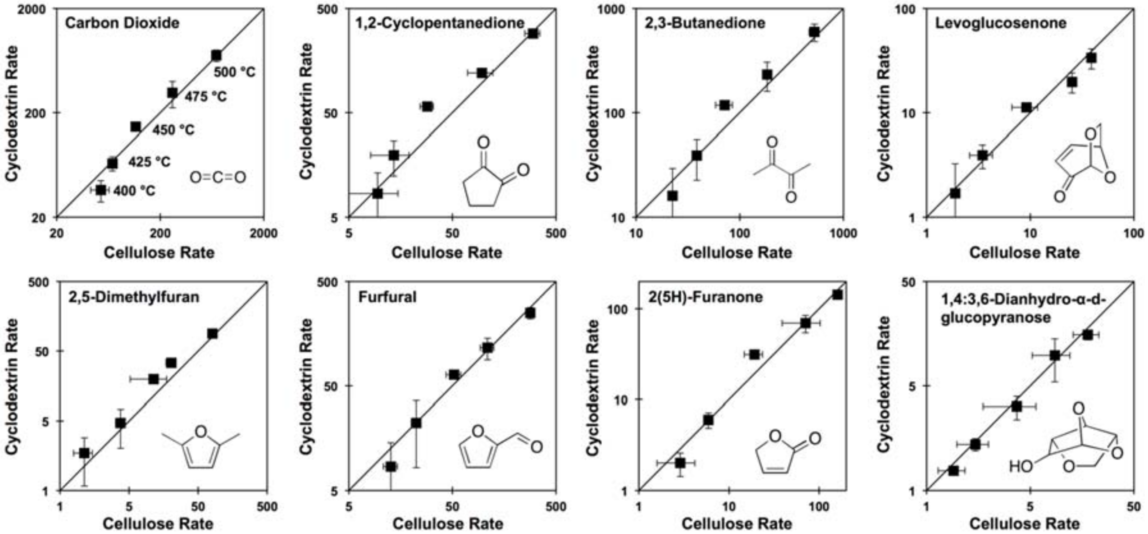

Figure 5.9. Product formation rate parity from α-cyclodextrin and cellulose at 400 - 500 °C. *The rate of formation* $(mol_{product}*mol_{cellulose\text{-}monomer}^{-1}*s^{-1})$ *of volatile products indicates that α-cyclodextrin is a small-molecule surrogate of cellulose. Error bars represent a 90% confidence interval in reaction rate.*

5.4 Cyclodextrin Conversion Kinetics

The conversion of cyclodextrin was measured for pulses of 20-2000 ms and temperatures of 385-505 °C as depicted in Figure 5.10A and B. Each time-temperature combination represented as a single data point in Figure 5.10A was comprised of at least three independent experimental trials; error bars associated with each point represent a 90% confidence interval. From the appearance of the data it is evident that conversion of cyclodextrin exhibits first order kinetics – the rate of cyclodextrin conversion was proportional the remaining quantity of cyclodextrin. For each temperature, a first order kinetic model was fit to the experimental data and found to pass through the majority of experimental confidence intervals for each temperature. From this large experimental data set, it was evident that cyclodextrin exhibits a broad range in conversion rates over the considered temperatures. At 385 °C, cyclodextrin only achieved ~50% conversion after 200 ms. In contrast, conversion of cyclodextrin was greater than 90% within 100 ms at 505 °C.

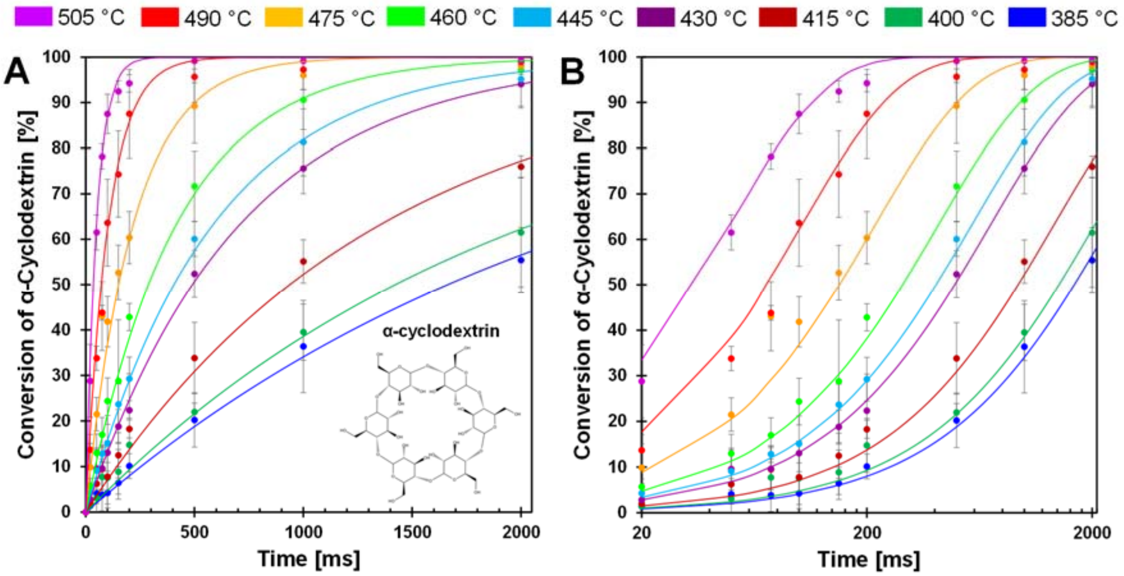

Figure 5.10. PHASR kinetics of α-cyclodextrin. *A. Conversion of α-cyclodextrin at temperatures 385 to 505 °C. B. Conversion of α-cyclodextrin at temperatures 385 to 505 °C with a log time scale. Error bars represent a 90% confidence interval in all data points.*

The selected experimental reaction times (i.e. durations of 20 ms to 2000 ms) were evenly spaced when the cyclodextrin conversion data are viewed on a logarithmic reaction time scale as depicted in Figure 5.10B. By this presentation of the data, the relative rate of conversion of cyclodextrin can be visually observed. For lower temperatures (385 – 460 °C), the first-order kinetic models (blue, dark green, maroon, purple, light blue, and light green lines) are close together. However, the first-order kinetic models above 460 °C (orange, red and purple lines) are much further apart, indicating that the rate of cyclodextrin conversion significantly increased above about 460 °C.

The kinetic transition observed in the cyclodextrin conversion data of Figure 5.10B was further characterized by determining the first-order model kinetic parameter, k [=] s^{-1}, for data sets at each reaction temperature. As shown in Figure 5.11, the logarithm of conversion of cyclodextrin relative to time is linear for first-order systems consistent with the data at each temperature (385-405 °C) in panels 5.11A-I. For each temperature, the first order kinetic parameter, k, was obtained with a least squares fit indicated by the solid line; a 90% confidence interval of k is indicated by shading. Comparison of the parameter range with the experimental data scale bars indicates good agreement in uncertainty.

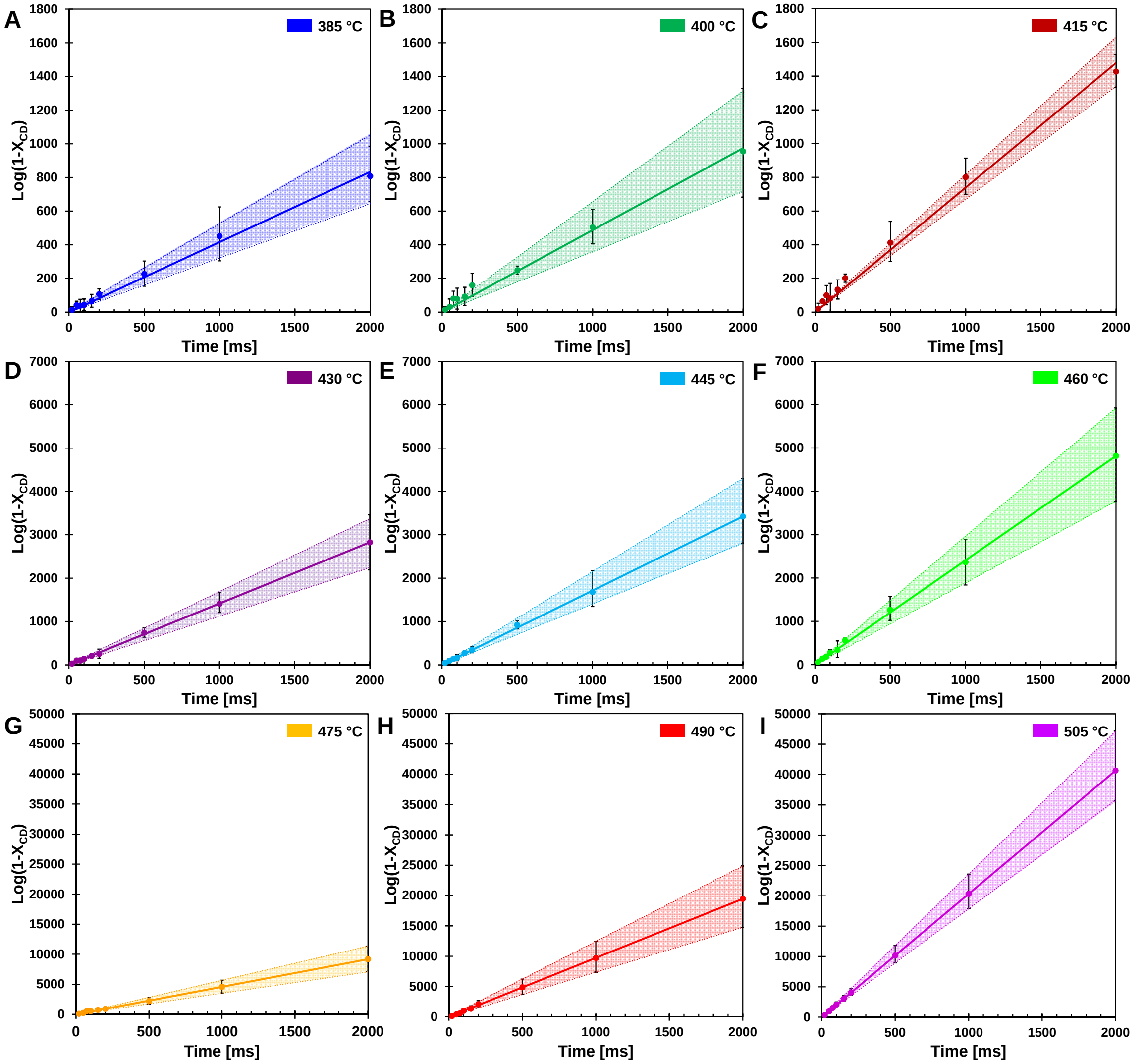

__Figure 5.11. Conversion of α-cyclodextrin with time fit to first-order kinetics.__ Data points represent the conversion of cyclodextrin; error bars represent a 90% confidence interval. Lines represent a first-order rate expression for conversion of cyclodextrin with reaction rate coefficient, k, obtained from a least squares fit; shaded regions represent a 90% confidence interval in the value of k.

The rate coefficients of Figure 5.11 are presented in Figure 5.12 in the Arrhenius form to reveal a distinct transition at 467 °C. Below this transition, the first order kinetic parameters indicated in red exhibit a low activation energy ($E_{a,1} = 23.2 \pm 1.9$ kcal/mol) and low pre-exponential factor ($k_{0,1} = 2.0 \times 10^{7}$ s^{-1}). Above the transition, the first order kinetic are consistent with a high apparent activation energy ($E_{a,2} = 53.7 \pm 1.1$ kcal/mol) and high pre-exponential factor ($k_{0,1}$ = 2.4 x 10^{16} s^{-1}). The two linear kinetic regimes are within the 90% confidence intervals of the nine experimentally-derived kinetic parameters.

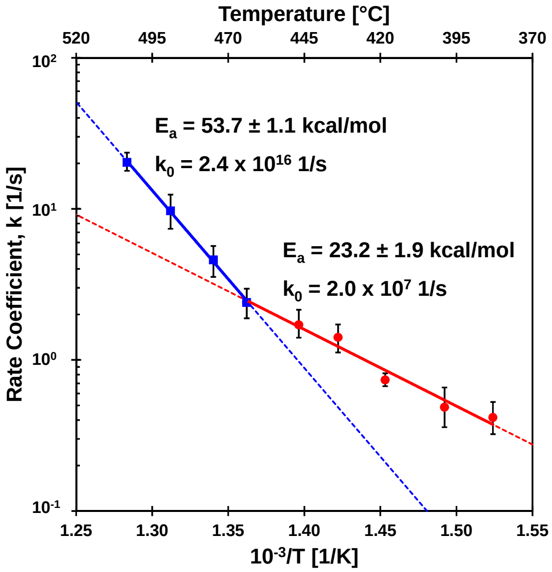

Figure 5.12. First order rate coefficient, k, for α-cyclodextrin conversion with inverse temperature. *The conversion of α-cyclodextrin exhibits a distinct change in kinetic regimes at 467 C, indicative a change in the mechanism of glycosidic bond cleavage. Error in the apparent activation energy represents a 90% confidence interval.*

5.5 Mechanism of Cellulose Fragmentation

The transition observed at 467 °C was previously reported by the differential measurement of initial rates of cyclodextrin conversion. [145] This methodology relied on single data points at each temperature in the interpretation of apparent activation energy at high and low kinetic regimes. In the current work, the measurement of a time-resolved conversion of cyclodextrin allowed the determination of the first-order kinetic parameter, *k*, at each temperature based on several experimental data points (7-9 measurements). Increased data sampling greatly increased the accuracy of measuring the apparent activation energy, particularly at high temperature (475 - 505 °C) where the cyclodextrin reaction is completed in only 100-200 milliseconds. Determination of the kinetic parameters including the pre-exponential factor for both kinetic regimes permits the first molecular interpretation of the kinetics of glycosidic cleavage.

The conversion of cyclodextrin was measured experimentally by determining the quantity of cyclodextrin remaining after the selected thermal pulse duration (reaction time); intermediate and product species were not quantified in these experiments. Conversion can therefore be interpreted as any reaction necessary to initiate the decomposition of cyclodextrin. It follows by a simple interpretation of the two kinetic regimes observed in Figure 5.12 that there exist two mechanisms of glycosidic bond cleavage. A slow mechanism consistent with a low apparent activation energy ($E_a = 23.2 \pm 1.9$ kcal/mol) is the primary cellulose initiation reaction below 467 °C. However, a high activation energy mechanism ($E_a = 53.7 \pm 1.1$ kcal/mol) overtakes this slow mechanism as temperature increases (at 467 °C) and dominates at higher temperatures.

Recent introduction of the PHASR reactor for characterization of time-resolved evolution of volatile organic products from cellulose at temperatures above 400 °C has revealed the existence of two kinetic regimes of cellulose glycosidic cleavage. [145] Since pyrolysis product formation exhibits zero-order rate dependence at low temperature and first-order rate dependence at high temperature, we proposed the mechanism of cellulose decomposition by chain-end cleavage and intra-chain scission, respectively. As depicted in Figure 5.13, PHASR kinetics of cellulose and the surrogate, α-cyclodextrin, indicate that cellulose conversion exhibits a distinct shift in the rate of conversion at 467 °C, a temperature referred to as the “Reactive Melting Point”, or T_{RM}. [145] Below T_{RM}, initiation by glycosidic bond cleavage is slow, and the rate of volatile product (e.g. furans) formation is consistent only with end-chain mechanisms. However, above T_{RM}, cellulose undergoes rapid intra-chain cleavage such that small, intermediate species are rapidly formed as a liquid phase faster than they can decompose and evaporate.

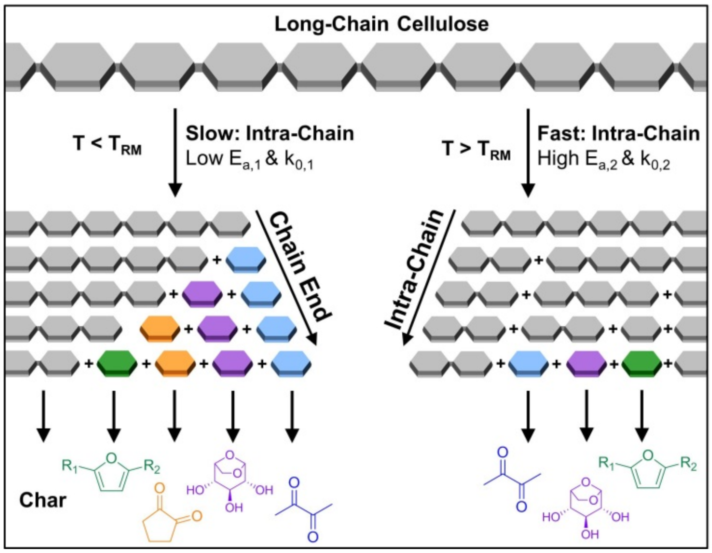

Figure 5.13. Scheme of cellulose glycosidic cleavage near the reactive melting point, T_{RM}. *Cellulose glycosidic bond cleavage is proposed to occur by two competing mechanisms. Below T_{RM} (467 °C), slow intra-chain cleavage produces cellulose fragments which decompose via chain-end mechanisms to volatile products and char. Above T_{RM}, rapid intra-chain cleavage rapidly produces small-molecule intermediates which react to volatile products.*

5.6 Molecular Interpretations of Cleavage Kinetics

The measured kinetic parameters within each regime allow for comparison with computed mechanisms of glycosidic bond cleavage. As listed in Table 5.1, potential mechanisms of glycosidic bond cleavage have been organized within three categories: (i) transglycosylation: reactions #1 to #28, (ii) deglycosylation: reactions #29 to #53, and (iii) hydrolysis: reactions #54 to #60. Transglycosylation was defined as the breaking of the β-1,4 glycosidic bond between glucan monomers combined with the concurrent formation of the bridging C1-C6 ether bond in levoglucosan. Deglycosylation included glycosidic bond cleavage mechanisms that do not form levoglucosan, and hydrolysis combines all catalyzed and uncatalyzed mechanisms that utilize water to break the β-1,4 glycosidic bond into two hydroxyl functional groups.

Table 5.1. Computed kinetics of glycosidic bond cleavage. *Three classes of cellulose glycosidic bond cleavage include transglycosylation to levoglucosan, deglycosylation and hydrolysis.*

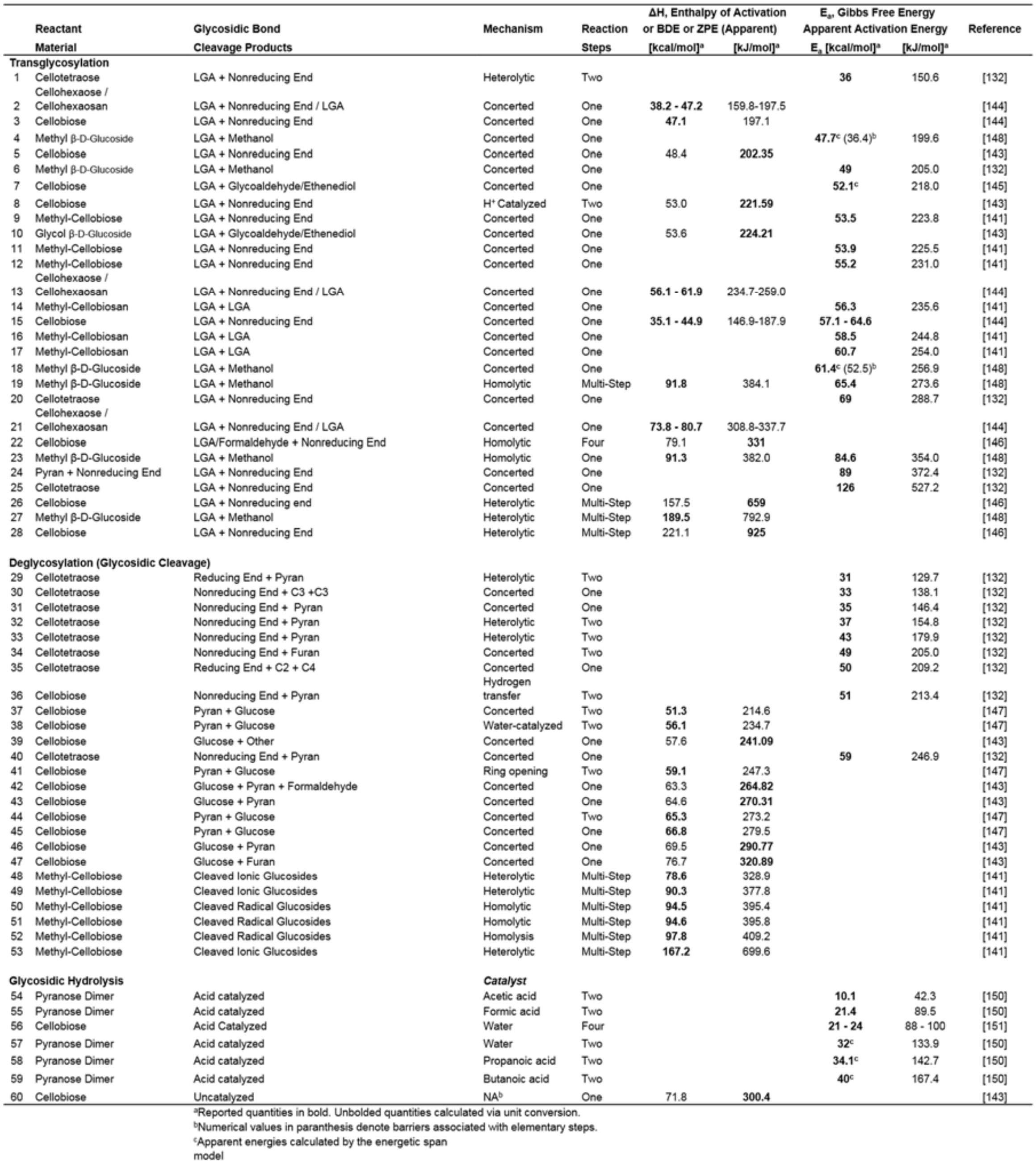

	Reactant Material	Glycosidic Bond Cleavage Products	Mechanism	Reaction Steps	ΔH, Enthalpy of Activation or BDE or ZPE (Apparent)		E_a, Gibbs Free Energy Apparent Activation Energy		Reference
					[kcal/mol]^{a}	[kJ/mol]^{a}	E_a [kcal/mol]^{a}	[kJ/mol]^{a}	
Transglycosylation									
1	Cellotetraose	LGA + Nonreducing End	Heterolytic	Two			**36**	150.6	[132]
2	Cellohexaose / Cellohexaosan	LGA + Nonreducing End / LGA	Concerted	One	**38.2 - 47.2**	159.8-197.5			[144]
3	Cellobiose	LGA + Nonreducing End	Concerted	One	**47.1**	197.1			[144]
4	Methyl β-D-Glucoside	LGA + Methanol	Concerted	One			**47.7**^{c} (36.4)^{b}	199.6	[148]
5	Cellobiose	LGA + Nonreducing End	Concerted	One	48.4	**202.35**			[143]
6	Methyl β-D-Glucoside	LGA + Methanol	Concerted	One			**49**	205.0	[132]
7	Cellobiose	LGA + Glycoaldehyde/Ethenediol	Concerted	One			**52.1**^{c}	218.0	[145]
8	Cellobiose	LGA + Nonreducing End	H^{+} Catalyzed	Two	53.0	**221.59**			[143]
9	Methyl-Cellobiose	LGA + Nonreducing End	Concerted	One			**53.5**	223.8	[141]
10	Glycol β-D-Glucoside	LGA + Glycoaldehyde/Ethenediol	Concerted	One	53.6	**224.21**			[143]
11	Methyl-Cellobiose	LGA + Nonreducing End	Concerted	One			**53.9**	225.5	[141]
12	Methyl-Cellobiose	LGA + Nonreducing End	Concerted	One			**55.2**	231.0	[141]
13	Cellohexaose / Cellohexaosan	LGA + Nonreducing End / LGA	Concerted	One	**56.1 - 61.9**	234.7-259.0			[144]
14	Methyl-Cellobiosan	LGA + LGA	Concerted	One			**56.3**	235.6	[141]
15	Cellobiose	LGA + Nonreducing End	Concerted	One	**35.1 - 44.9**	146.9-187.9	**57.1 - 64.6**		[144]
16	Methyl-Cellobiosan	LGA + LGA	Concerted	One			**58.5**	244.8	[141]
17	Methyl-Cellobiosan	LGA + LGA	Concerted	One			**60.7**	254.0	[141]
18	Methyl β-D-Glucoside	LGA + Methanol	Concerted	One			**61.4**^{c} (52.5)^{b}	256.9	[148]
19	Methyl β-D-Glucoside	LGA + Methanol	Homolytic	Multi-Step	**91.8**	384.1	**65.4**	273.6	[148]
20	Cellotetraose	LGA + Nonreducing End	Concerted	One			**69**	288.7	[132]
21	Cellohexaose / Cellohexaosan	LGA + Nonreducing End / LGA	Concerted	One	**73.8 - 80.7**	308.8-337.7			[144]
22	Cellobiose	LGA/Formaldehyde + Nonreducing End	Homolytic	Four	79.1	**331**			[146]
23	Methyl β-D-Glucoside	LGA + Methanol	Homolytic	One	**91.3**	382.0	**84.6**	354.0	[148]
24	Pyran + Nonreducing End	LGA + Nonreducing End	Concerted	One			**89**	372.4	[132]
25	Cellotetraose	LGA + Nonreducing End	Concerted	One			**126**	527.2	[132]
26	Cellobiose	LGA + Nonreducing end	Heterolytic	Multi-Step	157.5	**659**			[146]
27	Methyl β-D-Glucoside	LGA + Methanol	Heterolytic	Multi-Step	**189.5**	792.9			[148]
28	Cellobiose	LGA + Nonreducing End	Heterolytic	Multi-Step	221.1	**925**			[146]
Deglycosylation (Glycosidic Cleavage)									
29	Cellotetraose	Reducing End + Pyran	Heterolytic	Two			**31**	129.7	[132]
30	Cellotetraose	Nonreducing End + C3 +C3	Concerted	One			**33**	138.1	[132]
31	Cellotetraose	Nonreducing End + Pyran	Concerted	One			**35**	146.4	[132]
32	Cellotetraose	Nonreducing End + Pyran	Heterolytic	Two			**37**	154.8	[132]
33	Cellotetraose	Nonreducing End + Pyran	Heterolytic	Two			**43**	179.9	[132]
34	Cellotetraose	Nonreducing End + Furan	Concerted	Two			**49**	205.0	[132]
35	Cellotetraose	Reducing End + C2 + C4	Concerted	One			**50**	209.2	[132]
36	Cellobiose	Nonreducing End + Pyran	Hydrogen transfer	Two			**51**	213.4	[132]
37	Cellobiose	Pyran + Glucose	Concerted	Two	**51.3**	214.6			[147]
38	Cellobiose	Pyran + Glucose	Water-catalyzed	Two	**56.1**	234.7			[147]
39	Cellobiose	Glucose + Other	Concerted	One	57.6	**241.09**			[143]
40	Cellotetraose	Nonreducing End + Pyran	Concerted	One			**59**	246.9	[132]
41	Cellobiose	Pyran + Glucose	Ring opening	Two	**59.1**	247.3			[147]
42	Cellobiose	Glucose + Pyran + Formaldehyde	Concerted	One	63.3	**264.82**			[143]
43	Cellobiose	Glucose + Pyran	Concerted	One	64.6	**270.31**			[143]
44	Cellobiose	Pyran + Glucose	Concerted	Two	**65.3**	273.2			[147]
45	Cellobiose	Pyran + Glucose	Concerted	One	**66.8**	279.5			[147]
46	Cellobiose	Glucose + Pyran	Concerted	One	69.5	**290.77**			[143]
47	Cellobiose	Glucose + Furan	Concerted	One	76.7	**320.89**			[143]
48	Methyl-Cellobiose	Cleaved Ionic Glucosides	Heterolytic	Multi-Step	**78.6**	328.9			[141]
49	Methyl-Cellobiose	Cleaved Ionic Glucosides	Heterolytic	Multi-Step	**90.3**	377.8			[141]
50	Methyl-Cellobiose	Cleaved Radical Glucosides	Homolytic	Multi-Step	**94.5**	395.4			[141]
51	Methyl-Cellobiose	Cleaved Radical Glucosides	Homolytic	Multi-Step	**94.6**	395.8			[141]
52	Methyl-Cellobiose	Cleaved Radical Glucosides	Homolysis	Multi-Step	**97.8**	409.2			[141]
53	Methyl-Cellobiose	Cleaved Ionic Glucosides	Heterolytic	Multi-Step	**167.2**	699.6			[141]
Glycosidic Hydrolysis			***Catalyst***						
54	Pyranose Dimer	Acid catalyzed	Acetic acid	Two			**10.1**	42.3	[150]
55	Pyranose Dimer	Acid catalyzed	Formic acid	Two			**21.4**	89.5	[150]
56	Cellobiose	Acid Catalyzed	Water	Four			**21 - 24**	88 - 100	[151]
57	Pyranose Dimer	Acid catalyzed	Water	Two			**32**^{c}	133.9	[150]
58	Pyranose Dimer	Acid catalyzed	Propanoic acid	Two			**34.1**^{c}	142.7	[150]
59	Pyranose Dimer	Acid catalyzed	Butanoic acid	Two			**40**^{c}	167.4	[150]
60	Cellobiose	Uncatalyzed	NA^{b}	One	71.8	**300.4**			[143]

[a] Reported quantities in bold. Unbolded quantities calculated via unit conversion.

[b] Numerical values in paranthesis denote barriers associated with elementary steps.

[c] Apparent energies calculated by the energetic span model

Within the three classes of glycosidic bond cleavage, calculation of activation energies by density functional theory (DFT) has included a range of single and multi-step mechanisms (concerted, heterolytic and homolytic) from a variety of surrogate molecules sufficiently small to permit calculation. Common calculation surrogates included cellobiose, [146]–[150] methyl-cellobiose, [144] cellotetraose, [135] cellohexaose/cellohexaosan, [147] and methyl β-D-glucoside. [151] The resulting products of glycosidic bond cleavage were then determined by the considered mechanism; for example, concerted transglycosylation of cellobiose produced glucose (nonreducing end) and levoglucosan (LGA). For each mechanism the calculated apparent activation energy was tabulated as either the apparent Gibbs free energy of activation (in kJ/mol or kcal/mol) or a second category that included the apparent activation enthalpy, bond dissociation energy or zero-point corrected energy (ZPE). For multi-step mechanisms, the apparent activation energy was calculated using the greatest energetic span. [152] While only the Gibbs free energy can be directly compared with experiment, the other categories were included for comparison.

5.6.1 High Temperature Cellulose Initiation

Several proposed mechanisms of glycosidic cleavage exhibit viable apparent activation energy for the high temperature regime of glycosidic bond cleavage ($E_{a,2} = 53.7 \pm 1.1$ kcal/mol). Four variations (reactions #7, #9, #11, and #12 in Table 5.1) [144], [148] of the calculation of transglycosylation via a single concerted mechanism to form levoglucosan; this mechanism is depicted in Figure 5.14A. Concerted transglycosylation undergoes nucleophilic attach of the C1 carbon by the C6 hydroxyl oxygen; the C6 hydroxyl hydrogen is simultaneously transferred to the glycosidic bond oxygen and the glycosidic bond breaks. From the tabulated values of Table 5.1, it is apparent that that free radical mechanisms initiated by homolytic glycosidic cleavage (reactions #19, #22, and #23) [149], [151] are too high in activation energy (E_a = 65.4, 79.4, and 84.6 kcal/mol, respectively) when compared the experimental value in Figure 5.12.

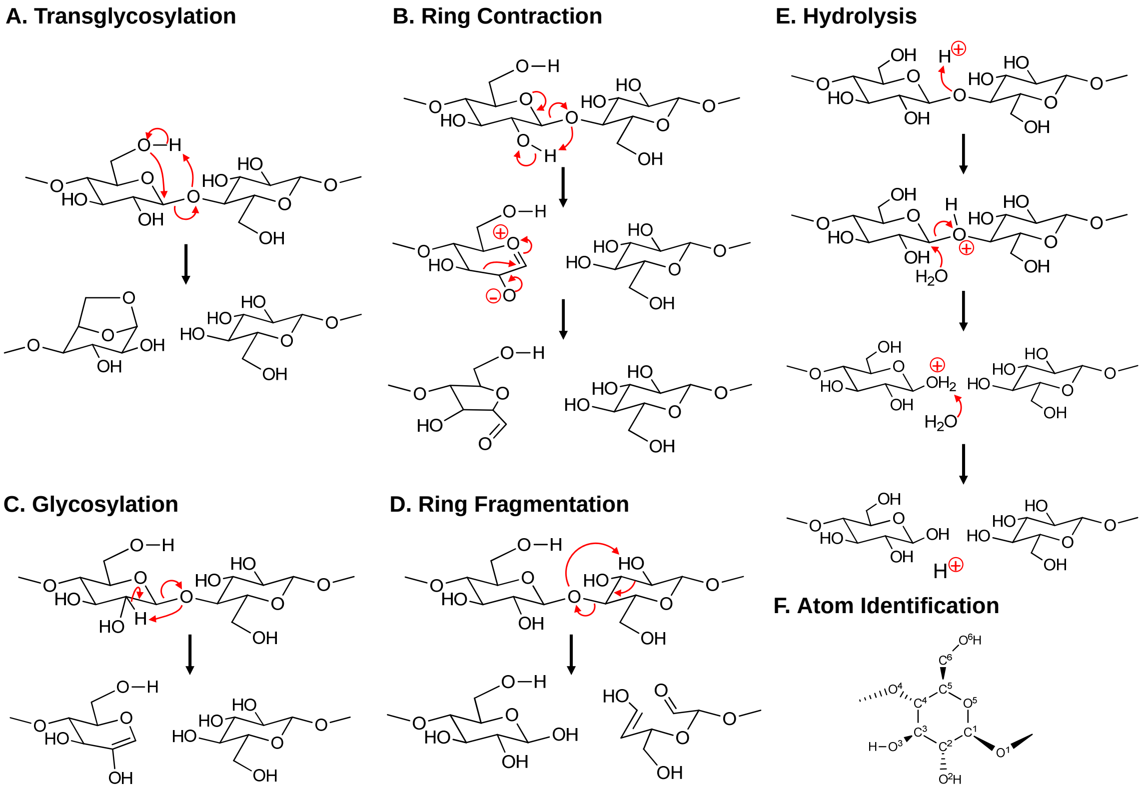

A. Transglycosylation

B. Ring Contraction

E. Hydrolysis

C. Glycosylation

D. Ring Fragmentation

F. Atom Identification

Figure 5.14. Mechanisms of cellulose glycosidic bond cleavage. *A. Glycosidic bond cleavage by concerted transglycosylation. B. Glycosdic bond cleavage by ring contraction to furans. C. Deglycosylation to pyrans. D. Glycosidic bond cleavage by ring fragmentation. E. Acid catalyzed hydrolysis. F. Atom identification of one glucan unit.*

For the high temperature initiation regime (T > 467 °C), three other glycosidic bond cleavage mechanisms were calculated to have viable activation energies when compared with experiment.

- As depicted in Figure 5.14B, depolymerization and ring contraction to a furan precursor of 5-hydroxymethyl-furfural (HMF) occurs by a two-step heterolytic mechanism (reaction #34 in Table 5.1) [135] with apparent activation energy of E_a = 49.0 kcal/mol.

- A second mechanism occurs by single step deglycosylation depicted in Figure 5.14C. By this mechanism (reaction #36 in Table 5.1), [135] the glycosidic oxygen abstracts the C2 hydrogen, thus breaking the glycosidic bond and forming a pyran ring with E_a = 51 kcal/mol.
- A third mechanism occurs by ring fragmentation and simultaneous glycosidic bond fragmentation as depicted in Figure 5.14D. By this mechanism (reaction #35 in Table 5.1), [135] the glycosidic bond oxygen abstracts the C2 hydroxyl hydrogen leading to ring opening and the formation of a C2 and C4 product with apparent activation energy of E_a = 50 kcal/mol.

None of the calculated hydrolysis mechanisms exhibited apparent activation energies sufficiently high to account for the high temperature cellulose initiation reaction.

5.6.2 Low Temperature Cellulose Initiation

The low temperature regime shows a much lower apparent activation energy of glycosidic bond cleavage ($E_{a,1}$ = 23.2 ± 1.9 kcal/mol). Either the concerted transglycosylation or deglycosylation mechanism gives a value comparable to the experimental value. As shown in Table 5.1, the minimal tabulated values for both transglycosylation and deglycosylation mechanisms (reactions #1 and #29 in Table 5.1) [135] are still high in activation energy (E_a = 36 and 31 kcal/mol, respectively) compared to the experimental value in Figure 5.12.

For the low temperature initiation regime (T < 467 °C), only acid-catalyzed hydrolysis mechanism (reaction #55 and # 56 in Table 5.1) [153], [154] exhibit viable activation energies compared to experimental value. As depicted in Figure 5.14E, a double displacement reaction associated with the transfer of the proton from the acid residue onto the glycosidic oxygen in the first reaction, and the transfer of the hydrogen from the water to the nucleophilic acid residue in the second reaction by a two-step hydrolysis mechanism (reaction #55 in Table 5.1) [153] with apparent activation energy of $E_a = 21.4$ kcal/mol. Both transition states in the reaction mechanism are concerted reactions with four individual bonds being created or destroyed in each step. The acid sources for proton could be small light oxygenates produced from pyrolysis such as acetic acid and formic acid.

5.6.3 General Interpretation of Kinetics

As stated previously for mechanisms of glycosidic bond cleavage, the apparent activation energies of Figure 5.12 cannot be readily interpreted without the development of a complex kinetic model. There have been several lumped kinetic models developed to simplify the overall chemistry to a single reaction or a few reactions such as the direct mechanism proposed by Broido [112] or intermediate-controlled model first proposed by Shafizadeh, [113] as shown in Figure 5.15. Interpretation of a complex depolymerization mechanism as a simple reaction (e.g. A → B) oversimplifies the chemistry and leads to misinterpretation of the measured data. For example, the apparent energies of Figure 5.12 are both very low ($E_{a,1} = 23.2 \pm 1.9$ kcal/mol) and very high ($E_{a,2} = 53.7 \pm 1.1$ kcal/mol). For the low activation energy, interpreted as a simple (A → B) mechanism would convert almost instantaneously with any reasonable pre-exponential factor. However, the high activation energy would require a pre-exponential factor that is really high (>10^{16} s^{-1}) for a single reaction to achieve a reasonable rate of conversion.

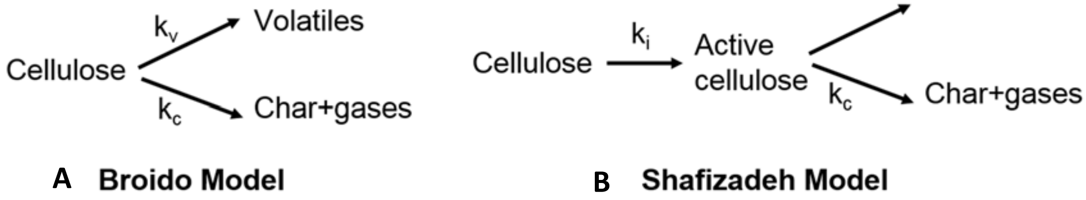

Figure 5.15. Two proposed kinetic models for cellulose pyrolysis. *(a) Kinetic model proposed by Broido and Nelson,* [112] *(b) by Bradbury, Sakai, and Shafizadeh (the Broido-Shafizadeh Model).* [113]

It has been demonstrated many times that polymer decomposition requires numerous steps for either homolytic or heterolytic chemistry resulting in complex rate expressions comprised of numerous terms. Thus, apparent activation energies can result from a combination of initiation, propagation, and termination steps, [155] which are lower or higher than those of any individual steps. Alternatively, the rate expression for a polymer reaction can reduce to just the activation energy of the initiation step. Broadbelt and co-workers [141] have stated that an activation energy for a simplified rate expression corresponding to a simple lumped model of cellulose conversion (e.g. A → B) must be in the range of ~50 kcal/mol to achieve the appropriate rate of conversion, which they estimated as a cellulose reaction completing within a few seconds at 500 °C. This matches the high activation energy in the range observed for cyclodextrin/cellulose decomposition above T_{RM}. Thus, while the tabulated energetics of Table 5.1 are potentially viable for certain reaction mechanisms and associated models, it is impossible to evaluate the apparent activation energies of Figure 5.12 at first glance without a complex kinetic model.

5.7 Conclusions

By employing PHASR reactor and α-cyclodextrin as cellulose surrogate, fragmentation kinetics of cellulose conversion were measured at 385 – 505 °C to elucidate the thermal decomposition mechanisms of liquid intermediate formation. Cyclodextrin thin film conversion rates were measured using an innovative device called Pulsed-Heated Analysis of Solid Reactions (PHASR) reactor for cellulose liquid phase analysis. The initial breakdown kinetics of cellulose exhibit a distinct transition at 467 °C, which is interpreted as a 'reactive melting point' (T_{RM}), with two kinetic regimes: a low activation energy for glycosidic bond cleavage ($E_{a,1}$ = 23.2 ± 1.9 kcal/mol) associated with chain-end cleavage mechanism ($T < 467$ °C) and a high activation energy for glycosidic bond cleavage ($E_{a,2}$ = 53.7 ± 1.1 kcal/mol) consistent with intra-chain scission ($T > 467$ °C). The experimental apparent activation energies were interpreted by comparing with computational literature values with three potential mechanisms of transglycosylation, deglycosylation, and hydrolysis.

Chapter 6 Calcium Catalyzed Scission of Cellulose Glycosidic Bond

6.1 Introduction and Sample Preparation

In the Chapter 4, the catalytic effect of alkaline earth metals on cellulose pyrolysis was investigated by doping cellulose sample with calcium or magnesium ions. Significant product distribution changes were observed by comparing powder and thin-film pyrolysis, proving the effectiveness of metal ions as catalysts on cellulose decomposition. Therefore, after getting an initial mechanism understanding of cellulose fragmentation from Chapter 5, my work continues on adding calcium ions into the cyclodextrin samples. Through quantitatively comparing the relative change in reaction rates and activation energies, it provides information to discover the catalytic mechanism of alkaline earth metals on cellulose initiation reaction.

The Ca^{2+}/cyclodextrin samples were prepared the same way as described in Chapter 5 through solvent deposition and drying on heating elements. The only difference is adding extra calcium nitrate salts into the 1.0 wt% α-cyclodextrin solution. Then the mixed solution was pipetted onto the center of the heating element to dry. To be consistent with the calcium concentrations in Chapter 4, Ca loadings into the cyclodextrin samples were chosen to be from 0.1 to 0.5 mmol/g cyclodextrin which represents the concentration of natural inorganic ions within the biomass. Additionally, to compared with pure cyclodextrin pyrolysis, the conversion of Ca-catalyzed cyclodextrin was measured for a range of temperatures (370 – 430 °C) and pulse lengths (20 - 2000 ms) same as in the previous chapter.

6.2 Ca^{2+} Catalyzed Cyclodextrin Conversion Kinetics

As shown in Figure 6.1, for each reaction temperature, the single data point was comprised of at least three independent experimental trials; error bats associated with each point represent a 90% confidence interval. From the appearance of all the panels 6.1A-E, it is evident that Ca catalyzed cyclodextrin conversion also exhibit first order kinetics. For the same Ca concentration, with reaction temperature increase, the reaction rate of cyclodextrin conversion become faster as expected. For instance, cyclodextrin with 0.5 mmol Ca/g cyclodextrin needs more than 2000 ms to complete the conversion at 370 °C (Figure 6.1A, red line), while it only takes less than 200 ms to reach fully converted at 430 °C (Figure 6.1E, red line). In addition, for the same reaction temperature, increasing Ca loading dramatically increased reaction rate with much shorter time to complete the conversion. Take cyclodextrin conversion at 400 °C as an example (Figure 6.1C), pure cyclodextrin conversion was only about 40% at reaction time of 1000 ms (purple line). However, with 0.5 mmol Ca/g cyclodextrin added into the sample, the conversion of cyclodextrin was completed by the time of 1000 ms (Figure 6.1C, red line) indicating the fast catalytic effect of calcium ions on glycosidic bond cleavage.

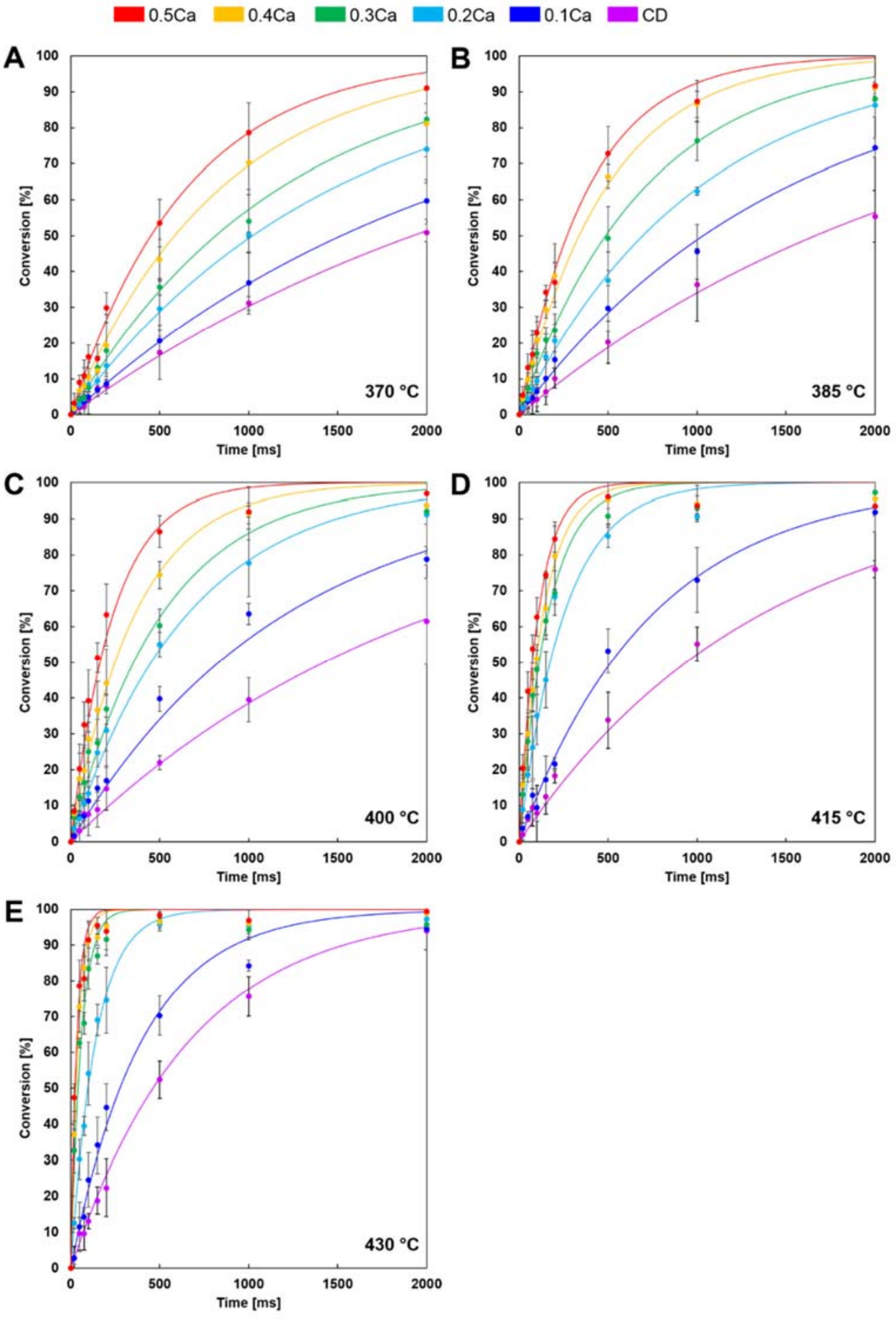

Figure 6.1. PHASR kinetics of Ca-catalyzed α-cyclodextrin. *A. Conversion of α-cyclodextrin at temperatures 370 °C with varied Ca concentrations from 0.1 to 0.5 mmol/g cyclodextrin. B. Conversion of α-cyclodextrin at temperatures 385 °C. C. Conversion of α-cyclodextrin at temperatures 400 °C. D. Conversion of α-cyclodextrin at temperatures 415 °C. E. Conversion of α-cyclodextrin at temperatures 430. Error bars represent a 90% confidence interval in all data points.*

Of particular note, for lower temperatures region (370 - 385 °C, Figure 6.1A-B), the first-order kinetic models are evenly increasing, close to each other. However, for higher temperatures above 400 °C (Figure 6.1C-E), the first-order kinetic models are much broader separated from each other, implying significant increase due to the addition of Ca ions. One problem is that for the higher temperatures from 415 to 430 °C, the first-order kinetic models at high Ca concentrations above 0.3 mmol/g cyclodextrin almost overlaid together, indicating the measurement of these reactions may exceed the PHASR reactor's limit. Thus, the conversion results under these conditions were untrusted and the calculation for reaction rate coefficient, k, didn't account for Ca concentrations above 0.3 mmol/g cyclodextrin at high temperatures.

From the conversion of cyclodextrin, we could determine the first-order reaction rate coefficient, $k_{apparent}$ [=] s^{-1}, for data sets at each reaction temperature and Ca concentration. One interesting finding is that the reaction rate coefficient at each reaction temperature exhibits second order dependence on Ca concentration, as depicted in Figure 6.2. The first-order kinetic parameter, $k_{apparent}$, is linear to the square of Ca concentration in panel 6.2A-E for all the reaction temperatures. Based on this relationship, a least square fit gives the actual reaction rate coefficient, k', to present in the catalytic Arrhenius plot.

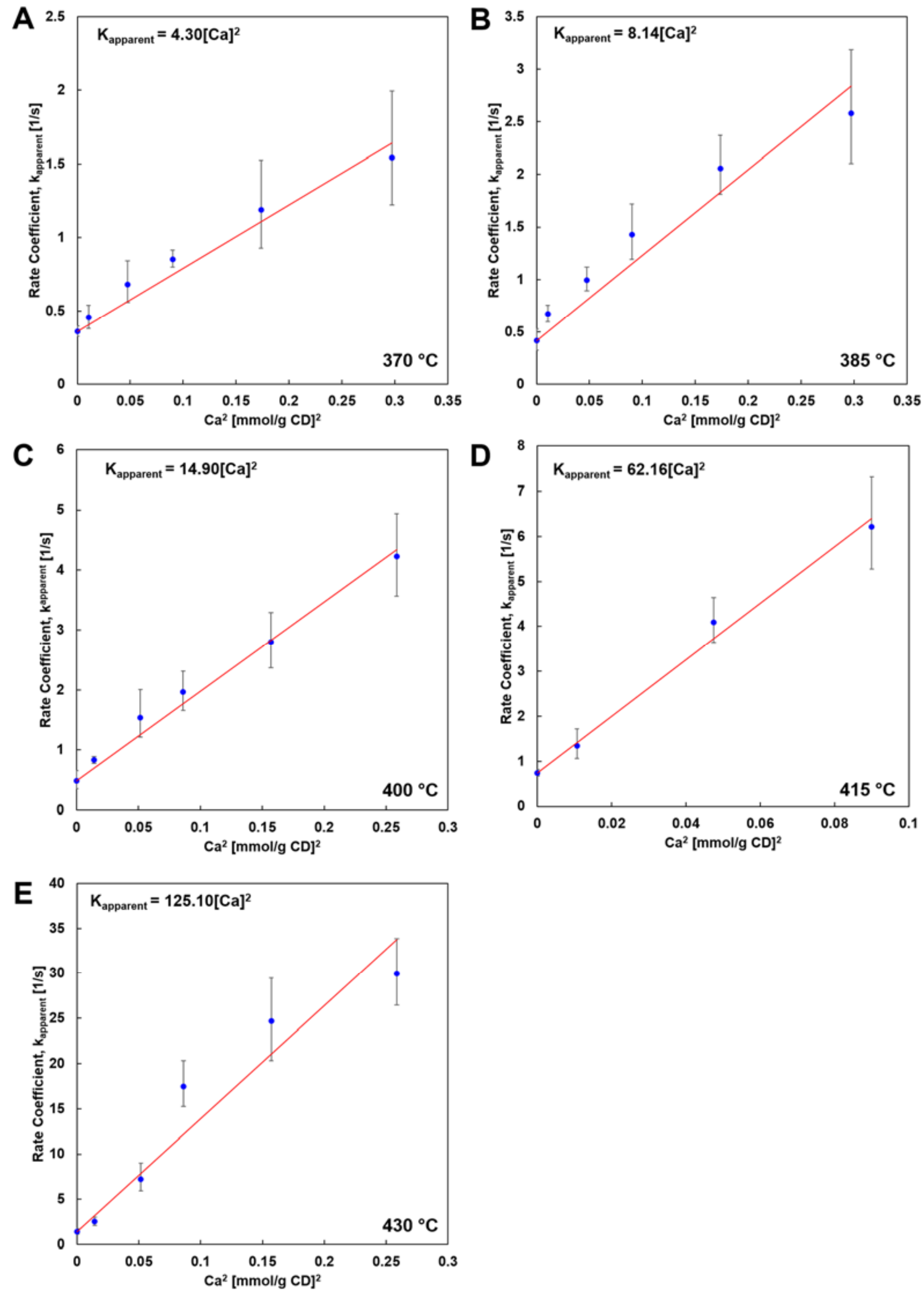

Figure 6.2. First-order kinetic parameter, $k_{apparent}$, versus Ca concentration. *A. First-order reaction rate coefficient, $k_{apparent}$, is linear to the square of Ca concentration, exhibits second-order dependence at 370 °C. B. Reaction rate coefficient versus Ca concentration at 385 °C. C. Reaction rate coefficient versus Ca concentration at 400 °C. D. Reaction rate coefficient versus Ca concentration at 415 °C. E. Reaction rate coefficient versus Ca concentration at 430 °C. Error bars represent a 90% confidence interval.*

The actual rate coefficients fitted from Figure 6.2 are presented in Figure 6.3 to reveal the catalytic activation energy of cyclodextrin decomposition. The Arrhenius plot (Figure 6.3) shows a high apparent activation energy (E_a = 50.5 ± 4.6 kcal/mol) and high pre-exponential factor (A = 5.7 x 10^{17} s^{-1}) for Ca-catalyzed cyclodextrin conversion. The catalytic activation energy exhibits a similar value to that of pure cyclodextrin decomposition in high temperature region, as shown in Figure 5.12. However, the reaction temperature range for Ca^{2+}/cyclodextrin samples are from 370 to 430 °C, which is lower than the T_{RM} of 467 °C in the low temperature region. Combined with cellulose fragmentation mechanisms stated before, this variation in activation energies may indicate that even at low reaction temperatures, the presence of Ca ions catalyzed cellulose decomposition by changing the fragmentation mechanism from chain-end cleavage to intra-chain scission. Therefore, the activation energy for Ca-catalyzed cyclodextrin conversion below T_{RM} increased to the value of pure cyclodextrin conversion above T_{RM}.

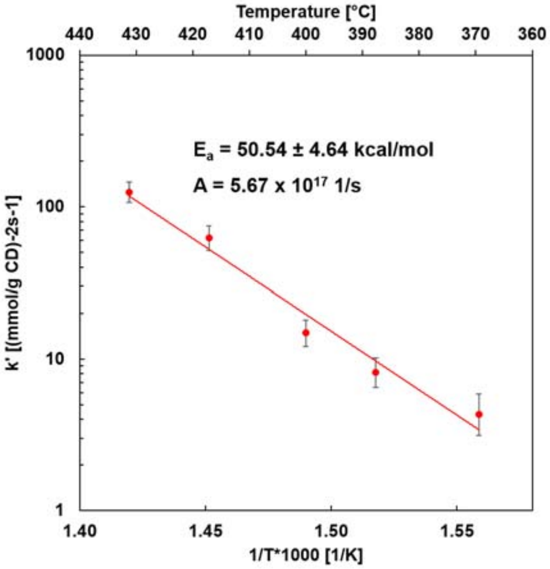

Figure 6.3. First order rate coefficient, k', for Ca-catalyzed α-cyclodextrin conversion with inverse temperature. *Error in the apparent activation energy represents a 90% confidence interval.*

6.3 Conclusions

Adding Ca ions into the cyclodextrin sample enables to quantify the catalytic kinetics of cyclodextrin conversion in the presence of alkaline earth metals. The addition of Ca ions dramatically increased reaction rate with activation energy ($E_a = 50.5 \pm 4.6$ kcal/mol) similar to the value of cyclodextrin decomposition at high temperatures. This energetics change probably indicate that Ca ions catalyzed cellulose initiation with decomposition mechanism shifted from chain-end scission to intra-chain cleavage. Of particular note, the catalyzed rate coefficient exhibits second order dependence on Ca concentration.

6.4 Future Direction

Biomass pyrolysis represents a renewable thermochemical route to transportation fuels and commodity chemicals, which has significant advantages over biochemical enzymatic biofuels production such as faster conversion rates and feedstock flexibility. Despite the wide study of catalysts for upgrading bio-oil, fundamental understanding of the natural inorganic constituents within biomass on the pyrolysis chemistry is limited. Understanding the molecular level reaction mechanisms of these inorganics affecting biofuel quality and yield is crucial in optimizing industrial pyrolysis reactors.

The technique of capturing kinetics of pyrolysis chemistry is still under development. In this thesis, a new experimental apparatus named of PHASR reactor was employed which is specifically tailored for pyrolysis chemistry. It is shown to be successful in measuring reaction rates for cellulose conversion and pyrolysis products formation. This is significant improvement over the reported values in literature as their kinetics was measured in the timescale of second. [108], [156] Beyond the work done in this thesis, future work is needed to understand the complex reaction environment not only within the liquid intermediate, but also within the gas phase.

As speculated in Chapter 4, alkaline earth metals are shown to catalyse cellulose pyrolysis on both primary and secondary pathways. After the study of cellulose initiation breakdown kinetics, one direction is continuing the investigation of the catalytic role of alkaline earth metals on the formation of volatile organics in gas phase and other intermediate liquid compounds. Also, it is anticipated that the loading of natural inorganic catalysts could significantly contribute to pyrolysis product yield. The other direction could study the catalytic role of other inorganic ions such as alkali metals of Na^+ and K^+ to compare with alkaline earth metals to reveal the influence of valence on their catalytic effect.

Although the PHASR reactor is effective for capturing millisecond kinetic data, there are still some issues to be addressed in the future. Disparity in total carbon balance of the system is one of the major concerns. Especially, the yield of major pyrolysis product levoglucosan (LGA) is inconsistent with the theoretical calculations and previously reported values. [14], [88] The incomplete recovery of LGA may result in the failure of measuring all the LGA related pyrolysis experiments. This problem may be due to the condensation of LGA after the reaction hot zone and before flowing into the GC column. We heated the outlet of the micro-reactor up to only 260 °C to avoid melting the Teflon gasket, which is much lower than the boiling point of LGA (384 °C). [147] Therefore, future effort needs to be put on either improving the heating technique at the reactor outlet or modifying the configuration of heating block to prevent LGA condensation.

Mechanism of cellulose pyrolysis chemistry as well as the effect of natural inorganic catalysts on cellulose pyrolysis has been a subject of debate in the literature for decades. [93], [94], [96], [100], [101], [103]–[105] Measurement of the kinetics of pyrolysis products can be used as an effective tool to validate or revoke the long-debated contradictory mechanisms of cellulose pyrolysis. Furthermore, except the focus on cellulose pyrolysis in this thesis, the other two important biomass components of hemicellulose and lignin pyrolysis chemistry remains to be discovered.

Bibliography

[1] U.S. Energy Information Administration, What are the major sources and users of energy in the United States? 2015, http://www.eia.gov/energy_in_brief/article/major_energy_sources_and_users.cfm.

[2] P. McKendry, Energy production from biomass (part 2): Conversion technologies," *Bioresour. Technol.*, **2002**, 83, 47–54.

[3] H. B. Goyal, D. Seal, and R. C. Saxena, Bio-fuels from thermochemical conversion of renewable resources: A review, *Renew. Sustain. Energy Rev.*, **2008**, 12, 504–517.

[4] A. Demirbaş, Biomass resource facilities and biomass conversion processing for fuels and chemicals, *Energy Convers. Manag.*, **2001**, 42, 1357–1378.

[5] N. Kobyashi, Y. Itaya, G. Piao, S. Mori, M. Kondo, M. Hamai, and M. Yamaguchi, The behavior of flue gas from RDF combustion in a fluidized bed, *Powder Technol.*, **2005**, 151, 87–95.

[6] J. W. Bohlig and D. Bai, A Process for Cogasifying and Cofiring Engineered Fuel with Coal, U.S. Patent WO2012145755, October 16, 2012.

[7] J. W. Bohlig and D. Bai, Engineered Fuel Feed Stock, U.S. Patent US8157874, April 17, 2012.

[8] D. Bai, Systems and Methods for Producing Engineered Fuel Feed Stocks from Waste Material, U.S. Patent US8579997, November 12, 2013.

[9] H. Manninen, Co-Combustion of Refuse-Derived and Packaging-Derived Fuels (Rdf and Pdf) With Conventional Fuels, *Waste Management & Research*, **1997**, 15, 137–147.

[10] O. Boutin, M. Ferrer, and J. Lédé, Radiant flash pyrolysis of cellulose—Evidence for the formation of short life time intermediate liquid species, *J. Anal. Appl. Pyrolysis*, **1998**, 47, 13–31.

[11] Z. Wang, A. G. McDonald, R. J. M. Westerhof, S. R. a Kersten, C. M. Cuba-Torres, S. Ha, B. Pecha, and M. Garcia-Perez, Effect of cellulose crystallinity on the formation of a liquid intermediate and on product distribution during pyrolysis, *J. Anal. Appl. Pyrolysis*, **2013**, 100, 56–66.

[12] A. R. Teixeira, K. G. Mooney, J. S. Kruger, C. L. Williams, W. J. Suszynski, L. D. Schmidt, D. P. Schmidt, and P. J. Dauenhauer, Aerosol generation by reactive boiling ejection of molten cellulose, *Energy Environ. Sci.*, **2011**, 4, 4306-4321.

[13] G. Chimique, J. P. Diebold, G. V. C. Peacocke, and J. Piskorz, The nature and properties of intermediate and unvaporized biomass pyrolysis materials. *Developments in Thermochemical Biomass Conversion.* Springer Netherlands, 1997, 27–42.

[14] M. S. Mettler, S. H. Mushrif, A. D. Paulsen, A. D. Javadekar, D. G. Vlachos, and P. J. Dauenhauer, Revealing pyrolysis chemistry for biofuels production: Conversion of cellulose to furans and small oxygenates, *Energy Environ. Sci.*, **2012**, 5, 5414-5424.

[15] BP Statistical Review of World Energy, BP: London, 2013.

[16] U.S. Energy Information Administration, International Energy Outlook 2013, Report No. DOE/EIA-0484(2013), Washington DC, 2013.

[17] B. K. Gullett, B. Ghorishi, R. Keeney, and F.E. Huggins, Mercuric chloride capture by alkaline sorbents. In *Proceddings of the 93rd Air and Waste Management Association Conference*, Salt Lake City, UT, June 18-22, 2000.

[18] U.S. Environmental Protection Agency, National Ambient Air Quality Standards (NAAQS), http://www. epa.gov/air/criteria.html.

[19] Flue Gas Analysis in Industry, Testo:Sparta, NJ, 2010, Chapter 3.

[20] U.S. Environmental Protection Agency, Clean Air Act, http://www.epa.gov/air/caa/.

[21] H. Wu, P. Glarborg, F. J. Frandsen, K. Dam-Johansen, P. A. Jensen, and B. Sander, Co-combustion of pulverized coal and solid recovered fuel in an entrained flow reactor - General combustion and ash behaviour, *Fuel*, **2011**, 90, 1980–1991.

[22] D. Surroop and A. Juggurnath, Investigating the Energy Potential from Co-firing Coal with Municipal Solid Waste, *Univ. Mauritius Res. J.*, **2011**, 17, 109–123.

[23] H. Cheng and Y. Hu, Municipal solid waste (MSW) as a renewable source of energy: Current and future practices in China, *Bioresour. Technol.*, **2010**, 101, 3816–3824.

[24] F. D. Hernandez-Atonal, C. Ryu, V. N. Sharifi, and J. Swithenbank, Combustion of refuse-derived fuel in a fluidised bed, *Chem. Eng. Sci.*, **2007**, 62, 627–635.

[25] R. Marsh, A. J. Griffiths, K. P. Williams, and S. J. Wilcox, Physical and thermal properties of extruded refuse derived fuel, *Fuel Process. Technol.*, **2007**, 88, 701–706.

[26] E. Ferrer, M. Aho, J. Silvennoinen, and R. V. Nurminen, Fluidized bed combustion of refuse-derived fuel in presence of protective coal ash, *Fuel Process. Technol.*, **2005**, 87, 33–44.

[27] C.-S. Chyang, Y.-L. Han, L.-W. Wu, H.-P. Wan, H.-T. Lee, and Y.-H. Chang, An investigation on pollutant emissions from co-firing of RDF and coal., *Waste Manag.*, 2010, 30, 1334–1340.

[28] X. Wei, Y. Wang, D. Liu, H. Sheng, W. Tian, and Y. Xiao, Release of Sulfur and Chlorine during Cofiring RDF and Coal in an Internally Circulating Fluidized Bed, *Energy & Fuels*, **2009**, 23, 1390–1397.

[29] J. Zhang, K. Liu, W. P. Pan, J. T. Riley, and Y. Xu, Characterization of ash deposition during co-combustion of coal with refuse-derived fuels in a pilot FBC facility, *Energy and Fuels*, In *Proceedings of the 17th International Fluidized Bed Combustion Conference*, Jacksonville, FL, May 18-21, 2003.

[30] B. K. Gullett, K. Raghunathan, and J. E. Dunn, The effect of cofiring high-sulfur coal with municipal waste on formation of polychlorinated dibenzodioxin and polychlorinated dibenzofuran, *Environ. Eng. Sci.*, **1998**, 15, 59–70.

[31] G. A. Norton and A. D. Levine, Cocombustion of refuse-derived fuel and coal-A review of selected emissions, *Environ. Sci. technol.*, **1989**, 23, 774-783.

[32] H. P. Wan, Y. H. Chang, W. C. Chien, H. T. Lee, and C. C. Huang, Emissions during co-firing of RDF-5 with bituminous coal, paper sludge and waste tires in a commercial circulating fluidized bed co-generation boiler, *Fuel*, **2008**, 87, 761–767.

[33] J. Silvennoinen, J. Rpoop, R. V. Nurminen, M. Aho, P. Vainikka, and E. Ferrer, Co-combustion of coal with REF and biomass-prevention of chloine deposition by using coal ash alkali adsorption ability, In *Proceedings of the 18th International Conference on Fluidized Bed Combustion*, Toronto, ON, May 22-25, 2005.

[34] J. F. Cheng, H. C. Zeng, Z. H. Zhang, and M. H. Xu, The effects of solid absorbents on the emission of trace elements, SO_2, and NO_x during coal combustion, *Int. J. Energy Res.*, **2001**, 25, 1043–1052.

[35] J. Cheng, J. Zhou, J. Liu, Z. Zhou, Z. Huang, X. Cao, X. Zhao, and K. Cen, Sulfur removal at high temperature during coal combustion in furnaces: A review, *Prog. Energy Combust. Sci.*, **2003**, 29, 381–405.

[36] E. J. Badin and G. C. Frazier, Sorbents for fluidized-bed combustion, *Environ. Sci. Technol.*, **1985**, 19, 894–901.

[37] Y. Liu, T. M. Bisson, H. Yang, and Z. Xu, Recent developments in novel sorbents for flue gas clean up, *Fuel Process. Technol.*, **2010**, 91, 1175–1197.

[38] L. A. Fenouil and S. Lynn, Kinetics and structural studies of calcium-based sorbents for high-temperature coal-gas desulfurization, *Fuel Sci. technol. Int.*, **1994**, 14, 537-557.

[39] H. Raclavska, D. Matysek, K. Raclavsky, and D. Juchelkova, Geochemistry of fly ash from desulphurisation process performed by sodium bicarbonate, *Fuel Process. Technol.*, **2010**, 91, 150–157.

[40] M. J. Pilat and J. M. Wilder, Pilot scale SO_2 control by dry sodium bicarbonate injection and an electrostatic precipitator, *Environ. Prog.*, **2007**, 26, 263-270.

[41] C. Wu, S. J. Khang, T. C. Keener, and S. K. Lee, A model for dry sodium bicarbonate duct injection flue gas desulfurization, *Adv. Environ. Res.*, **2004**, 8, 655–666.

[42] K. E. Daugherty, *An identification of potential binding agents for densified fuel preparation from municipal solid waste: Phase I, final report*, Report No. DE88007698, Argonne National Laboratory: Lemont, IL,1986.

[43] O. Ohlsson, *Results of combustion and emissions testing when co-firing blends of biner-enhanced densified refuse-derived fuel (b-dRDF) pellets and coal in a 440 MWe cyclone fired combustor, Vol. 1, test methodology and results*, Report No. DE94000283, Argonne National Laboratory: Lemont, IL, 1994.

[44] K. Liu, W. P. Pan, and J. T. Riley, A study of chlorine behavior in a simulated fluidized bed combustion system, *Fuel*, **2000**, 79, 1115–1124.

[45] F. Okasha, Enhancing sulphur self-retention by building-in CaO in straw-bitumen pellets, *Fuel Process. Technol.*, **2007**, 88, 401–408.

[46] H. G. Stenger and E. C. Meyer, Laboratory-scale coal combustor for flue gas emission studies, *Energy & Fuels*, **1992**, 6, 277–286.

[47] S. Li, S. Deng, A. Wu, and W. P. Pan, Impact of the addition of chicken litter on mercury speciation and emissions from coal combustion in a laboratory-scale fluidized bed combustor, *Energy and Fuels*, **2008**, 22, 2236–2240.

[48] Y. Cao, H. Zhou, J. Fan, H. Zhao, T. Zhou, P. Hack, C.-C. Chan, J.-C. Liou, and W. Pan, Mercury Emissions during Cofiring of Sub-bituminous Coal and Biomass (Chicken Waste , Wood , Coffee Residue , and Tobacco Stalk) in a Laboratory-Scale Fluidized Bed Combustor, *Environ. Sci. Technol.*, **2008**, 42, 9378–9384.

[49] C. R. Milne, G. D. Silcox, D. W. Pershing, and D. A. Kirchgessner, Calcination and sintering models for application to high-temperature, short-time sulfation of calcium-based sorbents, *Ind. Eng. Chem. Res.*, **1990**, 29, 139–149.

[50] W. Jozewicz and D. A. Kirchgessner, Calcination of Calcium Hydroxide Sorbent in the Presence of SO_2 and Its Effect on Reactivity, In *Emerging Technologies in Hazardous Waste Mangaement II*, ACS Symposium Series, 1991, 468, Chapter 4, 55-64,.

[51] R. H. Borgwardt, Calcium oxide sintering in atmospheres containing water and carbon dioxide, *Ind. Eng. Chem. Res.*, **1989**, 28, 493–500.

[52] C. Guldur, G. Dogu, and T. Dogu, Kinetics of trona sulfur dioxide reaction, *Chem. Eng. Process.*, **2001**, 40, 13-18.

[53] K. W. Ragland and K. W. Bryden, *Combustion Engineering*, Second Edition, CRC press: New York, 2011, 108-115.

[54] B. Courtemanche and Y. Levendisaf, A laboratory study on the NO, NO_2, SO_2, CO and CO_2 emissions from the combustion of pulverized coal , municipal waste plastics and tires, *Fuel*, **1998**, 77, 183–196.

[55] D. Liu, C. Zhang, Y. Mi, B. Shen, and B. Feng, Reduction of N_2O and NO emissions by co-combustion of coal and biomass, *J. Inst. Energy*, **2002**, 75, 81-84.

[56] J. E. Johnsson, A kinetic model for NO_x formation in fluidized bed combustion. In *Proceedings of the 11th International Conference on Fluidized Bed Combustion*, Montreal, QB, 1989.

[57] T. Hunt and J. T. Hanley, *Integrated Dry NO_x/SO_2 Emissions Control System Final Report, Volume 2: Project Performance and Economics*, U.S. Department of Energy: Washington, DC, 1999.

[58] J. Wang, Y. Wu, and E. J. Anthony, Reactions of solid $CaSO_4$ and Na_2CO_3 and formation of sodium carbonate sulfate double salts, *Thermochim. Acta*, **2007**, 459, 121–124.

[59] Municipal Solid Waste Generation, Recycling, and Disposal in the United States: Facts and Figures for 2011, 2011. http://www.epa.gov/solidwaste/nonhaz/municipal/msw99.html.

[60] T. Michaels, The 2010 ERC Directory of Waste-to-Energy Plants, 2010. http://www.energyrecoverycouncil.org/userfiles/file/ERC_2010_Directory.pdf

[61] M. Sami, K. Annamalai, and M. Wooldridge, Co-firing of coal and biomass fuel blends, *Prog. Energy Combust. Sci.*, **2001**, 27, 171–214.

[62] T. Kupka, M. Mancini, M. Irmer, and R. Weber, Investigation of ash deposit formation during co-firing of coal with sewage sludge, saw-dust and refuse derived fuel, *Fuel*, **2008**, 87, 2824–2837.

[63] L. Rigamonti, M. Grosso, and L. Biganzoli, Environmental Assessment of Refuse-Derived Fuel Co-Combustion in a Coal-Fired Power Plant, *J. Ind. Ecol.*, **2012**, 16, 748–760.

[64] G. Piao, S. Aono, M. Kondoh, R. Yamazaki, and S. Mori, Combustion test of refuse derived fuel in a fluidized bed, *Waste Manag.*, **2000**, 20, 443–447.

[65] H. Saito, S. Kosugi, and K. Sato, The revolving-type fluidized-bed incinerator: Its basic performance in MSW combustion, *Waste Manag. Res.*, **1988**, 6, 261–270.

[66] K. Tuppurainen, I. Halonen, P. Ruokojärvi, J. Tarhanen, and J. Ruuskanen, Formation of PCDDs and PCDFs in municipal waste incineration and its inhibition mechanisms: A review, *Chemosphere*, **1998**, 36, 1493–1511.

[67] N. Orbey, G. Dogu, and T. Dogu, Breakthrough analysis of noncatalytic solid-gas reactions: Reaction of SO_2 with calcined limestone, *Can. J. Chem. Eng.*, **1982**, 60, 314–318.

[68] M. R. Stouffer and H. Yoon, An investigation of CaO sulfation mechanisms in boiler sorbent injection, *AIChE J.*, **1989**, 35, 1253–1262.

[69] G. Hu, K. Damjohansen, S. Wedel, and J. Peterhansen, Review of the direct sulfation reaction of limestone, *Prog. Energy Combust. Sci.*, **2006**, 32, 386–407.

[70] T. Hlincik and P. Buryan, Desulfurization of boiler flue gas by means of activated calcium oxide, *Fuel Process. Technol.*, **2013**, 111, 62–67.

[71] M. C. Stewart, V. Manovic, E. J. Anthony, and A. Macchi, Enhancement of indirect sulphation of limestone by steam addition., *Environ. Sci. Technol.*, **2010**, 44, 8781–8786.

[72] G. Q. Liu, Y. Itaya, R. Yamazaki, S. Mori, M. Yamaguchi, and M. Kondoh, Fundamental study of the behavior of chlorine during the combustion of single RDF, *Waste Manag.*, **2001**, 21, 427–33.

[73] C. Zhu, S. Chu, G. A. Tompsett, J. Yang, and P. Mountziaris, T Dauenhauer, ReEngineered Feedstocks for Pulverized Coal Combustion Emissions Control, *Ind. Eng. Chem. Res.*, **2014**, 53, 17919-17928.

[74] D. Bai, Systems and Methods for Processing a Heterogeneous Waste Stream, U.S. Patent 20120305686, December 6, 2012.

[75] D. Bai, Systems and Methods for Producing Engineered Fuel Feedstocks with Reduced Chlorine Content, U.S. Patent 20130298455, November 14, 2013.

[76] Galbraith Laboratories Inc., http://www.galbraith.com.

[77] B. M. Jenkins, L. L. Baxter, T. R. Miles Jr., and T. R. Miles, Combustion properties of biomass, *Fuel Process. Technol.*, **1998**, 54, 17–46.

[78] H. J. Ollila, A. Moilanen, M. S. Tiainen, and R. S. Laitinen, SEM–EDS characterization of inorganic material in refuse-derived fuels, *Fuel*, **2006**, 85, 2586–2592.

[79] The Engineering ToolBox, Heating Values of Standard Grade Coal. http://www.engineeringtoolbox.com/coal-heating-values-d_1675.html.

[80] R. H. Borgwardt, Calcination kinetics and surface area of dispersed limestone particles, *AIChE J.*, **1985**, 31, 103–111.

[81] C. Hsia, G. Pierre, and L. Fan, Isotope study on diffusion in $CaSO_4$ formed during sorbent-flue-gas reaction, *AIChE J.*, **1995**, 41, 2337–2340.

[82] C. Hsia, G. R. St. Pierre, K. Raghunathan, and L.-S. Fan, Diffusion through CaSO4 formed during the reaction of CaO with SO_2 and O_2, *AIChE J.*, **1993**, 39, 698–700.

[83] Worldwatch Institute, Biofuels Regain Momentum, 2011, http://vitalsigns.worldwatch.org/vs-trend/biofuels-regain-momentum.

[84] U.S. International Energy Agency, Technology Roadmap - Biofuels for Transport, 2011, 1–56.

[85] A. V. Bridgwater, Principles and practice of biomass fast pyrolysis processes for liquids, *J. Anal. Appl. Pyrolysis*, **1999**, 51, 3–22.

[86] D. Liu, Y. Yu, J. Hayashi, B. Moghtaderi, and H. Wu, Contribution of dehydration and depolymerization reactions during the fast pyrolysis of various salt-loaded celluloses at low temperatures, *FUEL*, **2014**, 136, 62-68.

[87] P. J. Dauenhauer, J. L. Colby, C. M. Balonek, W. J. Suszynski, and L. D. Schmidt, Reactive boiling of cellulose for integrated catalysis through an intermediate liquid, *Green Chem.*, **2009**, 11, 1555-1561.

[88] A. D. Paulsen, M. S. Mettler, and P. J. Dauenhauer, The role of sample dimension and temperature in cellulose pyrolysis, *Energy and Fuels*, **2013**, 27, 2126–2134.

[89] M. S. Mettler, D. G. Vlachos, and P. J. Dauenhauer, Top ten fundamental challenges of biomass pyrolysis for biofuels, *Energy Environ. Sci.*, **2012**, 5, 7797-7809.

[90] M. S. Mettler, A. D. Paulsen, D. G. Vlachos, and P. J. Dauenhauer, Tuning cellulose pyrolysis chemistry: selective decarbonylation via catalyst-impregnated pyrolysis, *Catal. Sci. Technol.*, **2014**, 4, 3822-3825.

[91] Y. Sekiguchi and F. Shafizadeh, Effect of Inorganic Additives on the Formation, Composition, and Combustion of Cellulosic Char., *J. Appl. Polym. Sci.*, **1984**, 29, 1267–1286.

[92] K. Raveendran, A. Ganesh, and K. C. Khilar, Influence of mineral matter on biomass pyrolysis characteristics, *Fuel*, **1995**, 74, 1812–1822.

[93] P. R. Patwardhan, J. A. Satrio, R. C. Brown, and B. H. Shanks, Influence of inorganic salts on the primary pyrolysis products of cellulose, *Bioresour. Technol.*, **2010**, 101, 4646–4655.

[94] I. Y. Eom, J. Y. Kim, T. S. Kim, S. M. Lee, D. Choi, I. G. Choi, and J. W. Choi, Effect of essential inorganic metals on primary thermal degradation of lignocellulosic biomass, *Bioresour. Technol.*, **2012**, 104, 687–694.

[95] D. L. Wilkinson, S.R., Welch, Ross M., Mayland, H.F., Grunes, Magnesium in Plants: Uptake, Distribution, Function, and Utilization by Man and Animals, *Met. Ions Biol. Syst.*, **1990**, 26, 33 – 56.

[96] R. Fahmi, A. V. Bridgwater, L. I. Darvell, J. M. Jones, N. Yates, S. Thain, and I. S. Donnison, The effect of alkali metals on combustion and pyrolysis of Lolium and Festuca grasses, switchgrass and willow, *Fuel*, **2007**, 86, 1560–1569.

[97] P. Jensen, F. Frandsen, K. Dam-Johansen, and B. Sander, Experimental investigation of the transformation and release to gas phase of potassium and chlorine during straw pyrolysis, *Energy & Fuels*, **2000**, 14, 1280–1285.

[98] M. Müller-Hagedorn, H. Bockhorn, L. Krebs, and U. Müller, A comparative kinetic study on the pyrolysis of three different wood species, *J. Anal. Appl. Pyrolysis*, **2003**, 68–69, 231–249.

[99] Q. Liu, S. Wang, Z. Luo, and K. Cen, Catalysis Mechanism Study of Potassium Salts on Cellulose Pyrolysis by Using TGA-FTIR Analysis, *J. Chem. Eng. Japan*, **2008**, 41, 1133–1142.

[100] H. Kawamoto, D. Yamamoto, and S. Saka, Influence of neutral inorganic chlorides on primary and secondary char formation from cellulose, *J. Wood Sci.*, **2008**, 54, 242–246.

[101] A. Khelfa, G. Finqueneisel, M. Auber, and J. V. Weber, Influence of some minerals on the cellulose thermal degradation mechanisms: Thermogravimetic and pyrolysis-mass spectrometry studies, *J. Therm. Anal. Calorim.*, **2008**, 92, 795–799.

[102] Z. A. Mayer, A. Apfelbacher, and A. Hornung, Effect of sample preparation on the thermal degradation of metal-added biomass, *J. Anal. Appl. Pyrolysis*, **2012**, 94, 170–176.

[103] I. Y. Eom, K. H. Kim, J. Y. Kim, S. M. Lee, H. M. Yeo, I. G. Choi, and J. W. Choi, Characterization of primary thermal degradation features of lignocellulosic biomass after removal of inorganic metals by diverse solvents, *Bioresour. Technol.*, 2011,

102, 3437–3444.

[104] N. Shimada, H. Kawamoto, and S. Saka, Different action of alkali/alkaline earth metal chlorides on cellulose pyrolysis, *J. Anal. Appl. Pyrolysis*, **2008**, 81, 80–87.

[105] A. Saddawi, J. M. Jones, and a. Williams, Influence of alkali metals on the kinetics of the thermal decomposition of biomass, *Fuel Process. Technol.*, **2012**, 104, 189–197.

[106] G. Bellesia and S. Gnanakaran, Sodium chloride interaction with solvated and crystalline cellulose: Sodium ion affects the cellotetraose molecule and the cellulose fibril in aqueous solution, *Cellulose*, **2013**, 20, 2695–2702.

[107] G. Varhegyi, E. Jakab, and M. J. Antal, Is the Broido-Shafizadeh model for cellulose pyrolysis true?, *Fuel Energy Abstr.*, **1994**, 8, 1345-1352.

[108] Y. C. Lin, J. Cho, G. A. Tompsett, P. R. Westmoreland, and G. W. Huber, Kinetics and mechanism of cellulose pyrolysis, *J. Phys. Chem. C*, **2009**, 113, 20097–20107.

[109] C. Di Blasi, Kinetic and Heat Transfer Control in the Slow and Flash Pyrolysis of Solids, *Ind. Eng. Chem. Res.*, **1996**, 35, 37–46.

[110] P. J. Dauenhauer, J. L. Colby, C. M. Balonek, W. J. Suszynski, and L. D. Schmidt, Reactive boiling of cellulose for integrated catalysis through an intermediate liquid, *Green Chem.*, **2009**, 11, 1555-1561.

[111] K. Papadikis, S. Gu, and A. V. Bridgwater, Computational modelling of the impact of particle size to the heat transfer coefficient between biomass particles and a fluidised bed, *Fuel Process. Technol.*, **2010**, 91, 68–79.

[112] A. Broido and M. A. Nelson, Char yield on pyrolysis of cellulose, *Combust. Flame*, **1975**, 24, 263–268.

[113] A.G. Bradbury, Y. Sakai, and F. Shafizadeh, A Kinetic Model for Pyrolysis of Cellulose, 1979, 23, 3271–3280.

[114] C. R. Wilke and P. Chang, Correlation of diffusion coefficients in dilute solutions, *AIChE J.*, **1955**, 1, 264–270.

[115] M. S. Mettler, S. H. Mushrif, A. D. Paulsen, A. D. Javadekar, D. G. Vlachos, and P. J. Dauenhauer, Revealing pyrolysis chemistry for biofuels production: Conversion of cellulose to furans and small oxygenates, *Energy Environ. Sci.*, **2012**, 5, 5414-5424.

[116] M. S. Mettler, A. D. Paulsen, D. G. Vlachos, and P. J. Dauenhauer, Pyrolytic conversion of cellulose to fuels: levoglucosan deoxygenation via elimination and

cyclization within molten biomass, *Energy Environ. Sci.*, **2012**, 5, 7864-7868.

[117] P. K. Hepler and R. O. Wayne, Calcium and Plant Development, *Annu. Rev. Plant Physiol.*, **1985**, 36, 397–439.

[118] W. Laue, M. Thiemann, E. Scheibler, and K. W. Wiegand, Nitric Acid , Nitrous Acid , and Nitrogen Oxides, *Ullmann's Encycl. Ind. Chem.* **2012**, 24, 177–223.

[119] A. Aho, N. DeMartini, a. Pranovich, J. Krogell, N. Kumar, K. Eränen, B. Holmbom, T. Salmi, M. Hupa, and D. Y. Murzin, Pyrolysis of pine and gasification of pine chars - Influence of organically bound metals, *Bioresour. Technol.*, **2013**, 128, 22–29.

[120] M. Kleen and G. Gellerstedt, Influence of inorganic species on the formation of polysaccharide and lignin degradation products in the analytical pyrolysis of pulps, *J. Anal. Appl. Pyrolysis*, **1995**, 35, 15–41.

[121] ASTM D5198-09, Standard Practice for Nitric Acid Digestion of Solid Waste, ASTM International, West Conshohocken, PA, 2009.

[122] M. S. Mettler, A. D. Paulsen, D. G. Vlachos, and P. J. Dauenhauer, The chain length effect in pyrolysis: bridging the gap between glucose and cellulose, *Green Chem.*, **2012**, 14, 1284-1288.

[123] T. Hosoya and S. Sakaki, Levoglucosan formation from crystalline cellulose: Importance of a hydrogen bonding network in the reaction, *ChemSusChem*, **2013**, 6, 2356–2368.

[124] P. R. Patwardhan, J. A. Satrio, R. C. Brown, and B. H. Shanks, Product distribution from fast pyrolysis of glucose-based carbohydrates, *J. Anal. Appl. Pyrolysis*, **2009**, 86, 323-330.

[125] X. Zhou, M. W. Nolte, H. B. Mayes, B. H. Shanks, and L. J. Broadbelt, Experimental and Mechanistic Modeling of Fast Pyrolysis of Neat Glucose-Based Carbohydrates. 1. Experiments and Development of a Detailed Mechanistic Model, *Ind. Eng. Chem. Res.*, **2014**, 53, 13290-13301.

[126] X. Zhou, M. W. Nolte, H. B. Mayes, B. H. Shanks, and L. J. Broadbelt, Experimental and Mechanistic Modeling of Fast Pyrolysis of Neat Glucose-Based Carbohydrates. 2. Validation and Evaluation of the Mechanistic Model, *Ind. Eng. Chem. Res.*, **2014**, 53, 13290-13301.

[127] J. B. Paine, Y. B. Pithawalla, and J. D. Naworal, Carbohydrate pyrolysis mechanisms from isotopic labeling: Part 4. The pyrolysis of d-glucose: The formation of furans, *J. Anal. Appl. Pyrolysis*, **2008**, 83, 37–63.

[128] H. H. Carstensen and A. M. Dean, Development of detailed kinetic models for the

thermal conversion of biomass via first principle methods and rate estimation rules, *ACS Symp. Ser.*, **2010**, 1052, 201–243.

[129] C. E. Brewer, K. Schmidt-Rohr, J. A. Satrio, and R. C. Brown, Characterization of biochar from fast pyrolysis and gasification systems, *Environ. Prog. Sustain. Energy*, **2009**, 28, 386-396.

[130] T. Shoji, H. Kawamoto, and S. Saka, Boiling point of levoglucosan and devolatilization temperatures in cellulose pyrolysis measured at different heating area temperatures, *J. Anal. Appl. Pyrolysis*, **2014**, 109, 185–195.

[131] C. Di Blasi, Modeling chemical and physical processes of wood and biomass pyrolysis, *Prog. Energy Combust. Sci.*, **2008**, 34, 47–90.

[132] S. Kersten and M. Garcia-Perez, Recent developments in fast pyrolysis of ligno-cellulosic materials, *Curr. Opin. Biotechnol.*, **2013**, 24, 414–420.

[133] M. M. Wright, D. E. Daugaard, J. A. Satrio, and R. C. Brown, "Techno-economic analysis of biomass fast pyrolysis to transportation fuels," *Fuel*, **2010**, 89, S2–S10.

[134] T. R. Brown, R. Thilakaratne, R. C. Brown, G. Hu, "Techno-economic analysis of biomass to transportation fuels and electricity via fast pyrolysis and hydroprocessing," *Fuel*, **2013**, 106, 463-469.

[135] V. Agarwal, P. J. Dauenhauer, G. W. Huber, and S. M. Auerbach, Ab initio dynamics of cellulose pyrolysis: Nascent decomposition pathways at 327 °C and 600 °C, *J. Am. Chem. Soc.*, 2012, 134, 14958–14972.

[136] M. Garcia-Perez, A. Chaala, H. Pakdel, D. Kretschmer, and C. Roy, Characterization of bio-oils in chemical families, *Biomass and Bioenergy*, **2007**, 31, 222–242.

[137] M. J. Antal and M. Grønli, The Art, Science, and Technology of Charcoal Production, *Ind. Eng. Chem. Res.*, **2003**, 42, 1619–1640.

[138] J. Lédé, Cellulose pyrolysis kinetics: An historical review on the existence and role of intermediate active cellulose, *J. Anal. Appl. Pyrolysis*, **2012**, 94, 17–32.

[139] A. R. Teixeira, C. Krumm, K. P. Vinter, A. D. Paulsen, C. Zhu, S. Maduskar, K. E. Joseph, K. Greco, M. Stelatto, E. Davis, B. Vincent, R. Hermann, W. Suszynski, L. D. Schmidt, W. Fan, J. P. Rothstein, and P. J. Dauenhauer, Reactive Liftoff of Crystalline Cellulose Particles, *Sci. Rep.*, **2015**, 5, 11238.

[140] C. Krumm, S. Maduskar, A. D. Paulsen, A. D. Anderson, N. L. Barberio, J. N. Damen, C. A. Beach, S. Kumar, and P. J. Dauenhauer, Micro-ratcheted surfaces for a heat engine biomass conveyor, *Energy Environ. Sci.*, **2016**, 9, 1645–1649.

[141] A. K. Burnham, X. Zhou, and L. J. Broadbelt, Critical Review of the Global

Chemical Kinetics of Cellulose Thermal Decomposition, *Energy & Fuels*, **2015**, 29, 2906–2918.

[142] R. Vinu and L. J. Broadbelt, A mechanistic model of fast pyrolysis of glucose-based carbohydrates to predict bio-oil composition, *Energy Environ. Sci.*, **2012**, 5, 9808–9826.

[143] H. B. Mayes, M. W. Nolte, G. T. Beckham, B. H. Shanks, and L. J. Broadbelt, The alpha-bet(a) of glucose pyrolysis: Computational and experimental investigations of 5-hydroxymethylfurfural and levoglucosan formation reveal implications for cellulose pyrolysis, *ACS Sustain. Chem. Eng.*, **2014**, 2, 1461–1473.

[144] H. B. Mayes and L. J. Broadbelt, Unraveling the reactions that unravel cellulose, *J. Phys. Chem. A*, **2012**, 116, 7098–7106.

[145] C. Krumm, J. Pfaendtner, and P. J. Dauenhauer, Millisecond Pulsed Films Unify the Mechanisms of Cellulose Fragmentation, *Chem. Mater.*, **2016**, 28, 3108-3114.

[146] Y. Zhang, C. Liu, and X. Chen, Unveiling the initial pyrolytic mechanisms of cellulose by DFT study, *J. Anal. Appl. Pyrolysis*, **2015**, 113, 621–629.

[147] T. Hosoya and S. Sakaki, Levoglucosan formation from crystalline cellulose: Importance of a hydrogen bonding network in the reaction, *ChemSusChem*, **2013**, 6, 2356–2368.

[148] J. C. Degenstein, P. Murria, M. Easton, H. Sheng, M. Hurt, A. R. Dow, J. Gao, J. J. Nash, R. Agrawal, W. N. Delgass, F. H. Ribeiro, and H. I. Kenttämaa, Fast Pyrolysis of ^{13}C-Labeled Cellobioses: Gaining Insights into the Mechanisms of Fast Pyrolysis of Carbohydrates, *J. Org. Chem.*, **2015**, 80, 1909–1914.

[149] X. Zhang, J. Li, W. Yang, and W. Blasiak, Formation mechanism of levoglucosan and formaldehyde during cellulose pyrolysis, *Energy and Fuels*, **2011**, 25, 3739–3746.

[150] R. S. Assary and L. A. Curtiss, Thermochemistry and Reaction Barriers for the Formation of Levoglucosenone from Cellobiose, *ChemCatChem*, **2012**, 4, 200–205.

[151] T. Hosoya, Y. Nakao, H. Sato, H. Kawamoto, and S. Sakaki, Thermal degradation of methyl β-D-glucoside. A theoretical study of plausible reaction mechanisms, *J. Org. Chem.*, **2009**, 74, 6891–6894.

[152] S. Kozuch and S. Shaik, How to conceptualize catalytic cycles? the energetic Span model, *Acc. Chem. Res.*, **2011**, 44, 101–110.

[153] K. L. Fleming and J. Pfaendtner, Characterizing the catalyzed hydrolysis of β-1,4 glycosidic bonds using density functional theory, *J. Phys. Chem. A*, **2013**, 117, 14200–14208.

[154] C. Loerbroks, A. Heimermann, and W. Thiel, Solvents effects on the mechanism of cellulose hydrolysis: A QM/MM study, *J. Comput. Chem.*, **2015**, 36, 1114–1123.

[155] C. L. Beyler and M. M. Hirschler, Thermal Decomposition of Polymers, *SPE Handb. Fire Prot. Eng.*, **2001**, 2, 110–131.

[156] J. L. Banyasz, S. Li, J. L. Lyons-Hart, and K. H. Shafer, Cellulose pyrolysis: The kinetics of hydroxyacetaldehyde evolution, *J. Anal. Appl. Pyrolysis*, **2001**, 57, 223–248, 2001.